

Erling Vatn Tranulis

# Modeling MMC Energy Dynamics in Offshore HVDC Systems Using OpenModelica

Master's thesis in Energy and environment

Supervisor: Elisabetta Tedeschi

June 2019



Erling Vatn Tranulis

# Modeling MMC Energy Dynamics in Offshore HVDC Systems Using OpenModelica

Master's thesis in Energy and environment  
Supervisor: Elisabetta Tedeschi  
June 2019

Norwegian University of Science and Technology  
Faculty of Information Technology and Electrical Engineering  
Department of Electric Power Engineering



---

# Summary

Our need for clean, renewable energy causes offshore wind to constitute an increasing fraction of our energy mix. Due to considerations of maritime spatial planning and higher wind speeds, the distance to shore increases. This makes modular multilevel converter (MMC) based HVDC systems the superior transmission choice. Because these transmission systems are often large and complex, analyses of the dynamics characterizing them are necessary. Such analyses must be conducted by the use of specialized software that can reproduce the system behavior with sufficient precision.

This thesis uses the open source OpenModelica tool to investigate the power dynamics related to the MMC in offshore HVDC systems. The thesis also demonstrates the suitability of the software for such purposes in two regards. Firstly, it is shown that the software can accurately model systems that are characterized by relatively high-frequency dynamics. This is done by modeling a 10kHz two-level voltage source converter (2L-VSC) in OpenModelica and a benchmark software, MATLAB Simulink. The comparison showed that OpenModelica accurately captured all dynamics of interest as well as provide insight into its trustworthiness and computational resilience. Secondly, it is demonstrated that models developed in OpenModelica can be integrated into systems which are modeled using real-time simulation software (ePHASORSim) and real-time simulation hardware (OP5700). How this integration must be executed is described in this thesis.

Using OpenModelica, the thesis aims to investigate how the energy storage capability of the MMC can improve the power dynamics of an HVDC system. This is investigated in two scenarios that differ in duration and energy requirement. In doing so, it is attempted to demonstrate the characteristics of the MMC's storage capability, which might provide guidelines for determining how this energy should be appropriately used. The first scenario studies the MMC's impact on turbine dynamics caused by wind speed fluctuations around the turbines rated wind speed.

---

It is attempted to smoothen out power fluctuations that arise from the acceleration and deceleration of the turbine rotor upon crossing the rated wind speed. It is demonstrated that the improving impact of the MMC in this regard is almost always negligible, but that the relative impact improves with fluctuation brevity, ideally lasting no longer than two seconds. In the second scenario, it is attempted to reduce the response time of the HVDC system to a step in power reference by utilizing the stored MMC energy. Here, it is shown that the response time is reduced (by a factor of 32) down to a couple of milliseconds. These characteristics demonstrate that the MMC's energy storage capability is best used to counteract power fluctuations in the range of milliseconds to two seconds when the magnitude of the variations are in percent of the rated MMC power. Moreover, because of the coupling between the stored energy in the converter and the DC voltage, a controller is developed to reduce this coupling by using a feed-forward term in the voltage controller. It is showed that when this control is implemented, the step response time of both the DC voltage and the zero-sequence energy sum is reduced by a factor 3 and that oscillations are almost perfectly removed.

In the spirit of joint academic and industrial progress without socioeconomic borders, all models developed in this thesis have been made publicly available [1].

---

# Sammendrag

Mengden installert havvind har steget kraftig de siste 10 årene. Med fortsatt vekst vil havvind gi betydelig bidrag til at vi kan nå internasjonale klimamål om ren, fornybar energi. Som følge av maritim plassplanlegging og høyere vindhastigheter bygges havvind lengre og lengre fra kysten. Store avstander stiller krav til systemene for krafttransport til land. For å oppnå effektiv krafttransport benyttes derfor høyspent likestrøm (HVDC) systemer i kombinasjon med modulære flernivå omformere, såkalte MMC-topologier. For å forstå hvordan disse komplekse systemene påvirkes av ulike variabler, er nøyaktige simuleringer uhyre viktig. Slike analyser krever bruk av spesialiserte dataprogrammer, som gir mulighet for detaljert modellering av systemets dynamiske egenskaper.

I denne avhandlingen er OpenModelica, som er en åpen-kildekode programvare blitt benyttet for å simulere effektdynamikk knyttet til MMC'ene i et HVDC system. Det blir demonstrert at OpenModelica er et velgenet verktøy for slike studier, gjennom tester av to avgjørende egenskaper ved programvaren. Det første omhandler programvarens evne til å presist simulere system preget av relativt høyfrekvent dynamikk. For å oppnå dette ble en to-nivå omformer med en bryterfrekvens på 10 kHz simulert i OpenModelica. Den produserte dynamikken ble sammenlignet med data fra tilsvarende analyser med den veletablerte programvaren MATLAB Simulink. Det viste seg at dynamikken produsert i OpenModelica var meget lik den observert i MATLAB Simulink. OpenModelicas pålitelighet og robusthet i slike analyser ble også undersøkt. Den andre vesentlige egenskapen ved OpenModelica som ble undersøkt, var i hvilken grad modeller utviklet i programvaren lot seg integrere i systemer simulert av sanntidsstimulatorer. For å demonstrere dette ble to modeller utviklet i OpenModelica integrert i system simulert ved simuleringsystemet OP5700 ved bruk av sanntidssimulatoren ePHASORsim. I avhandlingen gis en nøyaktig beskrivelse av hvordan slik integrering kan oppnås.

Ved å bruke OpenModelica er der undersøkt hvordan MMCens energilagringsevne

---

kan forbedre effektdynamikken i et HVDC system. Denne undersøkelsen ble gjort ved å studere to scenario som var særlig forskjellig i varighet og energikrav. Ved å velge scenario på en slik måte ble det forsøk å demonstrere hvilke egenskaper som preger MMCen for å legge et beslutningsgrunnlag for hva denne energien bør brukes til. Det første scenariet undersøker MMCens evne til å utjevne effektvariasjoner som følge av turbinakselerasjon når vindhastigheten overstiger nominell verdi. Her vises det at påvirkningen av MMCen kan ignoreres for de fleste dynamikker, men at den relative påvirkningen øker jo kortere effektutslagene er, og at varigheten helst begrenses til to sekunder. I det andre scenariet ble det forsøkt å redusere responstiden til et HVDC system ved et steg i effektreferansen ved bruk av energien lagret i en MMC. Det ble vist at responstiden kunne reduseres med en faktor 32 ned til et par millisekund. Disse karakteristikene demonstrerer at MMCens energilagringsskapasitet best benyttes til å jevne ut effektvariasjoner hvis varighet spenner fra millisekund til 2 sekund. Videre ble det undersøkt om koblingen mellom DC-spenningen og energien lagret i omformerer kan reduseres ved bruk av et feed-forward signal. Det ble vist at utvidelsen av regulatoren til å inkludere et slikt signal reduserte stegresponstiden med en faktor 3 og at oscillasjoner nærmest forsvant helt for både DC-spenningen og MMC-energien.

Med håp om felles akademisk fremgang uten sosioøkonomiske grenser har alle modeller utviklet i denne avhandlingen blitt gjort tilgjengelig for alle [1].

---

# Preface

When I began my studies, I was, similar to many of my fellow students, hoping that somehow I would be able to contribute to combat a defining challenge of the 21st century - namely climate change. Even the tiniest contribution would be a good thing I reckoned! Now, when looking back at the work summarized in this thesis, I hope that my studies of MMCs in HVDC transmission systems for offshore wind might be exactly such a tiny step forward, although, for me, it has been a giant leap.

The assignment was initially given to two students, Joachim Espvik and me. This has facilitated fruitful collaboration, which proved especially useful for the development of the real-time simulation model. However, it was our task to diverge in terms of scope, and we did this by concentrating on different aspects of energy dynamics in offshore HVDC grids. Whereas I have analyzed MMC related energy dynamics, Joachim has investigated energy dynamics of an external energy storage device. Moreover, due to the similar and complementary nature of our work, our joint efforts have been amalgamated into a single academic paper which is appended to this thesis [2]. These findings will also be presented at the Offshore Energy and Storage Summit in July of 2019.

The thesis is structured and written so that it can be understood by other students who are in the same position I was in when I began to write it.

I want to express my sincere gratitude towards NTNU for providing me with some of the most inspiring and memorable years of my life.

Trondheim 06.06.2019,

A handwritten signature in black ink, appearing to read 'Erling Vatten', with a stylized flourish at the end.

---

---

## Acknowledgment

I want to express my deepest gratitude towards my supervisor, Elisabetta Tedeschi. Her support and guidance have proved to be of fundamental importance to me. I am also grateful for all the hours she has spent proofreading my work and meeting with me to give me the best chance of success. Her believing in me has allowed this thesis to develop as it has, and I will always be thankful for it.

I would also like to express my gratitude towards my co-supervisor, Santiago Sanchez-Acevedo. His aid in regards to the understanding of how to properly use the real-time simulators as well as how to integrate the models is most appreciated. During the entire development process, his suggestions and counseling have provided me with the necessary guidelines to achieve what I have.

In the early stages of the development of this thesis, Gilbert Bergna-Diaz was extremely helpful and was an excellent source for knowledge regarding the inner workings of the MMC as well as how to appropriately model them. For his flexibility, kindness, and insight, I will always be grateful.

I am also very thankful towards Joachim Espvik. He and I were given the same original problem description and had to diverge with regards to focus. However, the similarities in scope and focus allowed us to work jointly on specific topics, especially relating to the real-time simulations. Moreover, discussing and academically sparring with Joachim has been tremendously helpful in gaining a deeper understanding of close to all technical aspects touched upon in this thesis.

Lastly, I would like to thank my girlfriend, Ingvild. Writing a Master's thesis includes incredible highs and hopeless lows. I am thankful that I got to share the good moments with her and that she made the darkest hours slightly brighter.

---

# Table of Contents

<b>Summary</b>	<b>i</b>
<b>Sammendrag</b>	<b>iii</b>
<b>Preface</b>	<b>v</b>
<b>Table of Contents</b>	<b>xii</b>
<b>List of Tables</b>	<b>xiii</b>
<b>List of Figures</b>	<b>xviii</b>
<b>Nomenclature</b>	<b>xix</b>
<b>1 Introduction</b>	<b>1</b>
1.1 The offshore wind energy system . . . . .	1
1.1.1 Distance to shore . . . . .	2
1.1.2 HVDC in offshore wind . . . . .	5
1.1.3 The use of voltage source converters in offshore HVDC systems . .	6
1.2 The modeling tool OpenModelica . . . . .	12
1.2.1 Equation based . . . . .	12
1.2.2 Open Source . . . . .	13
1.2.3 Different time-steps at different levels of complexity . . . . .	13
1.2.4 Real-time simulation and Hardware-in-the-loop . . . . .	14

---

1.3	Objective . . . . .	14
1.3.1	OpenModelica . . . . .	15
1.3.2	Energy dynamics related to the MMC . . . . .	15
1.4	Method . . . . .	16
1.5	Limitation of scope . . . . .	17
1.6	Structure of the thesis . . . . .	18
<b>2</b>	<b>Modeling of the HVDC system</b>	<b>19</b>
2.1	Modeling of the MMC . . . . .	20
2.1.1	Average modeling of the MMC . . . . .	20
2.1.2	Specific modeling decisions . . . . .	24
2.1.3	The MMC model . . . . .	26
2.2	Control of MMC . . . . .	33
2.2.1	Current controller . . . . .	35
2.2.2	Energy controller . . . . .	37
2.2.3	Voltage controller . . . . .	40
2.3	Cable . . . . .	44
2.3.1	Steady-state conventional cable model . . . . .	44
2.3.2	The cable model . . . . .	45
2.4	Turbine . . . . .	46
2.4.1	Pitch angle control . . . . .	48
2.4.2	Torque controller . . . . .	49
<b>3</b>	<b>OpenModelica: verification and integration with Opal RT</b>	<b>51</b>
3.1	Modeling high-frequency dynamics: a Two-level VSC switching model . . . . .	52
3.1.1	Modeling of the switches . . . . .	53
3.1.2	PWM . . . . .	54
3.1.3	The memory block . . . . .	54
3.2	Integration of OpenModelica models with real-time simulation tools . . . . .	55
3.2.1	The creation/adaptation of the OpenModelica model . . . . .	57
3.2.2	The ancillary files . . . . .	61
3.2.3	The integration process . . . . .	64
3.2.4	The model construction in the Simulink environment . . . . .	66

---

---

<b>4</b>	<b>Simulation and results</b>	<b>67</b>
4.1	Simulation of switching model of two-level VSC . . . . .	68
4.1.1	Three Phase current . . . . .	68
4.1.2	DC voltage step response . . . . .	70
4.1.3	Run-times . . . . .	71
4.2	Real-time simulation using Opal-RT . . . . .	73
4.3	Dampening power fluctuations from the wind turbine . . . . .	75
4.4	Using stored energy to improve the step response of the power output . .	79
4.4.1	Base case . . . . .	79
4.4.2	PI controller . . . . .	81
4.4.3	Behavior-based control . . . . .	82
4.5	Impact of feed-forward in DC voltage control . . . . .	85
<b>5</b>	<b>Discussion</b>	<b>89</b>
5.1	OpenModelica's suitability to model HVDC systems . . . . .	90
5.1.1	Modeling of high frequency dynamics . . . . .	90
5.1.2	Integration of OpenModelica models with real-time simulation tools	94
5.2	Controlling the MMC to improve HVDC energy dynamics . . . . .	96
5.2.1	Dampening power fluctuations from the wind turbine . . . . .	96
5.2.2	Using stored energy to improve the step response of the power output	99
5.2.3	Impact of a feed-forward term in voltage controller . . . . .	101
<b>6</b>	<b>Conclusion and future work</b>	<b>103</b>
6.1	Conclusion . . . . .	103
6.2	Future work . . . . .	105
6.2.1	Modeling of switches . . . . .	105
6.2.2	HIL-testing . . . . .	105
6.2.3	Further development of the model . . . . .	106
	<b>Bibliography</b>	<b>107</b>
	<b>Appendices</b>	<b>125</b>
<b>A</b>	<b>Paper for OSES2019 conference</b>	<b>127</b>

---

---

<b>B Model Parameters and definitions</b>	<b>139</b>
B.1 Per unit definitions . . . . .	139
B.2 MMC parameters . . . . .	140
B.3 2L-VSC parameters . . . . .	140
B.4 ePHASORSim test parameters: MMC_base . . . . .	141
B.5 ePHASORSim test parameters: HVDC_BASE . . . . .	141
B.6 Cable . . . . .	142
B.7 Turbine Parameters . . . . .	142
B.8 Behavior-based Energy reference controller parameters . . . . .	143
B.9 Transformation Matrix . . . . .	143
<b>C Proofs</b>	<b>145</b>
C.1 Energy sum derivation . . . . .	145
C.2 Coupling matrix . . . . .	149

# List of Tables

4.1	Table listing run-times [s] of 2L-VSC switching models when modeling 0.5s. Simulations labeled x means the dynamics produced are wrong. na. means not available. WMB means with memory block, WCD means with continuous delay . . . . .	72
B.1	Per unit definitions . . . . .	139
B.2	MMC parameters . . . . .	140
B.3	2L-VSC parameters . . . . .	140
B.4	MMC_BASE parameters . . . . .	141
B.5	HVDC_BASE parameters . . . . .	141
B.6	Cable parameters [51] . . . . .	142
B.7	Turbine parameters [101] . . . . .	142
B.8	Parameters defining zero-sequence energy sum during power step . . . . .	143

---

# List of Figures

1.1	Average wind speeds in Europe [15] . . . . .	3
1.2	Distance to shore and water depth organized by development status [19]. The bubble size indicates the capacity of the site . . . . .	4
1.3	Overview of offshore wind energy system [28] . . . . .	6
1.4	Overview of offshore energy transmission technology . . . . .	8
1.5	a-phase of 2L-VSC and MMC. Note that the DC-capacitor of the MMC is primarily distributed among the submodules . . . . .	8
2.1	Overview of the HVDC system of investigation . . . . .	19
2.2	Topology of three-phase MMC [43]. . . . .	20
2.3	The two submodule states during normal operation . . . . .	21
2.4	Model of a MMC . . . . .	23
2.5	Different MMC modeling strategies used in the literature . . . . .	25
2.6	Overview of the MMC model . . . . .	32
2.7	Different MMC control strategies used in the literature . . . . .	34
2.8	Current controller . . . . .	35
2.9	Current control loop . . . . .	36
2.10	Energy controller . . . . .	37
2.11	Controller used to determine the energy reference . . . . .	39
2.12	Voltage controller . . . . .	41
2.13	Voltage control loop . . . . .	41

---

2.14	Gain, $ G_{vc,ol}(\omega) $ , and phase $\angle G_{vc,ol}(\omega)$ of the open loop transfer function of the voltage controller. The gain is illustrated using asymptotes. The asymptotes of the phase is drawn in dotted red. . . . .	42
2.15	Steady-state pi-model of a cable [96] . . . . .	44
2.16	Pi-section used in the cable model . . . . .	45
2.17	Overview of turbine model . . . . .	47
2.18	Overview of the pitch angle controller used in the wind turbine model . .	48
2.19	Torque controller . . . . .	49
3.1	System modeled in OpenModelica and Matlab to validate OpenModelicas ability to model systems characterized by relatively high frequency dynamics	52
3.2	The models for the IGBT-diode pair . . . . .	53
3.3	PWM used to produce switching states . . . . .	54
3.4	Overview of real-time simulation structure. Unidirectional arrows mean that one element of the structure is "contained" in another, while bidirectional arrows indicate that data are exchanged between two elements . . .	56
3.5	Illustration of a system simulated with ePHASORSim, containing an MMC model developed in OpenModelica. . . . .	57
3.6	Illustration of a system simulated with ePHASORSim, containing a HVDC-link developed in OpenModelica. . . . .	57
3.7	Illustration of reference frame-transformation . . . . .	58
3.8	MMC_base: the OpenModelica model interfaced with the system from fig. 3.5. The controllers and system equations are described in sections 2.1 and 2.2 and it is integrated with the rest of the system using a local to global transformation using eqs. (3.1) to (3.2) and a Power Pin. . . . .	60
3.9	HVDC_Base: The three phase OpenModelica model of an HVDC-link designed to be used with ePHASORSim in fig. 3.6. The MMC models are depicted in fig. 2.6 and the cable is described in section 2.3 . . . . .	60
3.10	FMUGlossary file. Lines 10 - 75 are hidden since they only shown the example components. The remaining 8 parameters are described in columns H-O . . . . .	62
3.11	The Pins section of the necessary Excel file. . . . .	63
3.12	How RT-lab assigns tasks based on subsystem division [115] . . . . .	65

---

---

3.13	Overview of OpComm blocks in various subsystems [115] . . . . .	65
3.14	Simulink environment used in the simulation of the system from fig. 3.5 with the integrated MMC FMU model from fig. 3.8 . . . . .	66
4.1	Three-phase grid currents produced by MATLAB Simulink and OpenMod- elica . . . . .	69
4.2	DC voltage produced by MATLAB simulink and OpenMModelica . . . . .	70
4.3	Real-time simulation system/Real-time target used for the simulations . .	73
4.4	Response of the 6 output variables of the system modeled containing the 4 MMC variables . . . . .	74
4.5	Model used when testing if the MMC can improve the power response of an energy system during wind fluctuations . . . . .	75
4.6	Power profiles during fluctuation in wind speed and rotational speed of generator. The blue power profile represents the case with $\Delta w_{\Sigma,z,ref} = 0$ and the green profile represents the case using the controller from fig. 2.11. The black line is $w_{gen,pu}$ and the red line is $v_{wind,pu}$ . . . . .	76
4.7	Zero-sequence energy sum of the MMC during the simulation in p.u. . . .	76
4.8	Blade pitch angle in green and blade pitch angel reference in blue . . . .	77
4.9	Zoomed image from fig. 4.6. In the green power response $w_{\Sigma,z,ref}$ is con- trolled, while in the blue response it is set to be 1 . . . . .	78
4.10	Multiterminal HVDC system used to investigate if the energy storage ca- pabilities of the MMC can improve the power flow to Grid 3 . . . . .	79
4.11	Power profile during unaided reference step at $t = 1.0$ . The green profile is the power delivered to the converter from the HVDC-cable, the red profile is the power delivered to the grid, the blue profile is $w_{\Sigma,z,pu}$ of the power controlling converter, and the black dotted line is the steady-state power to grid . . . . .	80
4.12	Power profile during reference step at 1.0 using PI controller to control $w_{\Sigma,z,ref}$ . The green profile is the power delivered to the converter from the HVDC-cable, the red profile is the power delivered to the grid, the blue profile is $w_{\Sigma,z,pu}$ of the converter, and the black dotted line is the steady-state power to grid. . . . .	81
4.13	Illustration of the needed energy to be released by the converter . . . . .	83

---

---

4.14	Power profile during reference step at 1.1 using behavior-based control. The green curve is the power delivered to the converter from the HVDC-cable, the red is the power delivered to the grid, the blue is $w_{\Sigma,z,pu}$ of the converter, and the black line is the steady-state power to the grid. . . . .	84
4.15	Model used to investigate the impact of the feed-forward term described by eq. (4.5) . . . . .	86
4.16	$v_{DC}$ (red) and $w_{\Sigma,z,pu}$ (blue) during a step in $w_{\Sigma,z,ref}$ of 0.1 p.u. at $t = 3s$ . The dotted lines are without the new feed-forward and the dotted are with the new feed-forward . . . . .	86
4.17	$v_{DC}$ (red) and $w_{Sigma,z,pu}$ (blue) during a step in $v_{DC,ref}$ of 0.1 p.u. at $t = 4s$ . The dotted lines are without the new feed forward and the dotted are with the new feed forward . . . . .	87
5.1	Tearing of algebraic Loop[122] . . . . .	92

---

# Nomenclature

## Subscripts

$[u, l]$  = upper and lower arm respectively

a = arm

$\circ$  = circulating

c = converter (AC-side); exception:  $i_c$  is current into DC-side capacitor

g = grid (AC)

$\Sigma$  = sum of variable in upper and lower arm

tot = total

DC = DC-side of converter on the converter side of the capacitor

eq = equivalent

ref = reference

pu = per unit

k = generic phase  $\in [1, 2, 3]$

j = generic arm  $\in [u, l]$

$[1, 2, 3]$  = phase of three-phase balanced system

$[d, q, z]$  = component Park-transformed variable

ol = open loop

cl = closed loop

cc = current controller

vc = voltage controller

w $\Sigma$  = Energy sum

$\circ cc$  = circulating current controller

v = equivalent AC-side

f = AC-side series impedance

RT = Rise time

RTC = Rise time constant

erc = energy reference creator

$[i, p]$  = integral and proportional gain respectively

SM = submodule

---

## Superscripts

123 = 123-reference frame

$dqz$  = dqz-reference frame

## Variables

$v$  = voltage (wind speed in turbine model)

$i$  = current

$r$  = resistance

$l$  = inductance

$c$  = capacitance

$g$  = conductance

$z$  = impedance

$y$  = admittance

$w$  = energy

$\omega$  = angular frequency

$\phi$  = angular difference

$P$  = power

$Q$  = reactive power

$\delta$  = switch state

$\tau$  = time constant

$T$  = period (Torque in turbine model)

$t$  = time

$\gamma$  = propagation factor

$\lambda$  = Tip-speed ratio

$C_p$  = power coefficient

$\beta$  = pitch angle

$\mathbf{T}$  = Transformation matrix

$\mathbf{J}$  = Coupling matrix

$\delta$  = Switch state of IGBT

$G$  = transfer function

ff = feed-forward

---

## Abbreviations

MMC = Modular Multilevel Converter  
IGBT = Insulated-gate bipolar transistor  
HVDC = High Voltage Direct Current  
VSC = Voltage Source Converter  
2L-VSC = two-level Voltage Source Converter  
RES = Renewable Energy Source  
HVAC = High Voltage Alternating Current  
PWM = Pulse Width Modulation  
HIL = Hardware-in-the-Loop  
SSTI = Steady-state time-invariant  
SSTP = Steady-state time-periodic  
UCM = uncompensated modulation  
CM = Compensated Modulation  
GUI = Graphical user interface  
FMI = Functional Mock-up interface  
FMU = Functional Mock-up unit  
PM = phase margin  
KVL = Kirchhoff's voltage law  
KCL = Kirchhoff's current law

## Parameters

R = resistance  
L = inductance  
C = capacitance  
G = conductance  
B = friction coefficient  
J = moment of inertia  
 $\ell$  = length  
K = Gain of PI controller  
f = frequency = 50 Hz  
N = number of submodules

---

# Introduction

## 1.1 The offshore wind energy system

In keeping with the climate goals of the UN following the Paris climate agreement, renewable energy sources have seen increased implementation in recent years [3]–[5]. In 2018 95% of all new EU power installations were constituted by renewable energy sources and wind accounted for more than 50% of these installations [4]. Furthermore, 2018 was a record year for Final Investment Decision in future capacity, reaching 16.7 GW worth of wind projects [4]. This record is not a simple reflection of increased investment, but rather that the prices are descending. Therefore, investors can buy more for less. Moreover, offshore wind installations accounted for 23% of all wind power installations in 2018, which is the highest fraction in European history [4]. Furthermore, Wind Europe’s central scenario for an outlook towards 2030, predicts installation levels of 323 GW with 70 GW coming from offshore wind, close to 4 times the current capacity [6].

Although onshore wind currently has and is projected to maintain, the majority of the

wind power capacity, the energy system of offshore wind is subject to investigation in this thesis. One reason for this is the *potential* of offshore wind. For instance, the potential for offshore wind in Germany has been estimated to be 54 GW equalling its currently installed onshore capacity [7], [8]. Similarly, the offshore potential in California alone is estimated to be between 58.6 and 75.5 GW, which is more than ten times Californias installed capacity as per 2018 [9], [10]. Moreover, the potential for offshore wind in Japan is 1600 GW, close to six times higher than the onshore wind potential, which is estimated to be 280 GW [11], [12]. Another reason for why offshore wind is the focal point is because it is an extremely fast growing renewable energy source (RES), expected to increase by a factor of four in just twelve years in Europe [6]. Lastly, offshore wind is chosen as the subject of investigation because the distances from the wind parks to shore are increasing [13]. As will be explained in 1.1.2, this forces the industry to use a completely different energy transmission system, High-voltage, direct current (HVDC), than would otherwise be implemented. The energy dynamics of one of the vital component of this energy transmission system, the converter, is one of the main focal points of this thesis.

### 1.1.1 Distance to shore

When considering how far off the coast an offshore wind project should be constructed, several aspects must be carefully considered. For instance, ABB has argued that *economics* related to the higher wind speeds accessible far from the coast could offset the higher initial cost in the long run [13]. Others, like DNV GL has referred to *maritime spatial planning* as the main driver when considering increased distances to shore [14]. It is reasonable to assume that such elements will vary significantly between localities. Therefore, comprehensive analysis, which takes into account local factors, must be performed in the assessment of potential offshore wind farms. However, some trends and studies related to these two aspects will be briefly covered here.

**Economics**

Economics plays an important role when determining the conditions of operation. Of major importance in this regard is the wind conditions of the location. Higher wind speeds further from shore allow for larger wind turbine implementations and thus higher revenue [15], [16], see fig. 1.1.

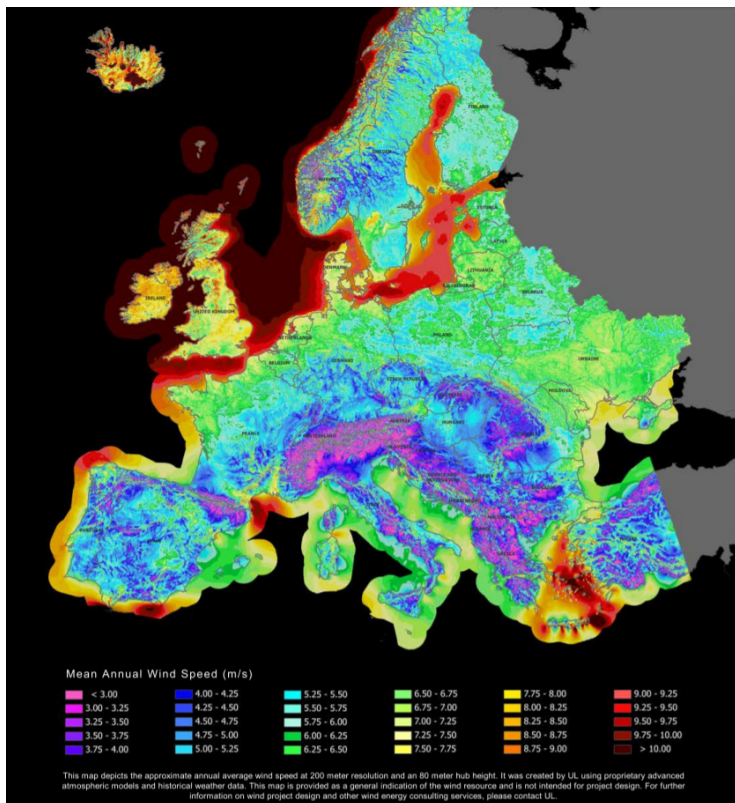


Figure 1.1: Average wind speeds in Europe [15]

This might explain why average distances to shore have been increasing in the past [17]. However, increasing distance to shore has not yet resulted in decreased cost per MWh and is often referred to as one of the main reasons why the offshore industry has *not* seen the same price reduction as the onshore wind industry [18]. More specifically, it has been found that for every 10% increase in distance to shore (or water depth), the

## Chapter 1. Introduction

---

specific investment cost (k€/MW) increases by 1% [18]. This might, in part, explain the decrease in average distance to shore seen from 2017 to 2018 [19].

However, as can be seen in fig. 1.2, it is reasonable to assume that an increasing share of offshore wind sites will be located more than 75 km from shore in the future. This can be seen by considering the percentage of sites located further away than 75 km that are already online (i.e., in operation) compared to the same share of sites that only have a permit. As can be seen, only 5 of about 85 of online and partially online sites are located further away than 75 km. On the other hand, 9 out of the 28 sites that either have a permit or are under construction are located at least that far away. Additionally, three out of seven projects under development in Germany (2018) were located more than 100 km from shore [20]. This might relate to projections of future specific prices, which reach €80/MWh across all distances to shore within 2030 in the central scenario of WindEurope [6].

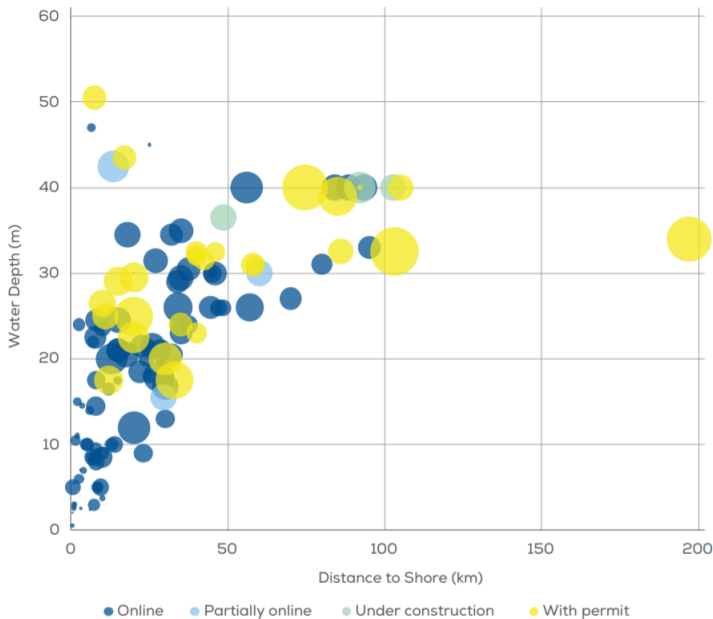


Figure 1.2: Distance to shore and water depth organized by development status [19]. The bubble size indicates the capacity of the site

### Maritime spatial planning

Another important element of "distance to shore" relevance is national maritime spatial planning [21]. This has been of major consideration for China in its offshore expansion. The state-owned power company "Powerchina huadong engineering corporation limited" is now planning to build their first HVDC offshore wind power park [22], [23]. They have contracted DNV GL to, in part, conduct a feasibility study for an offshore HVDC converter station and, as DNV GL pointed out, all offshore sites close to shore have already been exploited [14]. Similar considerations are increasingly relevant in Europe considering its expansive wind industry. The average installation distance in Germany for new installations is 74 km to keep them out of sight of coastal dwellers [7].

### 1.1.2 HVDC in offshore wind

When transferring power across long distances, HVDC is often advantageous compared to high-voltage, alternating current (HVAC). This is because HVDC has certain features which become very attractive when the transmission distance is long. HVDC can be used to connect grids operating at different frequencies and can transfer the same amount of power as HVAC with lower environmental impact because of a simpler line construction and smaller towers. HVDC has higher power transmission per conductor, no skin or proximity effect, and no charging current and therefore no need for reactive compensation. Additionally, HVDC has lower losses given the same power transfer [24]. This means that the marginal cost of increasing transmission distance is lower when the transmission system employs HVDC rather than HVAC.

However, the converter stations are quite expensive. The fixed cost for one offshore HVDC converter station has been estimated to be 25 M£ [25]. Thus, for short distances, the economic advantage per length does not outweigh the cost of the converter station, making HVAC the economically advantageous option.

The distance at which HVDC becomes price-competitive has been thoroughly investi-

gated. It has been shown that VSC-HVDC and HVAC have a break-even point at 87 km when using a low power rating of 0.6 GW [25]. When using a high power rating of 1.4 GW, the break-even point is reduced to 70 km. As a rough rule of thumb, ABB uses 60 km as a critical distance for submarine lines used in HVDC [13], [26]. Earlier work indicated similar findings and found a break-even point of VSC-HVDC and HVAC at 85 km using a power rating of 0.4GW [27].

In summary: our need for clean energy coupled with maritime spatial planning and economics, drive offshore wind energy production further away from shores. This requires the use of HVDC to transport the extracted power in an economically efficient manner to shore.

### 1.1.3 The use of voltage source converters in offshore HVDC systems

One of the core components of an HVDC system is the converter station, responsible for converting the current from AC to DC or vice versa, see fig. 1.3.

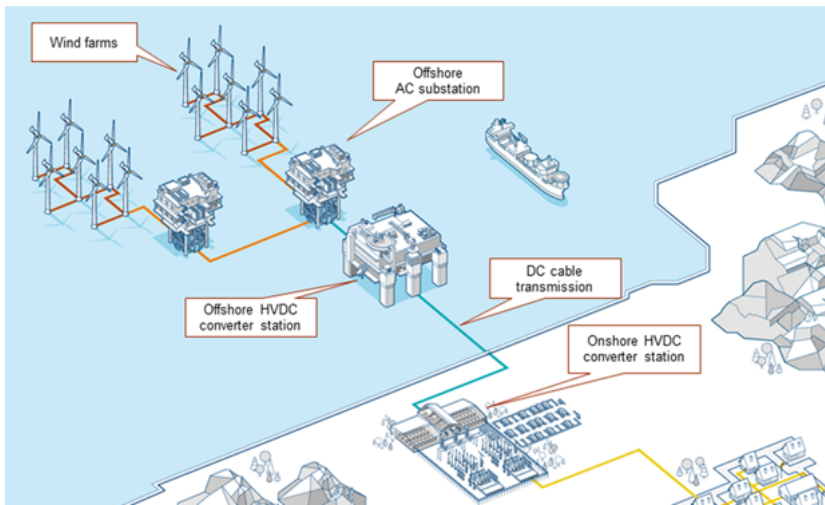


Figure 1.3: Overview of offshore wind energy system [28]

Of the two possible converter types available for HVDC, line commutated converter and voltage source converter (VSC), every offshore HVDC wind project to date has used VSCs [29]. In multi-terminal HVDC grids, they introduce a specific advantage because VSCs can reverse the power flow without reversing the polarity of the DC voltages, but rather reverse the flow of DC current [30]. Further key advantages are listed below [24], [29], [30].

- Independent control of active and reactive power
- Option of zero power operation
- Possibility of connecting to weak AC grids
- Lower harmonic production
- Black start capability
- More compact converter stations

### **Using MMCs as VSC in offshore HVDC systems**

As explained previously in this chapter, there are several available technological solutions for designing offshore wind transmission system, see fig. 1.4. Assuming an offshore wind project is sufficiently far from shore to make VSC-HVDC transmission the economically preferred choice, the remaining important question is which VSC should be used. The converter topology, which has been investigated herein is the Modular Multilevel Converter (MMC). To better understand why this converter is chosen, its operational principle will be compared to a two-level voltage source converter (2L-VSC).

It should be noted that other topologies exist, such as various three-level converters. However, because the purpose of this section is to illustrate the advantages of the MMC, not all converter topologies will be explained here. This is because the advantages of the MMC compared to the 2L-VSC also apply to other topologies. More thorough comparisons between VSC types, their capabilities, and control can be found in [31], [32].

The a-phase of a 2L-VSC and an MMC are depicted in fig. 1.5. The b- and c-phases of

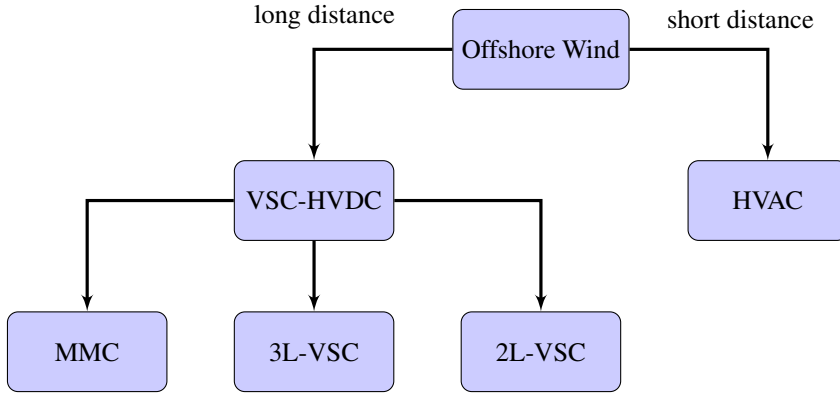
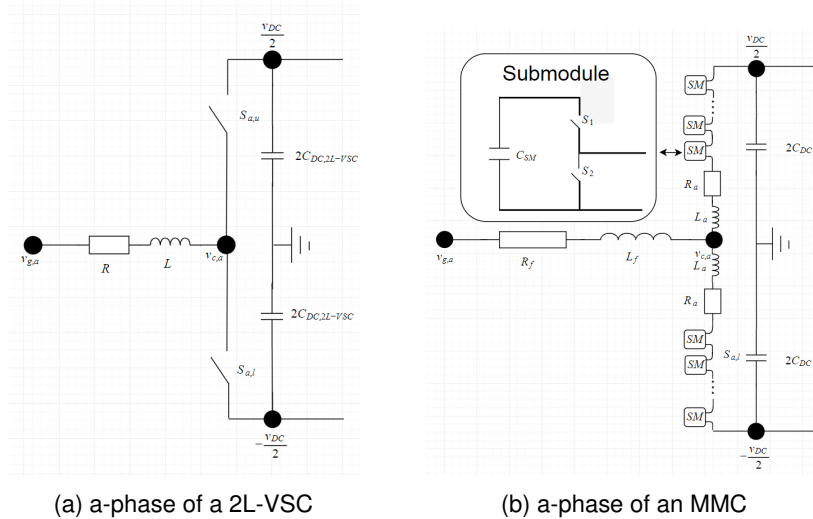


Figure 1.4: Overview of offshore energy transmission technology

the converters are not drawn in this depiction to simplify the overview, given that their operational principle is the exact same as for the a-phase. The left-hand side of each model represents the AC-side, and the right-hand side represents the DC-side.



(a) a-phase of a 2L-VSC

(b) a-phase of an MMC

Figure 1.5: a-phase of 2L-VSC and MMC. Note that the DC-capacitor of the MMC is primarily distributed among the submodules

Both converters are controlled to produce a certain voltage output at the node labeled  $v_{c,a}$  based on the grid voltage  $v_{g,a}$ . Thus, the voltage drop over the AC-side inductor and

---

## 1.1 The offshore wind energy system

---

resistor can be controlled to maintain/reach e.g. a certain active and reactive power flow. By assuming that the resistive drop is quite small, which is reasonable given that a higher resistance gives higher losses, the active and reactive power flow across the inductance,  $L$ , can be described according to eqs. (1.1) and (1.2) where  $f$  is the grid frequency and  $\phi$  is the angular difference between  $v_{g,a}$  and  $v_{c,a}$  [33]. Because  $P$  depends strongly on the angle  $\phi$  and  $Q$  depends strongly on the amplitude  $|v_{c,a}|$ ,  $P$  and  $Q$  can be controlled independently by controlling  $v_{c,a}$  relative to  $v_{g,a}$ .

$$P = |v_{g,a}| |v_{c,a}| \frac{\sin(\phi)}{2\pi f L} \quad (1.1)$$

$$Q = |v_{g,a}| |v_{c,a}| \frac{\cos(\phi) - |v_{g,a}|}{2\pi f L} \quad (1.2)$$

The 2L-VSC produces  $v_{c,a}$  by quickly alternating between applying high and low voltage, e.g.  $v_{DC}/2$  and  $-v_{DC}/2$ . High voltage is applied by closing  $S_{a,u}$ , and opening  $S_{a,l}$ , and low voltage is applied by changing the state of both switches. This is typically done using pulse-width modulation (PWM) with a switching frequency significantly higher than the frequency of the grid [24], [30], [34], [35]. This means that the grid voltage does not change significantly during one switching period. Thus, if the 2L-VSC should make  $|v_{c,a}| = 0.7 \frac{v_{DC}}{2}$  at any one instance based on  $v_{g,a}$  to produce desired  $P$  and  $Q$  flows, then  $v_{DC}/2$  is applied for 85% of the switching period, while  $-v_{DC}/2$  voltage is applied during the remaining 15% of the switching period.  $v_{c,a}$  is thus produced dynamically by the 2L-VSC, by altering the period of high voltage application to low voltage application.

The MMC produces  $v_{c,a}$  in a slightly more sophisticated way. As can be seen in fig. 1.5b, each phase of the MMC contains several cascade connected submodules. Every submodule includes a capacitor with a roughly equal share of the total arm voltage across it. Each of these submodules can be connected in series to the inductance and resistance of each arm,  $R_a$  and  $L_a$ , or the submodules can be bypassed. Thus, if the MMC should make  $|v_{c,a}| = 0.7 \frac{v_{DC}}{2}$  at any one instance, then 85% of the submodules in the lower arm and 15% of the submodules in the upper arm are inserted, while the remaining submodules are bypassed. This is because the total arm voltage equals the DC voltage. Thus,  $v_{c,a}$  is produced dynamically by the MMC, by periodically inserting and bypassing submodules sequentially.

Historically, both VSC topologies have been utilized in HVDC systems. The first was a 2L-VSC developed by ABB used in HVDC Light 1st Gen which was employed in 1997 in a demo project in Gotland [36]. ABB continued their development of HVDC systems by building the first offshore HVDC system. First, the power from shore system that fed Troll 1 and 2 which was finished in 2005 [37], then, the first offshore wind project, the Borwin1, which also used a 2L-VSC finished in 2009 [38]. In 2010, the first use of MMCs was adopted in the Trans Bay cable project. Originally, LCCs were intended for this purpose, but the smaller size of VSCs reduced cost by reducing the required land [39]. The ability to chose the number of inserted submodules in each arm, allows the MMC to produce a very smooth waveform compared to the two- or three-level VSCs [31]. The MMC design was, therefore, chosen because of its smoother waveform, reducing the need for filtering. Furthermore, the operational performance showed reduced system losses. Additional advantages such as scalability, modularity, and flexibility are among the reasons why the MMC is assumed to be the converter of choice in future offshore HVDC systems by several researchers [40]–[51].

Recently, efforts have been made to investigate if the energy storage capabilities of MMC could be used to improve various characteristics of an HVDC system. For instance, it was showed that the energy stored in an MMC could provide power oscillation damping services to enhance grid stability [52]. Related work was done to investigate if this capability could smoothen out active power fluctuations associated with wind gusts and tower shadowing in wind-based HVDC grids [53]. Ref. [54] showed how the same energy storage could be controlled to provide primary frequency regulation and system inertia. Another team of researchers has investigated how this energy could be used to improve the voltage behavior in multi-terminal HVDC grids [55]. Others have focused on how the MMC energy storage could reduce low-frequency arm current ripple and thus improve the lifetime of a battery storage system [56]. Similar results were found in [57], that also showed improved transient voltage performance at the point of common coupling and increase battery life span when battery storage systems are combined with MMC.

The motivations for this field of research can broadly be grouped into two topics. The first relates to prolonging the lifetime of system components. As has been shown, reducing

current ripple can improve the lifetime of batteries, but cables and other accessories have also experienced premature aging as a result of DC voltage deviation [55], [56]. The second point deals with requirements of grid codes regarding installations of wind power [58], [59]. This typically includes but is not limited to, acceptable ranges for frequency, voltage level, reactive power control, and power quality. Power quality can refer to flickering, harmonics, and voltage imbalance in the form of a step change. Hence, the motivation into the capability of MMCs to improve these aspects.

Another topic studied in the literature relates to decoupling of the DC voltage and stored energy of the converter. Typically, the control structure of the converter couples these, because reference changes to the DC-side of the converter are accomplished by changing the converters AC-side voltages. This changes the currents and power flowing into the converter, which inevitably changes the stored energy in the converter. This power flow then, in turn, appears on the DC-side of the converter. Some decoupling attempts have been discussed in the literature, for instance, by restructuring the control hierarchy [46].

In this thesis, two aspects of the energy dynamics of the MMC have been investigated. The first relates to the ability to improve the power dynamics of the HVDC system by controlling the stored energy in the submodules of the converter. To correctly map how its potential is best utilized, two cases that differ in duration and energy requirements are investigated. Firstly, it is attempted to improve relative slow dynamics introduced by fluctuations of the wind speed. Then, relatively fast dynamics relating to step changes in the reference of the delivered power by the HVDC system are improved. The second investigation relates to decoupling of the stored energy and DC voltage of the converter. This is attempted by including a feed-forward term in the voltage controller.

The investigations of improving power dynamics are chosen to retain generality, as they do not investigate specific system aspects which can be improved. Instead, they showcase the characteristics and capability of the MMC as an "energy storage" unit. Comparisons of the best use of this capability are not conducted here. Despite this, the presented work could provide insight into how the usage of the converter should be expanded to utilize this energy storage capability. Moreover, no side-by-side comparisons of various con-

trol structures or specific controllers are investigated with regards to decoupling ability. The only investigation that is done in this thesis in this regard relates to the particular improvements introduced by the feed-forward term in isolation.

To analyze the energy dynamics of the MMC, and the potential impact and improvements it can bring to an offshore HVDC system, such a system must be built and simulated using specialized software that can reproduce the effects of the physical components of the grid. The tool used in this thesis is the OpenModelica environment. This was requested by DNV GL, who recognized the advantages the open-source OpenModelica tool could offer if the software proved suitable. Its suitability entails two specific points investigated in this thesis [60]. The first being its ability to model systems that are characterized by relatively high-frequency dynamics. The second is that it must be possible to simulate OpenModelica based models using real-time simulation tools.

## 1.2 The modeling tool OpenModelica

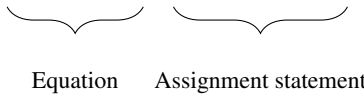
Before an offshore wind power plant and its energy transmission system are implemented, each component of the system must be modeled and tested to verify that everything behaves as expected. The modeling tool used in this thesis is OpenModelica. OpenModelica is an equation based, open-source modeling tool, and this thesis investigates the degree to which OpenModelica is a suitable modeling tool for modeling MMCs and HVDC systems [61].

### 1.2.1 Equation based

Unlike Matlab, OpenModelica is equation based. This means that when describing relationships between variables, these can be expressed as equations. This moves the mathematical labour of transforming an equation into an assignment statement from

the engineer to the software (see eq. (1.3)).

$$a^2 + b^2 = c^2 \Rightarrow a = \pm \sqrt{c^2 - b^2} \quad (1.3)$$



Such transformations can be time-consuming, difficult, tedious, and error-prone, speaking to the advantage of having the software do it.

### 1.2.2 Open Source

OpenModelica is open source, which means that it can be downloaded for free by anyone. This is a huge advantage over Matlab, costing 7.600 NOK annually together with Simulink and Simscape costing 11.400 NOK each, annually, per license for commercial, governmental, or other organizational usages [62], [63]. In addition to reducing costs, this makes product sharing easier and opens doors to collaborations between actors in different economic situations.

### 1.2.3 Different time-steps at different levels of complexity

When simulating a large system, certain states of the system are to a more considerable degree than others characterized by high-frequency dynamics. Thus, they require a smaller time-step to be accurately modeled. If the system contains few variables that change quickly and many variables that change slowly, this constitutes a substantial computational burden if all states must be updated contemporarily. OpenModelica can update different variables using different time-steps [64]–[66]. This allows for accurate modeling without compromising run-times throughout the model.

## 1.2.4 Real-time simulation and Hardware-in-the-loop

The ability to simulate in real-time allows what is called Hardware-in-the-loop (HIL) testing. This technique allows for testing of controllers that control systems, without needing to physically build the system [67]. Instead, the behavior of the system is produced based on simulations of the system. This not only saves time and costs but can allow test engineers to become part of a design process before a test bench is available. Furthermore, this might reduce the risk associated with the control testing of potentially dangerous systems as well as increase repeatability since the system model does not physically deteriorate over time. How OpenModelica models can be exported to run using real-time simulators suitable for HIL-testing is shown in this thesis.

Because of these advantages, another focal point of this thesis is the investigation of OpenModelica's suitability to model HVDC systems in two regards. First, can the software simulate systems characterized by high-frequency dynamics (typical for power electronic systems) and accurately capture those dynamics? Second, how can models developed in OpenModelica be integrated into systems simulated using real-time simulators? The thesis will demonstrate that OpenModelica is capable of capturing relatively high-frequency dynamics accurately by comparing it against a benchmark software: MATLAB Simulink. Furthermore, the thesis contains a detailed guide on how to construct models in OpenModelica that can be integrated into systems simulated by a real-time simulator as well as a description of the integration and modeling process. In doing so, the thesis aims to lay a foundation for modeling and HIL-testing of offshore HVDC systems and components using open source software.

## 1.3 Objective

The objective of this thesis is twofold. It focuses on the energy dynamics relating especially to the MMC in an HVDC system, but also encompasses an investigation into OpenModelica as a tool for modeling such converters and the systems they are used in.

### 1.3.1 OpenModelica

There are three objectives of this thesis that relate to OpenModelica.

1. The thesis will demonstrate OpenModelica's ability to model systems characterized by relatively high-frequency dynamics typical for power electronic systems.
2. The thesis will demonstrate that OpenModelica models can be integrated into larger system models which are run using real-time simulation tools.
3. The thesis will contain a guide describing this integration process. The guide focuses on the development of the OpenModelica model as well as the integration process in the simulation environment.

The first point will be achieved as a proof-of-concept by comparing the dynamic behavior of two 10kHz, 2L-VSC switching models, one developed in MATLAB Simulink and one developed in OpenModelica. The second point will be achieved by simulating systems which contain models developed in OpenModelica by using Opal-RT's ePHASORSim and OP5700. Additionally, the process of how this integration was achieved will be explained as a guide to make it easier for others wishing to do the same.

### 1.3.2 Energy dynamics related to the MMC

The thesis will explore the positive impact an MMC can have on the energy dynamics in an offshore HVDC system. There are three focus points pertaining to this:

1. Improving power dynamics in HVDC system using stored MMC energy.
  - (a) How, and to what degree, can the MMC be utilized to dampen and generally improve power dynamics related to fluctuation in wind speed and the associated turbine dynamics?
  - (b) How, and to what degree, can the MMC be utilized so the HVDC system responds more quickly to step changes in power demand?

2. Can the zero-sequence energy sum and DC voltage of the converter be decoupled by using a feed-forward signal in the voltage controller?

Regarding point 1. the dynamics of particular interest relate to the terminal behavior of the converter and the dynamics that manifest externally and not the internal dynamics of the converter per se. The investigation, therefore, includes two different sub-models of a three-terminal HVDC system that are modeled and investigated separately to isolate the dynamics of interest. The first sub-model seeks to isolate the energy dynamics of the MMC and the wind turbine. The second sub-model aims to isolate the energy dynamics of the HVDC grid constituted by the MMCs, their connecting cables, and stiff grids.

Finally, the second point is investigated by isolating the MMC, assuming stiff boundary conditions with the DC-side as a constant current source.

Moreover, the development of the thesis will result in the production of actual OpenModelica packages for HVDC-cables, converters, and wind turbine models, which will be freely available to the public [1].

## 1.4 Method

The method used in this thesis is made up of four parts. Initially, a literature review is conducted which aims to serve primarily two functions:

- To map the known technical advantage and the need for offshore wind, HVDC systems, MMCs, and OpenModelica
- To ensure that the models used in this thesis are state of the art academically, appropriate for their purpose, and relevant for interested members of the industry.

Subsequently, models are developed and verified using the OpenModelica tool, which also serves two purposes.

- To validate that OpenModelica is a viable modeling tool for such tasks.
- To gain insight into how the energy dynamics of HVDC systems can be improved using the energy storage capabilities of MMCs.

Then, real-time simulations of some of the systems developed in the thesis are conducted at the National Smart Grid laboratory in Trondheim.

Lastly, future work is outlined, with the intent to clarify the path from the end of this thesis to HIL-simulation. Additionally, some other research areas and related modeling tasks that could use this work as a basis are described.

## 1.5 Limitation of scope

The assessment of OpenModelica is limited in mainly two ways. Firstly, OpenModelica's synergy and compatibility with other software is not inspected comprehensively. It is only directly used together with simulators from OPAL-RT for demonstration purposes. However, because of the nature of the tool, the investigation of it will reveal the synergy potential with other tools, although this potential is not investigated explicitly. Secondly, it is only one library of OpenModelica that is used, the electrical library, and not in a comprehensive manner. This does neglect one of the advantages of the software which is its ability to easily build larger models consisting of different sub-models from different domains. Furthermore, no in-depth analysis of the inner workings of the software is conducted.

The scope of investigation of the dynamics relating to the MMCs in HVDC systems is subject to some limitation. The converter is not investigated during fault conditions or similar extreme deviation from the desired conditions nor is the converter investigated in any domain other than in an HVDC system. Second, the modeling precision of MMC is limited. The investigation of the MMC only intends to examine terminal behavior. Thus, converter aspects that only to a limited degree affect this, such as switching events and

the modeling of individual submodules or their components are neglected or simplified. This is because the MMC model is intended to be used to gain insight into dynamics that pertain to an entire HVDC system, and thus, the terminal behavior is of greater interest than the internal dynamics. Dynamics related to and as a result of physical deterioration, thermal effects, saturation, interference, and topological limitations are entirely disregarded. Other interesting energy dynamics of the HVDC system relating to other energy storage devices in the systems are not considered in this thesis. This is because the original project description was given to two students who had to diverge in focus to write independent theses. Energy dynamics relating to dedicated energy storage devices in HVDC systems are explored in [2], [68].

## 1.6 Structure of the thesis

The remaining thesis is structured as follows. Chapter 2 explains modeling of the HVDC system with a focus on the development of the component models and the associated control. Chapter 3 explains how OpenModelica was investigated in regards to its suitability as software to model HVDC systems and its components. Simulations and results are outlined in Chapter 4. Discussions of the results are presented in Chapter 5. Chapter 6 concludes.

# Modeling of the HVDC system

This chapter explains the modeling of the HVDC system used for the simulations in this thesis. This includes the model of the MMC, HVDC-cable, and wind turbines. The overview of the system under investigation is depicted in fig. 2.1.

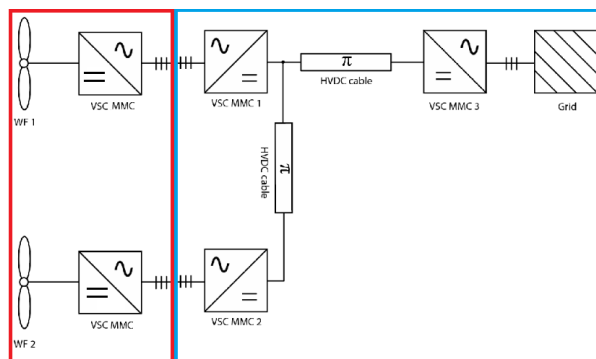


Figure 2.1: Overview of the HVDC system of investigation

The system is modeled as two sub-systems to isolate different energy dynamics. The red sub-system captures dynamics of the turbine caused by wind speed variation, while the blue sub-system captures the energy dynamics arising from power reference steps.

## 2.1 Modeling of the MMC

When modeling MMCs, two decisions must first be made. The first relates to the accuracy with which to model the MMC and which simplifications can be made that still preserve the dynamics of interest. This is done based on the required accuracy concerning what the model should be used for. The second relates more specifically to how the electrical relationships which remain should be expressed and how the MMC is expected to operate. The modeling decisions made in these regards are explained in this section.

### 2.1.1 Average modeling of the MMC

When deciding on the accuracy with which to model the MMC, this effectively means how accurately the arms of the MMC are modeled, see fig. 2.2. A detailed classification for this can be found in [69].

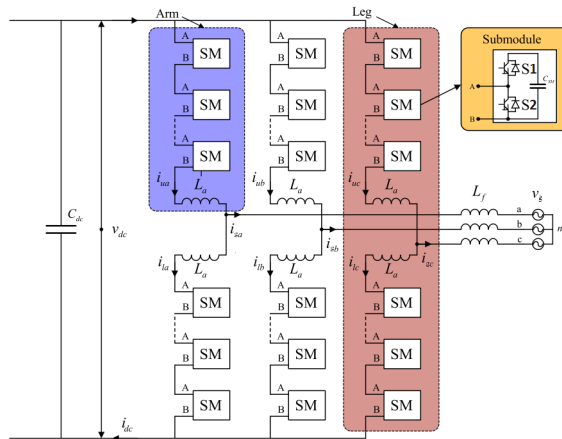


Figure 2.2: Topology of three-phase MMC [43].

Each arm of the MMC contains several submodules comprising switches, modeled as insulated-gate bipolar transistors (IGBTs) and diodes. A very accurate way to model this would be to model each submodule and to model each IGBT and diode using partial differential equations. However, such models are complicated to parameterize and

extremely time-consuming to simulate and are considered not to be suitable for grid studies [69]. Therefore, the modeling of the arms must be simplified. The simplification used here is termed average modeling and is typically 500 times faster than models where each IGBT and diode are modeled explicitly [69]. This means that each arm is just modeled as one controllable voltage source. How this is done and what it means for modeling accuracy is described below.

### Modeling of the arms of the MMC

In reality, each arm consists of  $N$  submodules, see fig. 2.2. There are various submodule topologies available [48], but since the differences between them are outside the scope of this thesis, only their principle is covered here. The submodules comprise a capacitor as well as two switches allowing the submodules to exist in one of two states at any time during regular operation, consider fig. 2.3.

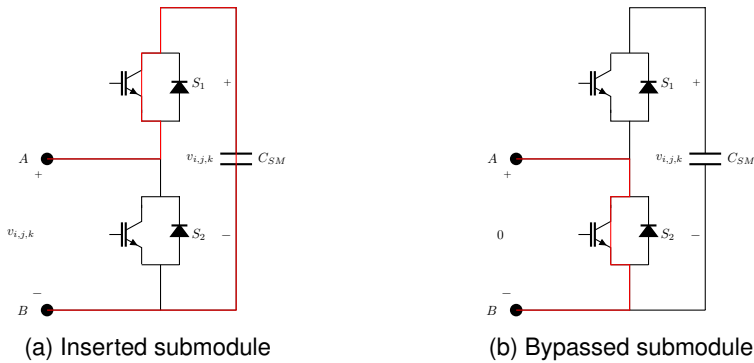


Figure 2.3: The two submodule states during normal operation

Either bypassed, i.e.,  $S_2$  closed and  $S_1$  open (see fig. 2.3b), or inserted, i.e.,  $S_1$  closed and  $S_2$  open (see, fig. 2.3a). Thus, if inserted, the  $i$ -th submodule in phase  $k \in \{1, 2, 3\}$  in arm  $j \in \{u, l\}$  has the same voltage as its capacitor,  $v_{i,j,k}$ . This voltage then contributes to the total arm voltage,  $v_{j,k}$ . If the submodule is bypassed, the voltage across it is zero. Assuming that the number of inserted submodules in arm  $j$  of phase  $k$ , is described by a function,  $n_{j,k}(t)$ , the total voltage inserted in the arm,  $v_{j,k}$ , can be described by eq. (2.1)

$$v_{j,k} = \sum_{i=1}^N v_{i,j,k} \approx n_{j,k}(t)v_{tot,j,k} \quad (2.1)$$

where  $v_{tot,j,k}$  is the sum of all the capacitor voltages in the arm and the modulation index follows  $0 \leq n_{j,k} \leq 1$ . Implicit in the last approximation of eq. (2.1) are two assumptions. First, there exists a balancing algorithm to ensure that all capacitor voltages are close to the average submodule voltage. Such balancing algorithms exist and are shown to work sufficiently for this assumption to be valid [49], [70]–[72]. Second, that the number of inserted capacitors can be modeled as a continuous function. This assumption is equivalent to assuming that there is an infinite number of submodules to be inserted. The validity of this assumption has been experimentally verified in [73], [74] as well as verified by comparing similar average models against more detailed discrete models in [47], [75]–[78].

It should be noted that [76]–[78] discovered that average models are inaccurate when modeling DC-faults because the models do not capture the submodules ability to enter a blocking state. However, since fault analysis is considered outside the scope of this thesis, no more attention is devoted to this inaccuracy. It is noted, however, that efforts were made to mitigate this problem in [50], [79], [80] which were somewhat successful. This lays a promising foundation in case the model is expanded in the future to model such faults.

Under these assumptions, the MMC can be modeled as in fig. 2.4 were the cascade-connected submodules in each arm are modeled as a controllable voltage source.

The electrical relationships of the model in fig. 2.4 serve as a basis for the converter model and can be described for any phase  $k$ . Applying Kirchoff's current law (KCL) at the node  $v_{c,k}$  yields eq. (2.2).

$$i_{g,k} = i_{u,k} - i_{l,k} \quad (2.2)$$

By assuming that the grid current is equally distributed between the upper and lower arms of a leg, the currents in the upper and lower arm can be described in terms of the

## 2.1 Modeling of the MMC

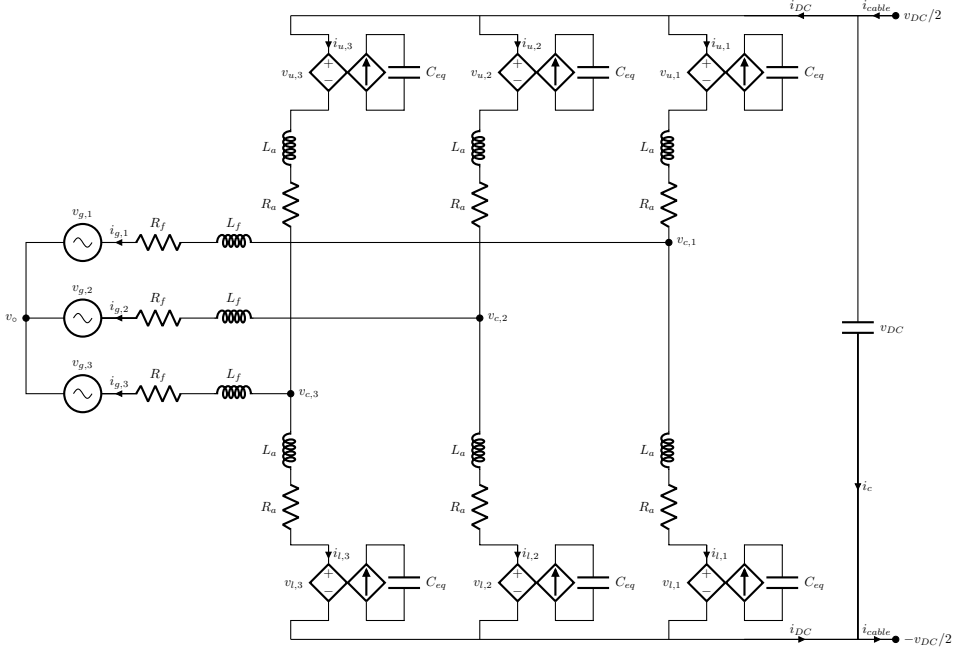


Figure 2.4: Model of a MMC

grid current and a circulating current by eqs. (2.3) and (2.4).

$$i_{u,k} = \frac{1}{2}i_{g,k} + i_{\circ,k} \quad (2.3)$$

$$i_{l,k} = -\frac{1}{2}i_{g,k} + i_{\circ,k} \quad (2.4)$$

By combining eqs. (2.3) and (2.4) the circulating current is described by eq. (2.5).

$$i_{\circ,k} = \frac{i_{u,k} + i_{l,k}}{2} \quad (2.5)$$

The converter voltage,  $v_{c,k}$ , can be described by using Kirchhoff's voltage law (KVL) along phase  $k$  from  $v_{c,k}$  to  $v_{DC}/2$  and  $-v_{DC}/2$ . By neglecting the voltage drop over the arm inductance and resistance, the relationships in eqs. (2.6) and (2.7) are produced:

$$v_{u,k} \approx \frac{v_{DC}}{2} - v_{c,k} \quad (2.6)$$

$$v_{l,k} \approx \frac{v_{DC}}{2} + v_{c,k} \quad (2.7)$$

Solving eqs. (2.6) and (2.7) for the converter voltage in phase  $k$  yields eq. (2.8).

$$v_{c,k} = \frac{v_{l,k} - v_{u,k}}{2} \quad (2.8)$$

Additionally, the voltage driving the circulating current can be described analogously to eq. (2.5) by eq. (2.9).

$$v_{\circ} = \frac{v_l + v_u}{2} \quad (2.9)$$

### 2.1.2 Specific modeling decisions

Assuming an average model, different researchers still make different decisions when designing MMC models. This relates to the focus points of the researchers. One challenge when modeling the MMC is how to handle the fact that different frequency components characterize different states. The challenge related to this is that if all variables are transformed in one rotating reference frame, then some variables will still be time-periodic in this reference frame; i.e., the system is not steady-state time-invariant (SSTI). It is possible to conduct stability analysis based on steady-state time-periodic (SSTP) average models, but this requires advanced methods specifically developed for time-periodic systems, by using a linear time-periodic reference frame [81].

Because such models require advanced methods that are currently not the industry standard, other approaches have been attempted to produce models that only contain variables which reach an equilibrium point in steady-state. One such approach applied dynamic phasor modeling to all the internal electrical states of the model of the MMC [82]. Such an approach does not entail the transformation of three-phase variables into a synchronous dq-reference frame to achieve a steady-state equilibrium but rather represents the waveforms in terms of complex Fourier coefficients which results in complicated high-order models. Another technique to circumvent the challenge of several frequency components is to neglect elements of the internal dynamics that are characterized by other frequencies than the fundamental frequency. For instance, [83] neglected the dynamic impact of the internal energy storage capabilities of the MMC and thus assumed

a perfect power balance between the AC- and DC-side. Other simplifications include reducing the MMC to a boost-buck converter with energy storage [40].

Further approaches include modeling the MMC under the assumption that a circulating current suppression control is applied [84]. These approaches are suitable when the modulation indexes are chosen based on the measured outputs of the control loops without taking into account the variations or oscillations of the capacitor voltages in the arms of the MMC. This is often called uncompensated modulation (UCM), which is juxtaposed with compensated modulation (CM), which does account for such oscillations. Uncompensated modulation has been determined not to be suitable for energy-based control strategies [85], which are investigated here. An overview of different modeling approaches used for the MMC is depicted in fig. 2.5

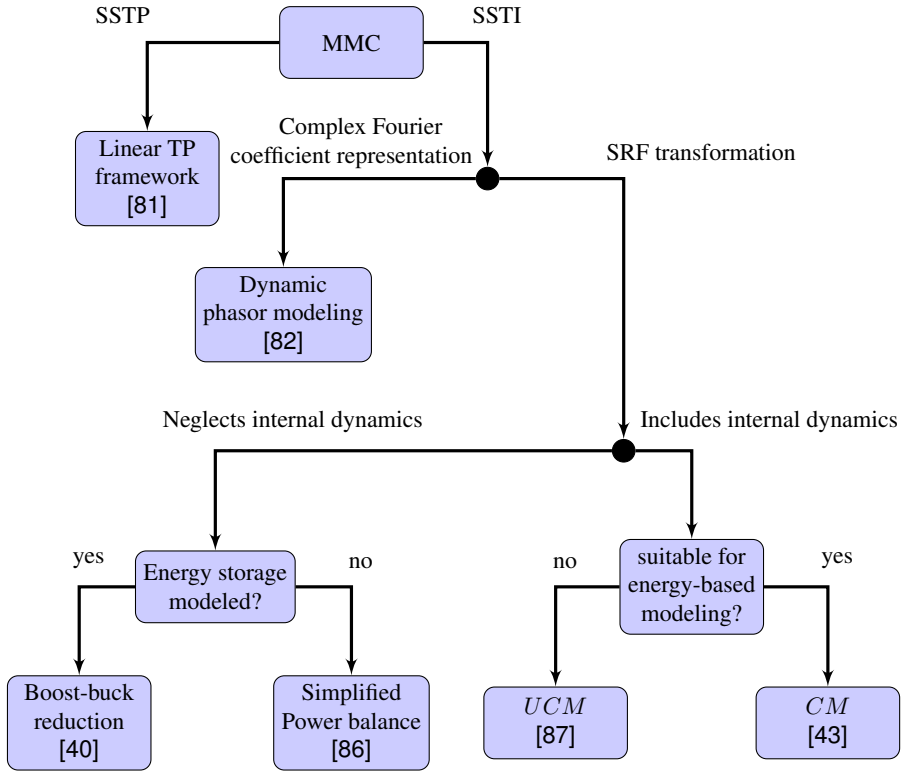


Figure 2.5: Different MMC modeling strategies used in the literature

### 2.1.3 The MMC model

This section aims to describe the mathematical modeling of the MMC, which will serve as the basis for the subsequent development of the control structure used in this thesis. The modeling process is broken down into four dynamics: the AC-side dynamics, the DC-side dynamics, the circulating current dynamics, and the internal energy storage dynamics. Because this model is developed as per industrial request, the variables that appear in the system equations need to reach an equilibrium point in steady-state so that traditional stability analysis can be applied to the model, using traditional techniques. Furthermore, since the model needs to be suited for energy-based modeling, compensated modulation will be assumed. Thus, the model developed subsequently is based on the models described in [43], [46].

#### Internal energy storage dynamics

The rate of change of the stored energy in the capacitors in the upper and lower arm in phase  $k$  can now be described by combining eqs. (2.3) and (2.4) into eqs. (2.10) and (2.11)

$$\frac{d}{dt}w_{u,k} = i_{u,k}v_{u,k} = \left(\frac{1}{2}i_{g,k} + i_{\circ}\right)v_{u,k} \quad (2.10)$$

$$\frac{d}{dt}w_{l,k} = i_{l,k}v_{l,k} = \left(-\frac{1}{2}i_{g,k} + i_{\circ}\right)v_{l,k} \quad (2.11)$$

By adding eqs. (2.10) and (2.11) and using eqs. (2.8) and (2.9), the rate of change of the sum of stored energy in the converter can be described, as in eq. (2.12).

$$\frac{d}{dt}\mathbf{w}_{\Sigma}^{123} = 2\mathbf{P}_{\circ,\circ}^{123} - \mathbf{P}_{g,c}^{123} \quad (2.12)$$

Where the two vectors  $\mathbf{P}_{\circ,\circ}^{123}$  and  $\mathbf{P}_{g,c}^{123}$  are defined according to eqs. (2.13) and (2.14).

$$\mathbf{P}_{\circ,\circ}^{123} = [i_{\circ,1}v_{\circ} \quad i_{\circ,2}v_{\circ} \quad i_{\circ,3}v_{\circ}]^T \quad (2.13)$$

$$\mathbf{P}_{g,c}^{123} = [i_{g,1}v_{c,1} \quad i_{g,2}v_{c,2} \quad i_{g,3}v_{c,3}]^T \quad (2.14)$$

Equation (2.12) can be understood as a power balance. The rate of change of the stored energy of the converter is the difference between the power flowing into the converter,  $2\mathbf{P}_{\circ,\circ}^{123}$ , and the power flowing out of the converter,  $\mathbf{P}_{g,c}^{123}$ . A further observation relates to the frequency of the terms in eq. (2.12). As can be seen in eq. (2.14), the power that drains the converter,  $\mathbf{P}_{g,c}^{123}$ , is the product of the grid current and the converter voltage. Because they both oscillate at grid frequency, their product oscillates at twice that frequency and in negative sequence. This can be shown by carrying out the multiplication and noting that the sign in front of the frequency changes and that the sequence changes from 1-2-3 to 3-2-1. Furthermore, the circulating current has been shown to have the same characteristics as the draining power. That is, the circulating current is characterized by a second-order harmonic as well as having negative sequence [88]. Additionally, the circulating voltage is assumed to be controlled to be equal to its reference as a result of compensated modulation as in [43], [45], [47], [74], [75], [89]. Thus, it is assumed that the circulating voltage can be chosen to share the characteristics of the circulating current mentioned above.

Because control of sinusoidally varying variables is more challenging than control of non-oscillating variables, it is chosen to transform all of the variables in eq. (2.12) into a reference frame rotating at the frequency of those variables, i.e.  $-2\omega$ . As will be shown, when described in such a  $dqz_{-2\omega}$ -reference frame, the power draining the converter,  $\mathbf{P}_{g,c}^{dqz-2\omega}$ , appears to be a DC-signal, while the power entering the converter,  $\mathbf{P}_{\circ,\circ}^{dqz-2\omega}$ , only has a negligible sixth-order harmonic. The definition of the transformation matrix,  $\mathbf{T}$ , used in this thesis for this transformation can be found in section B.9. Thus eq. (2.12) can be rewritten in a reference frame that rotates at twice the frequency of the grid frequency by using eqs. (2.15) to (2.17).

$$\mathbf{w}_{\Sigma}^{123} = \mathbf{T}_{-2\omega}^{-1} \mathbf{w}_{\Sigma}^{dqz-2\omega} \quad (2.15)$$

$$\mathbf{P}_{\circ,\circ}^{123} = \mathbf{T}_{-2\omega}^{-1} \mathbf{P}_{\circ,\circ}^{dqz-2\omega} \quad (2.16)$$

$$\mathbf{P}_{g,c}^{123} = \mathbf{T}_{-2\omega}^{-1} \mathbf{P}_{g,c}^{dqz-2\omega} \quad (2.17)$$

By inserting eqs. (2.15) to (2.17) into eq. (2.12), using the chain rule, and left-multiplying with  $\mathbf{T}_{-2\omega}$ , the energy sum vector can be expressed in its synchronous reference frame

according to eq. (2.18).

$$\frac{d}{dt} \mathbf{w}_{\Sigma}^{dqz-2\omega} = 2\mathbf{P}_{\circ,\circ}^{dqz-2\omega} - \mathbf{P}_{g,c}^{dqz-2\omega} - \mathbf{T}_{-2\omega} \frac{d}{dt} \mathbf{T}_{-2\omega}^{-1} \mathbf{w}_{\Sigma}^{dqz-2\omega} \quad (2.18)$$

Using a similar transformation matrix (see, eq. (B.2)), the grid current vector in the 123-reference frame,  $\mathbf{i}_g^{123}$ , and the converter voltage vector in the same reference frame,  $\mathbf{v}_c^{123}$ , can be described in terms of their dqz-reference frame components.

$$\mathbf{i}_g^{abc} = \mathbf{T}_{\omega}^{-1} \mathbf{i}_g^{dqz\omega} \quad (2.19)$$

$$\mathbf{v}_c^{abc} = \mathbf{T}_{\omega}^{-1} \mathbf{v}_c^{dqz\omega} \quad (2.20)$$

By expanding eq. (2.17) and substituting in eqs. (2.19) and (2.20),  $\mathbf{P}_{g,c}^{dqz-2\omega}$  can be expressed as in eq. (2.21). This is shown in section C.1 eq. (5).

$$\Rightarrow \mathbf{P}_{g,c}^{dqz-2\omega} = \frac{1}{2} \begin{bmatrix} i_{g,d}v_{c,d} - i_{g,q}v_{c,q} \\ -i_{g,d}v_{c,q} - i_{g,q}v_{c,d} \\ i_{g,d}v_{c,d} + i_{g,q}v_{c,q} \end{bmatrix} \quad (2.21)$$

Similarly, the expression for  $\mathbf{P}_{\circ,\circ}^{dqz-2\omega}$  can be expressed in the  $dqz-2\omega$ -reference frame. Analogous to the grid current and converter voltage, the circulating current and voltage can be expressed in their reference frame by eqs. (2.22) and (2.23).

$$\mathbf{i}_{\circ}^{123} = \mathbf{T}_{-2\omega}^{-1} \mathbf{i}_{\circ}^{dqz-2\omega} \quad (2.22)$$

$$\mathbf{v}_{\circ}^{123} = \mathbf{T}_{-2\omega}^{-1} \mathbf{v}_{\circ}^{dqz-2\omega} \quad (2.23)$$

Thus,  $\mathbf{P}_{\circ,\circ}^{dqz-2\omega}$  can be expressed in its synchronous reference frame by combining eqs. (2.16), (2.22) and (2.23). This is shown in section C.1 eqs. (6) and (7).

$$\Rightarrow \mathbf{P}_{\circ,\circ}^{dqz-2\omega} = \begin{bmatrix} i_{\circ,d}v_{\circ,z} + i_{\circ,z}v_{\circ,d} \\ i_{\circ,q}v_{\circ,z} + i_{\circ,z}v_{\circ,q} \\ v_{\circ,z}i_{\circ,z} \end{bmatrix} \quad (2.24)$$

The derivation of eq. (2.24) requires a simplification. Since second-order harmonics char-

acterize both the circulating voltage and the circulating current, their product should contain a fourth-order harmonic that would appear as a sixth-order harmonic when transformed to  $dqz_{-2\omega}$ -reference frame. However, the coefficient of these terms will only consist of the product of d- and q-components of the circulating current and voltage. Since these terms are significantly smaller than the zero-sequence terms, they are neglected [43].

The coupling matrix  $\mathbf{J}_{-2\omega} = \mathbf{T}_{-2\omega} \frac{d}{dt} \mathbf{T}_{-2\omega}^{-1}$  in eq. (2.18) can also be found according to eq. (2.25), see section C.2.

$$\mathbf{J}_{-2\omega} = \begin{bmatrix} 0 & 2\omega & 0 \\ -2\omega & 0 & 0 \\ 0 & 0 & 0 \end{bmatrix} \quad (2.25)$$

Thus, the energy sum vector can be expressed according to eq. (2.26)

$$\frac{d}{dt} \mathbf{w}_{\Sigma}^{dqz_{-2\omega}} = 2 \begin{bmatrix} i_{\circ,d} v_{\circ,z} + i_{\circ,z} v_{\circ,d} \\ i_{\circ,q} v_{\circ,z} + i_{\circ,z} v_{\circ,q} \\ v_{\circ,z} i_{\circ,z} \end{bmatrix} - \frac{1}{2} \begin{bmatrix} i_{g,d} v_{c,d} - i_{g,q} v_{c,q} \\ -i_{g,d} v_{c,q} - i_{g,q} v_{c,d} \\ i_{g,d} v_{c,d} + i_{g,q} v_{c,q} \end{bmatrix} - \begin{bmatrix} 0 & 2\omega & 0 \\ -2\omega & 0 & 0 \\ 0 & 0 & 0 \end{bmatrix} \mathbf{w}_{\Sigma}^{dqz_{-2\omega}} \quad (2.26)$$

## AC-side dynamics

The dynamics of the grid current and converter voltage must be described to provide a basis for the grid side current controller. Moreover, this will simplify the modeling of the system by modeling each leg of the MMC instead of both arms. By using KVL from the grid voltage to the upper and lower arm voltage respectively, eqs. (2.27) and (2.28) are derived.

$$\mathbf{v}_g^{123} = -R_f \mathbf{i}_g^{123} - L_f \frac{d}{dt} \mathbf{i}_g^{123} - R_a \mathbf{i}_u^{123} - L_a \frac{d}{dt} \mathbf{i}_u^{123} - \mathbf{v}_u^{123} \quad (2.27)$$

$$\mathbf{v}_g^{123} = -R_f \mathbf{i}_g^{123} - L_f \frac{d}{dt} \mathbf{i}_g^{123} + R_a \mathbf{i}_l^{123} + L_a \frac{d}{dt} \mathbf{i}_l^{123} + \mathbf{v}_l^{123} \quad (2.28)$$

Adding eqs. (2.27) and (2.28) yields eq. (2.29).

$$2\mathbf{v}_g^{123} = -2R_f \mathbf{i}_g^{123} - 2L_f \frac{d}{dt} \mathbf{i}_g^{123} - R_a (\mathbf{i}_u^{123} - \mathbf{i}_l^{123}) - L_a \frac{d}{dt} (\mathbf{i}_u^{123} - \mathbf{i}_l^{123}) - (\mathbf{v}_u^{123} - \mathbf{v}_l^{123}) \quad (2.29)$$

which can be simplified using eqs. (2.2) and (2.8) and by introducing  $R_v = R_f + \frac{1}{2}R_a$  and  $L_v = L_f + \frac{1}{2}L_a$  into eq. (2.30).

$$\mathbf{v}_g^{123} = -R_v \mathbf{i}_g^{123} - L_v \frac{d}{dt} \mathbf{i}_g^{123} + \mathbf{v}_c^{123} \quad (2.30)$$

Using eqs. (2.19) and (2.20) and a similar transformation for the grid voltage, eq. (2.30) can be written in the dqz $\omega$ -reference frame according to eq. (2.31).

$$\mathbf{v}_g^{dqz\omega} = -R_v \mathbf{i}_g^{dqz\omega} - L_v \frac{d}{dt} \mathbf{i}_g^{dqz\omega} + \mathbf{v}_c^{dqz\omega} - L_v \mathbf{T}_\omega \frac{d}{dt} (\mathbf{T}_\omega^{-1}) \mathbf{i}_g \quad (2.31)$$

Thus the grid current dynamics can be described by eq. (2.32)

$$L_v \frac{d}{dt} \begin{bmatrix} i_{g,d} \\ i_{g,q} \end{bmatrix} = -R_v \begin{bmatrix} i_{g,d} \\ i_{g,q} \end{bmatrix} + \begin{bmatrix} v_{c,d} \\ v_{c,q} \end{bmatrix} - \begin{bmatrix} v_{g,d} \\ v_{g,q} \end{bmatrix} - L_v \begin{bmatrix} 0 & -\omega \\ \omega & 0 \end{bmatrix} \begin{bmatrix} i_{g,d} \\ i_{g,q} \end{bmatrix} \quad (2.32)$$

## Circulating current dynamics

It is important to describe the dynamics that govern the circulating current so that effective controllers can be developed. Furthermore, since the dynamics of the circulating voltage is coupled with the DC-side voltage, this description nicely facilitates modeling of the DC-side by using the circulating voltage.

The central relationship relating to this dynamic is found using KVL from the circulating voltage to the DC terminal and only considering the voltage drop over the arm inductor and resistor as a consequence of the circulating current. This current is driven by the circulating voltage. The equations governing the circulating current can be described in the 123-reference frame by eq. (2.33).

$$\mathbf{v}_\circ^{123} = -R_a \mathbf{i}_\circ^{123} - L_a \frac{d}{dt} \mathbf{i}_\circ^{123} + \frac{v_{DC}}{2} \begin{bmatrix} 1 & 1 & 1 \end{bmatrix}^T \quad (2.33)$$

eq. (2.33) can be transformed into a synchronous reference frame by inserting eqs. (2.22) and (2.23), using the chain rule, and left-multiplying with  $\mathbf{T}_\omega$ .

$$L_a \frac{d}{dt} \mathbf{i}_\circ^{dqz} = - \left( R_a \mathbf{I} + L_a \mathbf{T}_{-2\omega} \frac{d}{dt} (\mathbf{T}_{-2\omega}^{-1}) \right) \mathbf{i}_\circ^{dqz} - \mathbf{v}_\circ^{dqz} + \frac{v_{DC}}{2} \begin{bmatrix} 1 & 1 & 1 \end{bmatrix}^T \quad (2.34)$$

Which simplifies into eq. (2.35).

$$L_a \frac{d}{dt} \mathbf{i}_\circ^{dqz} = - \begin{bmatrix} R_a & 2\omega L_a & 0 \\ -2\omega L_a & R_a & 0 \\ 0 & 0 & R_a \end{bmatrix} \mathbf{i}_\circ^{dqz} - \mathbf{v}_\circ^{dqz} + \frac{v_{DC}}{2} \begin{bmatrix} 1 \\ 1 \\ 1 \end{bmatrix} \quad (2.35)$$

### DC-side dynamics

The DC-side dynamics are primarily chosen to describe the coupling of the DC voltage and the AC-side grid current, because the voltage controller will determine  $i_{g,d,ref}$ .

First, the dynamics of  $i_{g,d}$  and  $v_{DC}$  are expressed. This is done by considering an energy balance, where the losses in the converter resistances are neglected. This is done by considering the zero-sequence component of the energy sum of the converter, described by eq. (2.26), the power flowing out of the converter, the power charging the DC-side capacitor, and the power flowing into the converter. This relationship is expressed in eq. (2.36).

$$i_{cable} v_{DC} = i_c v_{DC} + 3 \frac{d}{dt} w_{\Sigma,z} + \frac{3}{2} (i_{g,d} v_{c,d} + i_{g,q} v_{c,q}) \quad (2.36)$$

where  $i_{cable}$  is the current flowing in the DC-cable and  $i_c$  is the current flowing into DC-side capacitor. The factor of 3 in front of  $w_{\Sigma,z}$  is because there are three legs and is thus a result of the definition of the zero-sequence energy sum. The factor of  $\frac{3}{2}$  is a result of the choice of an amplitude invariant reference frame transformation. Moreover, the dynamics relating to the DC current must be described. Using KCL at the node connecting the DC-capacitor to the DC terminals, eq. (2.37) is derived.

$$i_{cable} = i_c + i_{DC} \quad (2.37)$$

**Summary of the system equations**

Because the model only needs to be accurate with regards to the terminal behavior of the converter, the only equations of interest are the ones describing the DC-components of the circulating current and energy sum of the converter. Thus, only the zero-sequence component of eqs. (2.26) and (2.35) are considered system equations, together with the grid current dynamics and DC voltage dynamics described by eqs. (2.32), (2.36) and (2.37). These six system equations are summarized in eqs. (2.38) to (2.43).

$$L_v \frac{d}{dt} i_{g,d} = -R_v i_{g,d} + v_{c,d} - v_{g,d} + L_v \omega i_{g,q} \quad (2.38)$$

$$L_v \frac{d}{dt} i_{g,q} = -R_v i_{g,q} + v_{c,q} - v_{g,q} - L_v \omega i_{g,d} \quad (2.39)$$

$$L_a \frac{d}{dt} i_{\circ,z} = -R_a i_{\circ,z} + \frac{1}{2} v_{DC} - v_{\circ,z} \quad (2.40)$$

$$\frac{d}{dt} w_{\Sigma,z} = -\frac{1}{2} (i_{g,d} v_{c,d} + i_{g,q} v_{c,q}) + 2v_{\circ,z} i_{\circ,z} \quad (2.41)$$

$$i_{cable} v_{DC} = i_c v_{DC} + 3 \frac{d}{dt} w_{\Sigma,z} + \frac{3}{2} (i_{g,d} v_{c,d} + i_{g,q} v_{c,q}) \quad (2.42)$$

$$i_{cable} = i_c + 3i_{\circ} \quad (2.43)$$

A drawn model overview is depicted in fig. 2.6 with controllers.

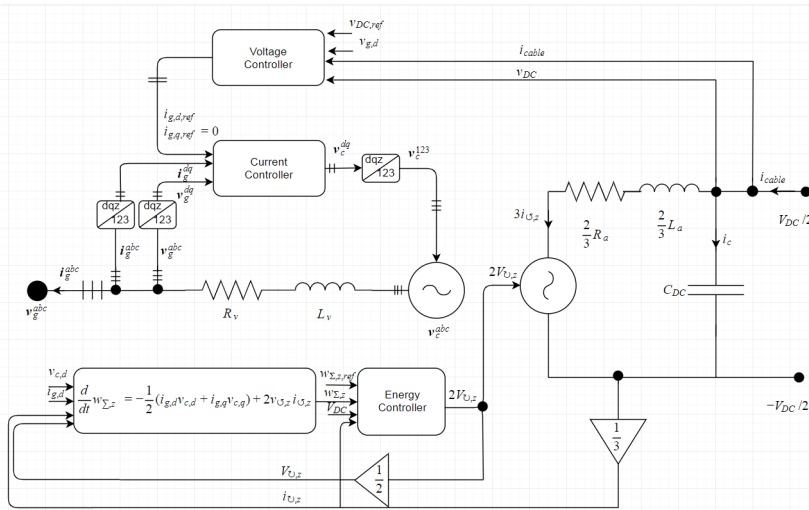


Figure 2.6: Overview of the MMC model

## 2.2 Control of MMC

The challenge of controlling the MMC can be broken down into three sub-problems. The current controller controls the grid currents, the energy controller controls the zero-sequence energy sum, and the voltage controller controls the DC-side voltage. Note that the energy controller encompasses the circulating current controller. All of these controllers use the same control philosophy in that disturbances are compensated for by feed-forwards, and the remaining system is controlled using a PI controller.

This is not the only technique used in the literature regarding how to control an MMC. First and foremost, virtually all MMC control designs can *either* control the DC voltage or the active power flowing through the converter. In addition to this, they can independently control the reactive power flow. In this thesis, the current component reference associated with reactive power flow is set to zero. This allows the dynamics of interest to be studied in isolation as well as simplifying the modeling. Furthermore, only the controller associated with the DC voltage, not the active power flow, is explained in this thesis. This is because the same control principle can be applied to active power flow, the only difference being multiplying with the DC current.

Furthermore, several researchers do not specify a controller for the zero-sequence energy of the controller. Since this thesis aims explicitly to investigate dynamic improvements related to control of this energy, such approaches are not adopted here.

There is some variation with regards to the control topology used in the literature by researchers that explicitly use energy controllers. One such approach used the energy controller in the outer-loop to produce the AC-side grid current reference, and a DC-current controller produces the circulating voltage reference [51]. Another approach is used in [75], where the output of the energy controller is used in tandem with a voltage controller to produce the grid voltage references. The arguably most common approach, however, uses a different hierarchy where the energy controller outputs a reference that directly relates to one of the two DC-variables,  $i_{DC}$  or  $v_{DC}$  [43], [44], [46], [47], [54], [55], [90]. This is then typically coupled with an outer-loop power/voltage controller

with DC Droop which determines the reference for the AC-side grid current controller. Figure 2.7 gives an overview of some of the control strategies used in the literature with some examples.

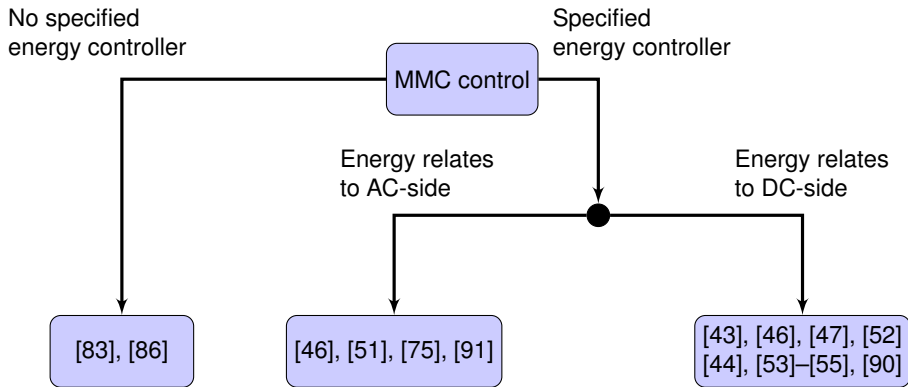


Figure 2.7: Different MMC control strategies used in the literature

Typically, when the energy controller relates to the AC-side, the voltage controller determines the reference for the circulating current. This can effectively decouple the DC voltage and the zero-sequence energy sum, and it decouples the AC- and DC-side of the converter, which allows for independent tuning. This was shown in [46].

The control structure used in this thesis, however, retains the most commonly applied control hierarchy, but aims to investigate the potential for decoupling  $w_{\Sigma,z}$  and  $v_{DC}$  by introducing a feed-forward term in the voltage controller. That is, the energy controller is used to determine the reference for the circulating current controller. The circulating current controller, in turn, produces the reference for the circulating voltage which is used to model the DC-side of the converter. Additionally, the voltage controller determines the reference for the d-component of the grid side current, which is controlled using the current controller. This current controller produces the references for the converter voltage which is modeled using a controllable voltage source, see fig. 2.6. To investigate the decoupling, the voltage controller used in this thesis is not based on droop control, but rather on model inversion.

### 2.2.1 Current controller

The current controller aims to produce the references for the converter voltages,  $v_{c,d}$  and  $v_{c,q}$ , so that the AC-side currents follow their references. The equations governing the current dynamics are recalled from eqs. (2.38) and (2.39), but rephrased in p.u. in accordance with section B.1 in eq. (2.44).

$$\underbrace{\frac{L_{v,pu}}{\omega_{base}} \frac{d}{dt} \begin{bmatrix} i_{g,d,pu} \\ i_{g,q,pu} \end{bmatrix} + R_{v,pu} \begin{bmatrix} i_{g,d,pu} \\ i_{g,q,pu} \end{bmatrix}}_{System} = \begin{bmatrix} v_{c,d,pu} \\ v_{c,q,pu} \end{bmatrix} - \underbrace{\left( \begin{bmatrix} v_{g,d,pu} \\ v_{g,q,pu} \end{bmatrix} + L_{v,pu} \begin{bmatrix} 0 & -1 \\ 1 & 0 \end{bmatrix} \begin{bmatrix} i_{g,d,pu} \\ i_{g,q,pu} \end{bmatrix} \right)}_{Disturbance} \quad (2.44)$$

It is clear from eq. (2.44) that the feed-forward terms used to cancel the disturbance,  $\mathbf{ff}_{cc}$ , are described by eq. (2.45). The current controller is depicted in fig. 2.8.

$$\mathbf{ff}_{cc} = \begin{bmatrix} v_{g,d,pu} \\ v_{g,q,pu} \end{bmatrix} + L_{v,pu} \begin{bmatrix} 0 & -1 \\ 1 & 0 \end{bmatrix} \begin{bmatrix} i_{g,d,pu} \\ i_{g,q,pu} \end{bmatrix} \quad (2.45)$$

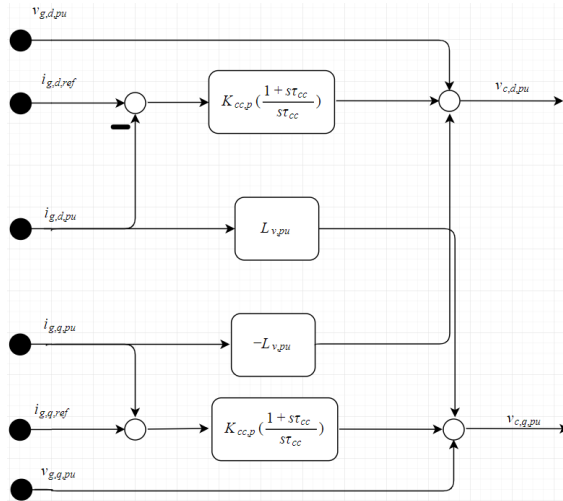


Figure 2.8: Current controller

### Tuning of the current controller

Since the remaining system is the same for both the d- and q-axis component, only the control for the d-axis current is derived as an example. Assuming the disturbance is perfectly compensated by the feed-forward, the control loop is depicted in fig. 2.9.

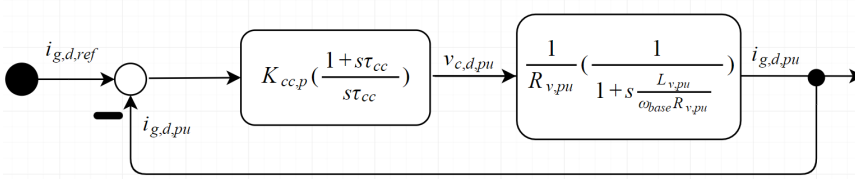


Figure 2.9: Current control loop

The system is found from eq. (2.44). The transfer function of that system can be found by solving the remaining equation for  $i_{g,d,pu}/v_{c,d,pu}$  and then Laplace transforming that equation.  $\tau_{cc}$  is chosen to cancel the pole of the system,  $1 + \frac{L_{v,pu}}{R_{v,pu}\omega_{base}}s$ , and is thus chosen according to eq. (2.46)

$$\tau_{cc} = \frac{K_{cc,p}}{K_{cc,i}} = \frac{L_{v,pu}}{R_{v,pu}\omega_{base}} \quad (2.46)$$

By using eq. (2.46), the remaining closed loop transfer function can be found according to eq. (2.47)

$$G_{cl,cc} = \frac{1}{1 + s\tau_{eq,cc}} \quad (2.47)$$

where  $\tau_{eq,cc}$  is the equivalent time-constant of the entire current control loop defined according to eq. (2.48)

$$\tau_{eq,cc} = \frac{R_{v,pu}}{K_{cc,i}} \quad (2.48)$$

Thus, by assuming that the time constant of the current controller is determined according to the speed requirements of the controller, the appropriate proportional and integral control gains are found according to eq. (2.49) by combining eqs. (2.46) and (2.48).

$$\begin{bmatrix} K_{cc,p} \\ K_{cc,i} \end{bmatrix} = \frac{1}{\tau_{eq,cc}} \begin{bmatrix} L_{v,pu}/\omega_{base} \\ R_{v,pu} \end{bmatrix} \quad (2.49)$$

### 2.2.2 Energy controller

The task of the energy controller is to produce the reference for the circulating voltage to ensure that the zero-sequence energy sum is at its reference. This is done in two steps. Initially, the circulating current reference is calculated by a PI-controller. Then, the circulating current is controlled by another PI controller to produce the correct reference for the circulating voltage.

To understand the control of the circulating current, the relevant dynamics from eq. (2.40) are recalled in eq. (2.50) in p.u.

$$-\underbrace{\left(\frac{L_{a,pu}}{\omega_{base}} \frac{d}{dt} i_{\odot,z,pu} + R_{a,pu} i_{\odot,z,pu}\right)}_{System} = v_{\odot,z,pu} - \underbrace{\frac{1}{2} v_{DC,pu}}_{Disturbance} \quad (2.50)$$

Similar to the case with the grid current controller, the disturbance is controlled by adding a feed-forward term,  $ff_{\odot cc}$ , to the circulating voltage reference. Thus the feed-forward term is found according to eq. (2.51)

$$ff_{\odot cc} = \frac{1}{2} v_{DC,pu} \quad (2.51)$$

The energy controller is depicted in fig. 2.10.

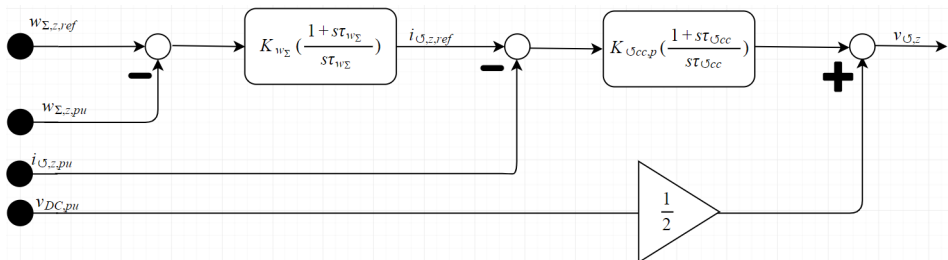


Figure 2.10: Energy controller

### Tuning of Energy controller

Through inspection of eq. (2.50) it is immediately clear that the circulating current can be controlled and tuned using the same principle that was used to control the grid current. Thus, the gains of the PI controller are found according to eq. (2.52).

$$\begin{bmatrix} K_{\circ cc,p} \\ K_{\circ cc,i} \end{bmatrix} = \frac{1}{\tau_{eq,\circ cc}} \begin{bmatrix} -L_{a,pu}/\omega_{base} \\ -R_{a,pu} \end{bmatrix} \quad (2.52)$$

It should be noted that small-signal analysis of this converter model was conducted in [43] which found that if the AC grid is weak, then reducing  $K_{\circ cc,p}$  to 80% of the value calculated in eq. (2.52) improves stability.

The gains used in the outer PI controller,  $K_{w\Sigma,p}$  and  $K_{w\Sigma,i}$ , are difficult to derive analytically due to the non-linear nature of the relationship between the energy sum and the circulating current. Luckily, [43] conducted a stability analysis of the same MMC model and used gains of 10 p.u. Since these gains did not emerge as causes of instability in their paper, this theses initially used them as well, under the assumption that they could be re-tuned later. However, the simulations showed that the system quickly became stable when using these gains and, thus, they were not re-tuned.

The last remaining question now relates to how to determine  $w_{\Sigma,z,ref}$ . For this, two different controllers will be described, each designed for a specific purpose. In chapter 4 simulations will be carried out to investigate the degree to which these controllers are effective in their tasks. Based on this, a discussion is conducted in chapter 5 to determine for which purpose the stored energy in the MMC should be controlled.

### Purpose 1: Smoothen out turbine dynamics caused by wind fluctuations

The goal of the controller is to reduce the stored energy when the power from the turbine is below rated value, to compensate for that lack of energy. Assuming no error between

the power produced by the turbine and its reference, the controller should output 1. Because too rapid alterations in  $w_{\Sigma,z}$  would have a negative impact on the power profile by causing too many fluctuations, a delay is added. The gains of the PI controller and time constant of the delay were found experimentally and are listed in table B.3. If the controller could completely deplete the MMC of its energy by setting  $w_{\Sigma,z}$  to 0, then the converter could not function properly. Therefore a limiter is added to ensure that  $0.7 \leq w_{\Sigma,z,pu} \leq 1.3$ .

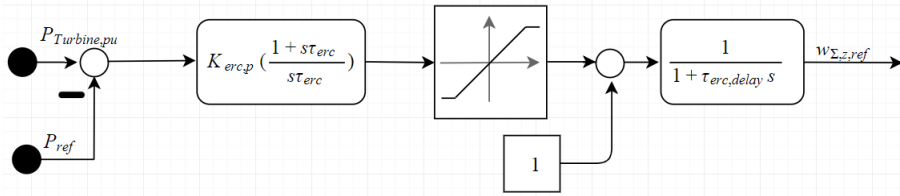


Figure 2.11: Controller used to determine the energy reference

### Purpose 2: Reduce power step response time

The idea behind this controller is to release energy upon a step up in power reference or to absorb energy in the event of a step-down. Thus, in the period immediately following this step change, the converter can supply the power difference, i.e., the difference between the power flowing into the converter and the power reference it aims to provide. Due to the concrete relationship between an error in power and energy, a controller characterized by its integral gain can be utilized efficiently according to eq. (2.53).

$$\Delta w_{\Sigma,z,ref} = \frac{S_{base}}{3w_{base}} \int_{t_{step}}^{t_{step}+t} (P - P_{ref}) dt \quad (2.53)$$

which is recognized as an integral controller with an integral gain of  $-\frac{S_{base}}{3w_{base}}$ . However, performance can be improved by reducing the integral gain and introducing a proportional term. This is because this reduces the oscillations associated with the integral term and reduces the response time due to the fast nature of the proportional term. Thus a PI is implemented using a proportional gain of  $-0.0004 \frac{S_{base}}{3w_{base}}$  and an integral gain of  $-0.7 \frac{S_{base}}{3w_{base}}$  where the ratio of integral to proportional gain was found experimentally.

### 2.2.3 Voltage controller

Even though the control strategy used in this thesis is inspired by [43], the implemented voltage controller is different. [43] used droop control, a common choice for increased reliability used by researchers and in the industry [36], [44], [47], [69], [92], [93]. However, since the system model only includes three terminals, and fault analysis is outside the scope of the thesis, droop control is not adopted in this thesis. Furthermore, this allows for an adaptation of a feed-forward technique to reduce the coupling between the DC voltage and the zero-sequence energy sum.

To describe the voltage controller, the dynamics of the DC voltage is first recalled from eq. (2.42). At this point, one simplifying assumption is made, namely that the impact of  $i_{g,q,pu}v_{c,q,pu}$  is negligible compared to  $i_{g,d,pu}v_{c,d,pu}$ . This assumption is valid almost always because the angular difference between  $v_{c,q}$  and  $v_{g,q}$  is very small and  $v_{g,q}$  is always 0 under the dq-transformation described in eq. (B.1) because the grid-voltage vector is aligned with  $v_{g,d}$ . In essence, this assumption is equivalent to neglecting the dynamics introduced by  $L_v$  with regards to  $v_{c,q}$ . By replacing the variables remaining in eq. (2.42) with the p.u. equivalents and isolating  $i_{g,d,pu}$ , eq. (2.42) is rephrased in p.u. in eq. (2.54).

$$\underbrace{-\frac{8v_{DC,pu}}{3v_{c,d,pu}} \frac{C_{DC,pu}}{\omega_{base}} \frac{d}{dt} v_{DC,pu}}_{System} = i_{g,d,pu} - \underbrace{i_{cable,pu} \frac{v_{DC,pu}}{v_{c,d,pu}} + \frac{2w_{base}}{S_{base}v_{c,d,pu}} \frac{d}{dt} w_{\Sigma,z,pu}}_{Disturbance} \quad (2.54)$$

The,  $\frac{2w_{base}}{S_{base}v_{c,d}} \frac{d}{dt} w_{\Sigma,z}$ -term is initially neglected in the control. There are two reasons why this *might* be considered prudent. Firstly, it might be argued that because  $w_{base}/S_{base} \ll 1$ , it is negligible and superfluous in the control. Secondly, as for any feed-forward term, its inclusion could cause *instability* due to imperfections in the model. Its inclusion is investigated in section 4.5, by comparing this controller to a controller that does include the term. The feed-forward,  $ff_{vc}$ , is, therefore, initially, expressed by eq. (2.55).

$$ff_{vc} = i_{cable,pu} \frac{v_{DC,pu}}{v_{c,d,pu}} \quad (2.55)$$

The voltage controller is depicted in fig. 2.12.

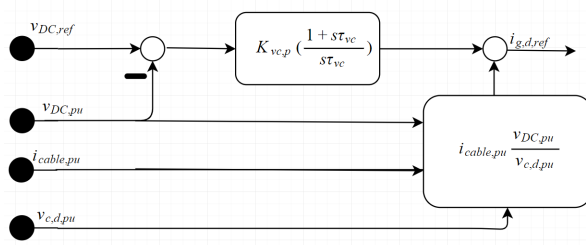


Figure 2.12: Voltage controller

### Tuning of the voltage controller

The tuning of the controller is done in two steps. First, simplifications are made to formulate the dynamics related to the control loop in a way that allows for analytic expression for the gains. Secondly, these gains are found based on an analysis of the closed loop transfer function. However, as will be evident, because the simplifications introduce inaccuracies, some re-tuning is expected after the initial simulations. Thus, these analytical expressions are best conceived as starting points for further re-tuning while also providing insights into the dynamics of the control loop.

For the tuning of the voltage controller, two assumptions are made. First, everything considered a disturbance is neglected under the assumption that they are either perfectly handled by a feed-forward or negligible. Second, it is assumed that entire current control loop can be modeled as a delay with time-constant  $\tau_{eq}$ , see eq. (2.47). Under these assumptions, the system to be controlled is derived by solving for  $\frac{v_{DC,pu}}{i_{g,d,pu}}$  in eq. (2.54). The remaining control loop is depicted in fig. 2.13

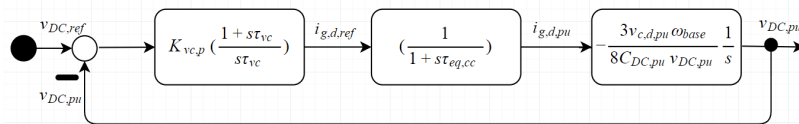


Figure 2.13: Voltage control loop

## Chapter 2. Modeling of the HVDC system

As can be seen in fig. 2.13 the open loop transfer function,  $G_{vc,ol}$  can be expressed as in eq. (2.56).

$$G_{vc,ol} = K_{vc,p} \frac{1 + s\tau_{vc}}{s\tau_{vc}} \frac{1}{1 + s\tau_{eq}} \left( -\frac{3v_{c,d,pu}\omega_{base}}{8C_{DC,pu}v_{DC,pu}} \frac{1}{s} \right) \quad (2.56)$$

where  $K_{vc,p}$  and  $\tau_{vc}$  are the proportional gain and time constant of the PI controller used. The implemented control is symmetrical optimum to ensure that there is never a zero in the denominator of the closed loop transfer function [94]. This is done by ensuring that the open-loop transfer function is never -1, by ensuring that the phase of the open-loop transfer function is as far away from  $-180^\circ$  ( $-1$ ) as possible when the amplitude is  $0\text{dB} = 1$ , see fig. 2.14.

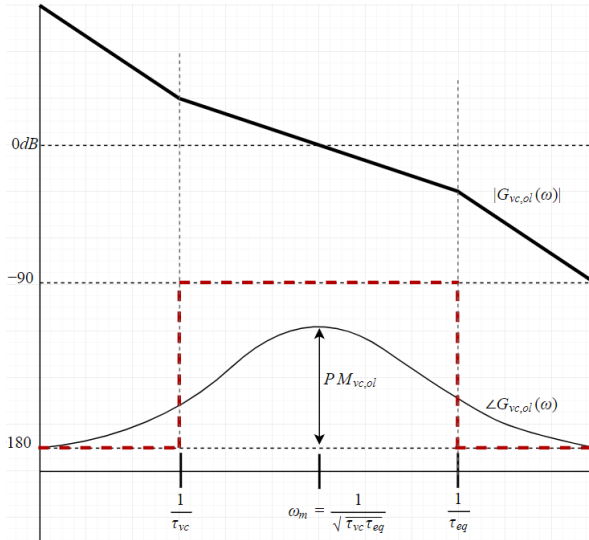


Figure 2.14: Gain,  $|G_{vc,ol}(\omega)|$ , and phase  $\angle G_{vc,ol}(\omega)$  of the open loop transfer function of the voltage controller. The gain is illustrated using asymptotes. The asymptotes of the phase is drawn in dotted red.

As can be seen eq. (2.56) the open-loop transfer function has a double pole in the origin meaning that its phase will be close to  $-180^\circ$  for small values of  $\omega$ . Additionally, the open-loop transfer function consists of one zero which elevates the phase towards  $-90^\circ$  and one pole which lowers the phase towards  $-180^\circ$ . Because the zero and the pole are described by the inverse of the time constant of the PI controller,  $\frac{1}{\tau_{vc}}$ , and the delay,  $\frac{1}{\tau_{eq}}$ , respectively, the phase of the open-loop transfer function peaks at the geometric

mean of the inverse of these time-constants. This can be proven by replacing  $s$  with  $j\omega$  in eq. (2.56) and splitting the real and imaginary part of the open-loop transfer function, see eq. (2.57).

$$G_{vc,ol} = -K_{vc,p} \frac{3v_{c,d,pu}\omega_{base}}{8C_{DC,pu}v_{DC,pu}} \tau_{vc} \left( \frac{1 + \omega^2 \tau_{vc} \tau_{eq}}{\omega^2 \tau_{vc}^2 + \omega^4 \tau_{vc}^2 \tau_{eq}^2} + j \frac{\omega \tau_{vc} - \omega \tau_{eq}}{\omega^2 \tau_{vc}^2 + \omega^4 \tau_{vc}^2 \tau_{eq}^2} \right) \quad (2.57)$$

Then, by taking the signs of the numerator and denominator into account in accordance with [95] and adding  $360^\circ$  to get the phase angle in the desired range between  $0$  and  $360^\circ$ , the phase margin of the open-loop transfer function is described by eq. (2.58)

$$PM_{vc,ol} = 180 - \left| \left( 180 - \arctan \left( \frac{\omega \tau_{vc} - \omega \tau_{eq}}{1 + \omega^2 \tau_{vc} \tau_{eq}} \right) \right) \right| \quad (2.58)$$

From eq. (2.58) it is clear that a maximum phase margin is achieved by having the zero-crossing frequency when eq. (2.58) is at its peak. Since  $\arctan$  is a strictly increasing function, this is found by differentiating the expression inside the  $\arctan$ -function with respect to the angular frequency and setting that equal to zero and solving for the angular frequency. It is found that the zero-crossing frequency,  $\omega_m$ , is expressed by eq. (2.59).

$$\omega_m = \frac{1}{\sqrt{\tau_{vc} \tau_{eq}}} \quad (2.59)$$

which is recognized as the geometrical mean of the inverse of the two time constants. By inserting eq. (2.59) into eq. (2.57) and using the fact that the amplitude at the zero crossing is equal to  $1(0\text{dB})$ , the proportional gain is described by eq. (2.60)

$$K_{vc,p} = -\frac{8C_{DC,pu}v_{DC,pu}}{3v_{c,d,pu}\omega_{base}\sqrt{\tau_{vc}\tau_{eq}}} \quad (2.60)$$

The time constant can also be found by choosing a desired phase margin and inserting eq. (2.59) into eq. (2.58). A phase margin of  $45^\circ$  gives  $\tau_{vc} = (3 + 2\sqrt{2})\tau_{eq}$ . By using this result, the proportional and integral gains can be expressed by eq. (2.61)

$$\begin{bmatrix} K_{vc,p} \\ K_{vc,i} \end{bmatrix} = -\frac{8C_{DC,pu}v_{DC,pu}}{3\omega_{base}v_{c,d,pu}} \begin{bmatrix} \frac{1}{(3+2\sqrt{2})^{\frac{1}{2}}\tau_{eq}} \\ \frac{1}{(3+2\sqrt{2})^{\frac{3}{2}}\tau_{eq}^2} \end{bmatrix} \quad (2.61)$$

The fraction  $\frac{v_{DC,pu}}{v_{c,d,pu}}$  is assumed to be 1 during the tuning.

## 2.3 Cable

The model used for the DC-cable is chosen because of two features. Firstly, the model is able to capture the frequency dependency of the cable parameters. Secondly, the formulation of the model does facilitate state space representation which can be used for eigenvalue analysis. Since this is an often implemented technique used in stability analysis of models, this feature was desired of the cable model [60]. There are two challenges related to achieving these two features which can be made clear through inspection of a steady-state conventional cable model.

### 2.3.1 Steady-state conventional cable model

The steady-state pi-model of a cable can be seen in fig. 2.15 where the elements of the cable are described by eqs. (2.62) and (2.63).

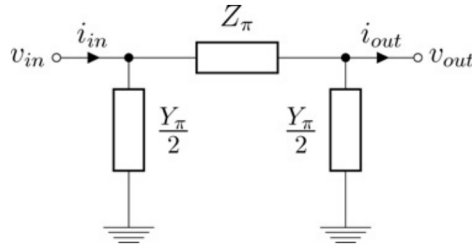


Figure 2.15: Steady-state pi-model of a cable [96]

$$Z_{\pi} = z(r(\omega), l(\omega)) \ell \frac{\sinh(\gamma \ell)}{\gamma \ell} \quad (2.62)$$

$$Y_{\pi} = y(g(\omega), c(\omega)) \ell \frac{\tanh(\gamma \ell / 2)}{\gamma \ell / 2} \quad (2.63)$$

where  $r$ ,  $l$ ,  $c$ , and  $g$  are the resistance, inductance, capacitance and conductance of the cable respectively and  $\ell$  is the length of the cable.  $z$  and  $y$  are the impedance and admittance per length of the cable and  $\gamma$  is the propagation constant defined according

to eq. (2.64).

$$\gamma = \sqrt{zy} \quad (2.64)$$

Equations (2.62) and (2.63) reveal two issues related to this model. Firstly, the hyperbolic correction factors that are used, do not allow for this model to be expressed in a state space form. This is circumvented by breaking the cable down into  $n$  smaller sections. The parameters in each section are thus a function of  $\ell/n$ . This is useful because the  $\sinh(x) \approx x$  and  $\tanh(x) \approx x$  for small values of  $x$  [97]. It is also quite natural given that the cable used in this model is assumed to be quite long since HVDC is used. The second issue stems from the fact that the impedance and admittance are functions of frequency dependent parameters. The frequency dependence of the conductance and capacitance of the admittance is often omitted [98], but as was shown in [96], assuming that the resistance and inductance are not frequency dependent is far more severe. It has been shown that the frequency dependency of the parameters can be captured by modeling each section of cable using several RL-branches [96], [99]. The parameters of the branches,  $R_j$  and  $L_j$   $j \in \{1, 2, 3\}$ , were determined using vector fitting against measurements of real cables [92], [100].

### 2.3.2 The cable model

The cable model uses five cascade connected pi-sections with three parallel branches, see fig. 2.16. The specific parameters of the cable model are listed in table B.6.

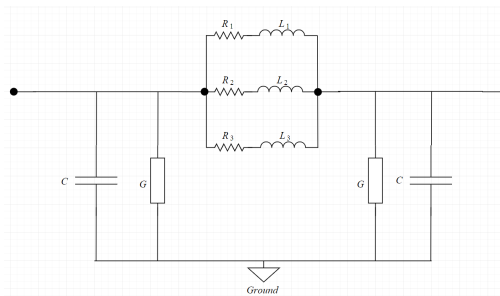


Figure 2.16: Pi-section used in the cable model

## 2.4 Turbine

A well-known feature that any wind power plant must cope with is significant variations in wind speed and stability. Furthermore, turbine control around the threshold value for the rated wind speed causes changes in the stored kinetic energy of the turbine. This causes the turbine to absorb and release energy, resulting in fluctuations in power delivered to the HVDC transmission system. Thus, to investigate if the MMC energy storage capabilities can dampen these fluctuations, a turbine model with the necessary control and energy characteristics was built. The wind turbine model created aims to capture essential dynamics related to converting wind speeds data into generated power. The parametric values, dynamic equations and control strategies used are from [101] and can be found in table B.7. The model was created by Joachim Espvik, and some elaborations of the model can be found in [68].

The central dynamic equation is the torque balance in eq. (2.65).

$$J \frac{d}{dt} \omega_{gen} = T_{inn} - T_{out} - T_{loss} \quad (2.65)$$

Where  $J$  is the moment of inertia of the generator,  $T_{inn}$ ,  $T_{out}$ , and  $T_{loss}$  are the torque of the rotor and generator as well as a term for the loss of torque due to friction.  $\omega_{gen}$  is the angular frequency of the generator.  $T_{inn}$  directly relates to the power entering the turbine from the wind, which can be described by eq. (2.66)

$$T_{inn} = \frac{1}{\omega_{gen}} P_{inn} = \frac{1}{\omega_{gen}} v^3 C_p \frac{1}{2} A \rho \quad (2.66)$$

Where  $v$  is the wind speed,  $\rho$  is the air density,  $A$  is the area swept by the rotor blades, and  $C_p$  is the power coefficient defining the proportional relationship between the power of the wind and the power that enters the turbine. This power coefficient relates to the aerodynamics of transforming the power of the wind into mechanical power needed to rotate the turbine blades.  $C_p$  can be expressed analytically in terms of the tip speed ratio,  $\lambda$ , the length of the blades,  $\ell$ , and pitch angle of the rotor blades,  $\beta$ , by eqs. (2.67) to (2.69).

$$\lambda = \frac{\omega_{gen} \ell}{v} \tag{2.67}$$

$$\lambda_{ai} = \frac{1}{\frac{1}{\lambda + 0.08\beta} - \frac{0.035}{\beta^3 + 1}} \tag{2.68}$$

$$Cp = 0.5176 \left( \frac{116}{\lambda_{ai}} - 0.4\beta - 5 \right) e^{\frac{-21}{\lambda_{ai}}} + 0.0068\lambda \tag{2.69}$$

The loss of torque related to friction is assumed to be proportional to  $\omega_{gen}$  with proportionality constant B. There are two controllers associated with the wind turbine which aim to control  $T_{inn}$ . One pitch angle controller to regulate  $T_{inn}$  by varying the pitch angle of the rotor blade,  $\beta$ . This allows for shedding of excess power when the wind speed is above rated value by tilting  $\beta$ . The second controller is a speed controller to regulate  $\omega_{gen}$ . This is done to achieve an optimal  $\lambda$  to maximize Cp and thus  $T_{inn}$  when the wind speed is below rated value. When the wind speed is above rated value, the speed controller maintains rated speed.

The overview of the model is depicted in fig. 2.17.

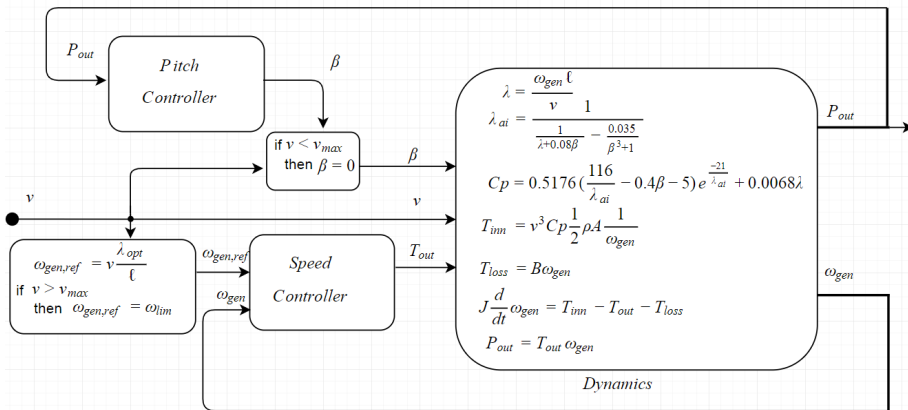


Figure 2.17: Overview of turbine model

### 2.4.1 Pitch angle control

The pitch angle control is activated if the wind speed is higher than a certain threshold value,  $v_{max}$  defined in terms of rated power. This threshold value is defined according to eq. (2.70)

$$v_{max} = \left( \frac{P_{rated}}{Cp_{max} \frac{1}{2} \rho A} \right)^{\frac{1}{3}} \quad (2.70)$$

When the wind speed exceeds its threshold value, the angle of the rotor blade is tilted to ensure that the mechanical input power does not exceed the design limits [102]. The reference for the pitch angle,  $\beta_{ref}$ , is found based on the difference between the generated power and the rated power. It is possible to determine  $\beta_{ref}$  based on wind speed, but because accurate wind speed measurements are impossible, this would not be appropriate [103]. The control is based on a PI-regulator, where the integral gain can be varied. This variation is dependent on the difference between  $\beta$  and the output of the controller before a limiter is used. This is because when the wind speed is close to rated, the sensitivity of aerodynamic torque to pitch angle is minimal, and thus a greater gain is needed [103]. The limiter is used because  $\beta$  cannot exceed certain values without inflicting damage to the system. Lastly, because it takes some time to adjust the pitch angle of the rotor blades mechanically, a delay is introduced to capture this dynamic. The pitch angle is thus controlled, according to fig. 2.18.

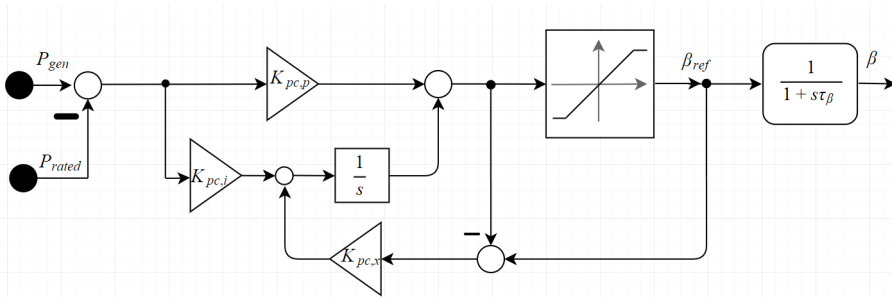


Figure 2.18: Overview of the pitch angle controller used in the wind turbine model

When the wind speed does not exceed  $v_{max}$ , the controller sets  $\beta = 0$ .

## 2.4.2 Torque controller

The torque controller is used to produce an optimal  $\lambda$  by controlling  $\omega_{gen}$ . The wind speed is used to determine the reference for the angular speed of the generator,  $\omega_{gen,ref}$ .

$$\omega_{gen,ref} = \lambda_{opt} v \frac{1}{\ell} \quad (2.71)$$

where  $\lambda_{opt}$  is the optimal tip-speed ratio. If the wind speed exceeds  $v_{max}$ , see eq. (2.70), then the reference is determined using  $v_{max}$  instead of  $v$ . Because of the sign convention associated with the generator, the error signal  $\omega_{ref} - \omega$ , is multiplied by  $-1$ . Furthermore, for the same reason as in the case with the speed controller, the integral gain is adjusted depending on the output torque. The torque controller is depicted in fig. 2.19.

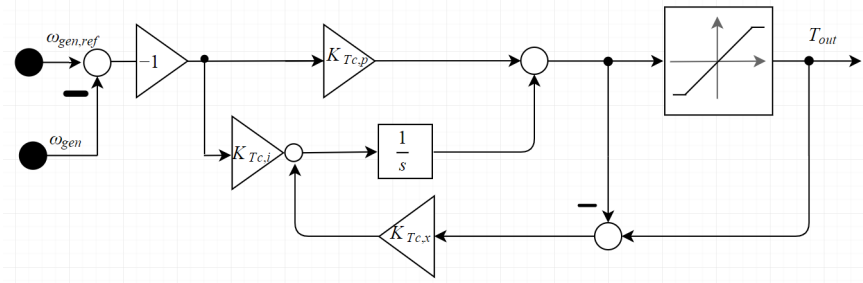


Figure 2.19: Torque controller



# Chapter 3

## OpenModelica: verification and integration with Opal RT

Before OpenModelica can be used to investigate the positive contribution of the MMC in an HVDC system, it must first be verified that the software can capture all dynamics of interest. To achieve this, a switching model of a 2L-VSC is built in OpenModelica and MATLAB Simulink for comparison. Because the MMC model is an average model, the dynamics characterizing the switching model of the 2L-VSC is of significantly higher frequency. Thus, if OpenModelica can capture all the dynamics of the 2L-VSC with similar precision as MATLAB, then it can be confidently assumed that it can capture all dynamics of interest in later simulations.

Moreover, because of the advantage of HIL-testing, model integration with real-time simulation tools is an essential feature of the software. Therefore, this chapter outlines how models in OpenModelica must be constructed to allow for such integration. In this thesis, the real-time simulation tools used are ePHASORsim and OP5700. The integration process is written as a guide to ease future application.

### 3.1 Modeling high-frequency dynamics: a Two-level VSC switching model

To assess OpenModelica's ability to capture and model relatively high-frequency dynamics, a switching model of a 2L-VSC was built. The mathematical description, control, and modeling details of the 2L-VSC are explained in [104], [105]. The topology of the model is depicted in fig. 3.1. This section highlights the necessary differences between the two models, the one developed in OpenModelica and the one in Simulink.

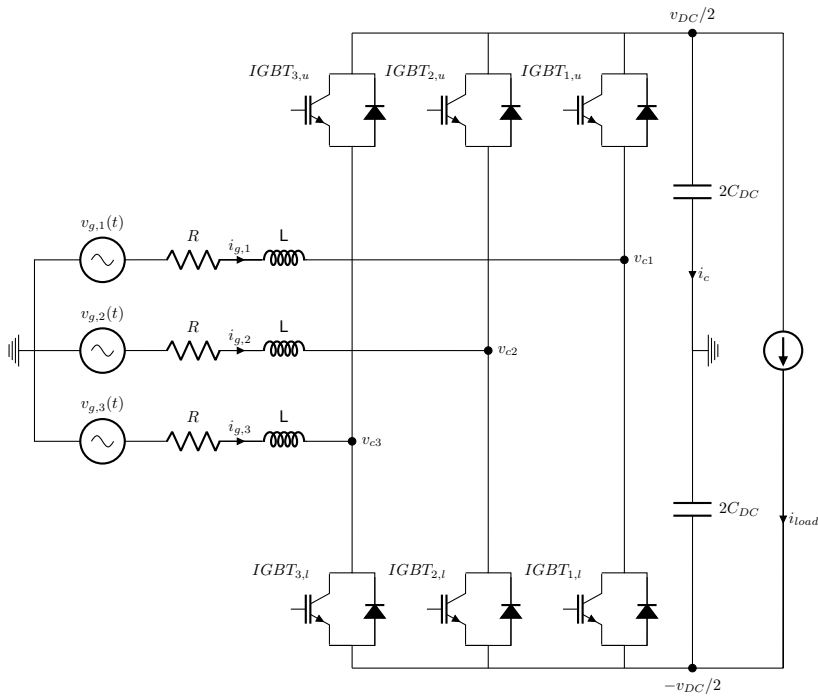


Figure 3.1: System modeled in OpenModelica and Matlab to validate OpenModelica's ability to model systems characterized by relatively high frequency dynamics

### 3.1.1 Modeling of the switches

Some of the key components of the two-level VSC are the switches, giving it access to two voltage levels:  $v_{DC}/2$  and  $-v_{DC}/2$ . As can be seen in fig. 3.1, each phase of the 2L-VSC has two IGBTs which can either conduct or not conduct current. If the upper IGBT conducts then  $v_{DC}/2$  is applied and if the lower IGBT conducts then  $-v_{DC}/2$  is applied at the AC terminals of the converter. To avoid a short circuit, these IGBTs can never conduct simultaneously and thus a single variable,  $\delta_k$ , can describe the state of both IGBTs in phase k. I.e.  $\delta_k = 1 \Leftrightarrow IGBT_{k,u}$  conducts and  $IGBT_{k,l}$  does not conduct and vice versa for  $\delta_k = 0$ . The switching state of each phase is determined by a PWM, as explained in section 3.1.2. The IGBT is modeled using an IdealCommutingSwitch from the standard Modelica library which is connected in parallel with an ideal diode from the same library, see fig. 3.2a. In the MATLAB model, the same set-up is modeled using an "IGBT/Diode"-block from the "Power Electronics" library, see fig. 3.2b.

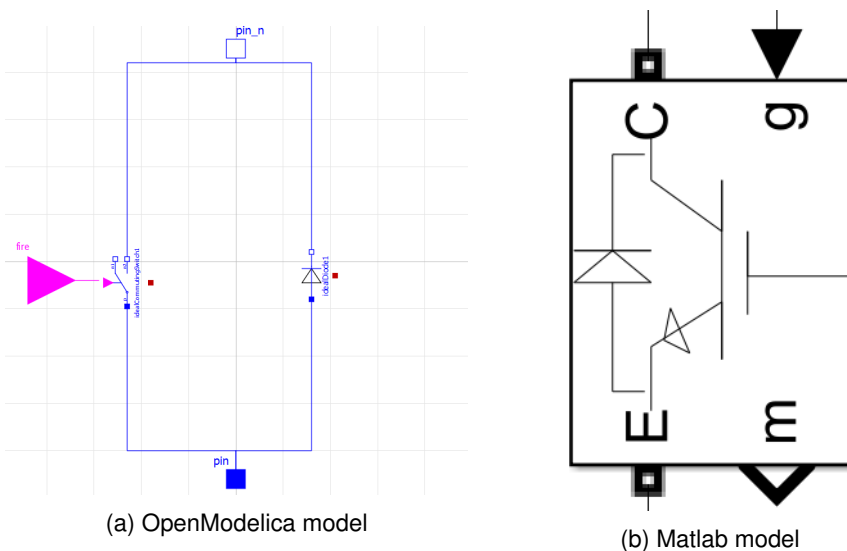


Figure 3.2: The models for the IGBT-diode pair

### 3.1.2 PWM

The PWM determines  $\delta_k$  by comparing a *carrier signal* against a *modulating signal*. In this case, the carrier signal is a sawtooth signal, and the modulating signal is the per unit converter voltage reference for phase k. When the reference signal is larger than the carrier signal,  $\delta_k$  is 1. In the OpenModelica model, two conjugate variables are produced,  $k_{fire}$  and  $k_{notfire}$  which are sent to the upper and lower IGBT in phase k respectively, see fig. 3.3. In the MATLAB model, these same firing signals are calculated using logic

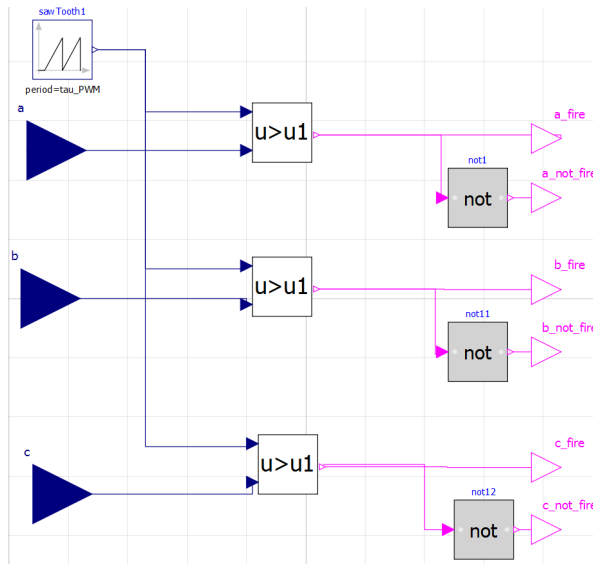


Figure 3.3: PWM used to produce switching states

equations in a self-defined function taking the voltage references as input together with a sawtooth signal, s, from the "Simulink/quick insert/sources" library.

### 3.1.3 The memory block

To avoid algebraic loops in the MATLAB model, each measured signal in the model was sent through a "memory"-block. This was not required by the OpenModelica model.

## 3.2 Integration of OpenModelica models with real-time simulation tools

As mentioned in the introduction, one attractive feature of OpenModelica is that models created in the OpenModelica environment can be run using real-time simulation tools, such as the ones provided by Opal-RT. This can allow, e.g., HIL testing. HIL testing is a technique used to test controllers without needing a physical plant to control. Instead, the behavior of the plant can be mimicked by the system model (often called HIL simulator). To realistically test the controllers, it is therefore important that the HIL simulator mimics the system behavior in real-time [67], [106]. HIL testing based on models developed in the Modelica language is already being done, especially in the Automobile industry, because of the ability to model different physical domains (e.g., mechanical, electrical, thermal, etc.) [60], [107]. Furthermore, not only is testing of complex HVDC networks under e.g., transient operation mandatory practice, but successful HIL testing with prototype controllers is *required* before real controllers can be installed in real grids [108].

This section addresses how to build models using OpenModelica, that are suitable for real-time simulation using Opal-RT's real-time simulation tools. For related issues such as download and installation of RT-LAB or connections of the simulation system and Host PC, the interested reader is referred to [109].

To clarify the role of the various components and software needed for the real-time simulation, an overview of the real-time simulation conducted in this thesis is initially presented. OpenModelica was used to build a model of an MMC, according to section 2.1, but by assuming a constant DC voltage and thus using eqs. (2.38) to (2.41) as system equations. Subsequently, the model was altered to allow for successful integration with a larger system model, henceforth referred to as a system. How this alteration must be done is described in section 3.2.1. The system was described in an Excel file, together with a so called FMUGlossary file. The development of these files is described in section 3.2.2.

### Chapter 3. OpenModelica: verification and integration with Opal RT

To run real-time simulations, suitable software and hardware for real-time simulation are necessary. This thesis used ePHASORsim and OP5700 provided by Opal-RT for these purposes respectively [110], [111]. To ensure proper division of computational labour and provision of a graphical user interface (GUI), Simulink was used as a simulation environment. In Simulink, two subsystems were created, one containing an ePHASORsim solver that communicated with OP5700, and one containing scopes that communicated with the Host PC. How to use Simulink for this integration process is described in section 3.2.3.

An overview of the real-time simulation structure is depicted in fig. 3.4.

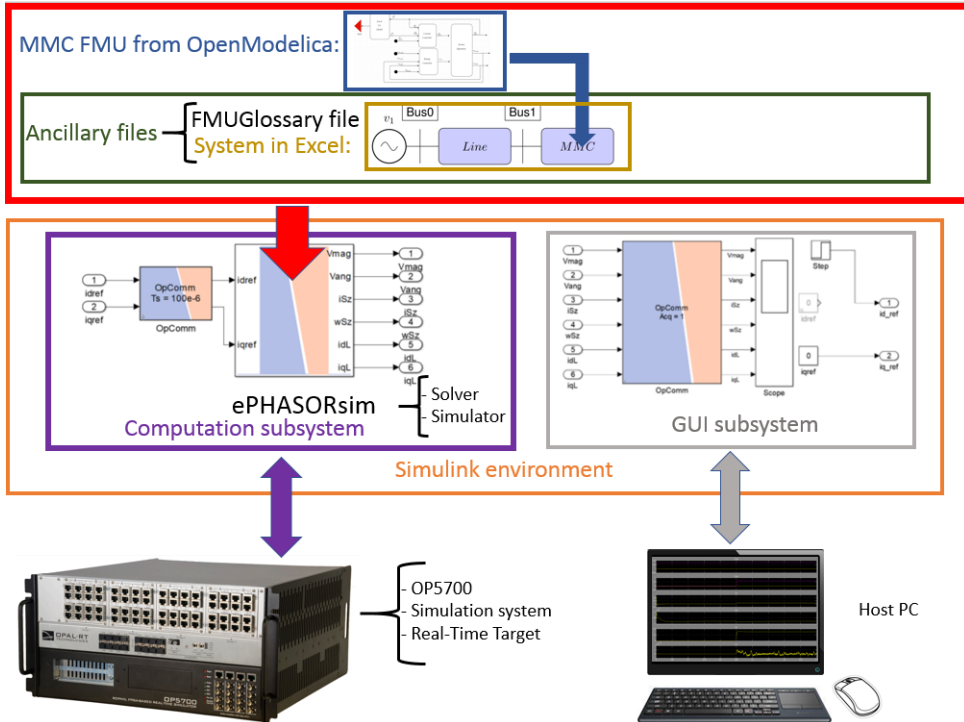


Figure 3.4: Overview of real-time simulation structure. Unidirectional arrows mean that one element of the structure is "contained" in another, while bidirectional arrows indicate that data are exchanged between two elements

The process of integrating OpenModelica models into systems simulated by real-time simulation tools can be broken down into 3 main steps: the development or adaption of the OpenModelica model, the creation of the ancillary files needed, and the integration

---

## 3.2 Integration of OpenModelica models with real-time simulation tools

process. These steps are outlined in this section as a guide for future application.

To demonstrate this integration, two models were developed in OpenModelica, and two systems were simulated using ePHASORSim. These systems contained the models developed in OpenModelica. Overviews of these systems are depicted in figs. 3.5 and 3.6. The system in fig. 3.5 was simulated in real-time using OP5700 as a real-time simulation system.

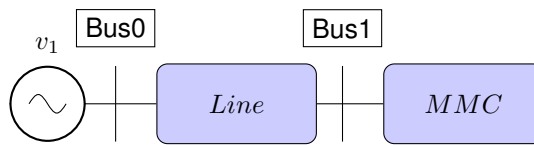


Figure 3.5: Illustration of a system simulated with ePHASORSim, containing an MMC model developed in OpenModelica.

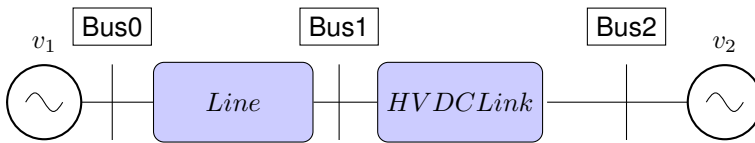


Figure 3.6: Illustration of a system simulated with ePHASORSim, containing a HVDC-link developed in OpenModelica.

### 3.2.1 The creation/adaptation of the OpenModelica model

To run a simulation with ePHASORSim which incorporates an OpenModelica model, the model must be designed so that it can be integrated with the interface used by ePHASORSim. To do this, a so-called Functional Mock-up Interface (FMI) protocol is used. The FMI protocol requires, among other things, that the model must be transformed into a Functional Mock-up Unit (FMU). Moreover, certain boundary conditions are required for ePHASORSim to integrate the OpenModelica model with the rest of the system.

### The required boundary conditions of the OpenModelica model

To integrate a model with a larger system, ePHASORSim needs to interpret the model as a component which can be modeled as a current injector. ePHASORSim recognizes current injectors by a specific component, the Power Pin. The necessity for the Power Pin is the basis for the required interface of the OpenModelica model, which is to be integrated with the rest of the system using ePHASORSim.

The Power Pin is a connector that includes variables for voltages and currents. These variables are the dq-components of the currents and voltages and must be of type real. The Power Pins are used to interface with power system buses in ePHASORSim simulations. Therefore, the variables that are interfaced must be transformed to a global reference frame. This is because the simulation might include several OpenModelica models connected at various buses in the system. Consider for instance fig. 3.6. Globally,  $v_1$  might be defined to be aligned with a global Real-axis, causing the voltage at "Bus2" to not be globally aligned with the global Real axis. However, the OpenModelica component "HVDCLink" is designed under the assumption that the local grid voltage vector is aligned with its local d-axis. Therefore, a transformation between the reference frames is necessary [112].

The mathematical basis for this transformation is depicted in fig. 3.7. The real and

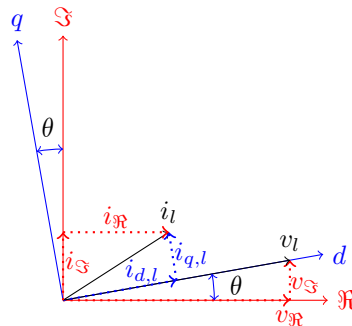


Figure 3.7: Illustration of reference frame-transformation

imaginary axis define the global reference frame. Locally, a dq-reference frame might be

---

### 3.2 Integration of OpenModelica models with real-time simulation tools

---

used, which is aligned with the local grid voltage vector. The transformation between these reference frames is mathematically described in eqs. (3.1) to (3.2).

$$\theta = \arctan2(V_{\Im}, V_{\Re}) \quad (3.1)$$

$$\begin{bmatrix} v_{d,l} & i_{d,l} \\ v_{q,l} & i_{q,l} \end{bmatrix} = \begin{bmatrix} \cos(\theta) & \sin(\theta) \\ \sin(\theta) & -\cos(\theta) \end{bmatrix} \begin{bmatrix} v_{\Re} & i_{\Re} \\ v_{\Im} & i_{\Im} \end{bmatrix} \quad (3.2)$$

Hence, the requirement of the Power Pin introduces three interface requirements.

1. Assuming the OpenModelica model is built in a 123-reference frame, the local dq-voltage variables from the Power Pin must be transformed into a 123-reference frame. These signals can then be used as the control signals for controllable voltage sources defining the grid. If the OpenModelica model is built in the dq-reference frame, this is not necessary.
2. A new block must be created which transforms the current and voltage variables from a local dq-reference frame to a global  $\Re\Im$ -reference frame. This is to interface between the Power Pins of the OpenModelica model and the system. The local variables are defined in terms of the global variable by eqs. (3.1) to (3.2).
3. The local currents and voltages cannot be flow or potential variables. Thus, if the model uses electrical components, the currents must be measured and sent to the Power Pin. The voltages from the Power Pin must be sent to controllable voltage sources and cannot be directly connected to electrical components.

The two transformation processes were encapsulated in the block "PowerPin to 3 phase grid". The two OpenModelica models created to be simulated using ePHASORSim are shown in figs. 3.8 and 3.9.

Note that because the model in fig. 3.8 is designed in the dq-reference frame, the only transformation needed is between the global and local currents and voltages. However, the model in fig. 3.9 is built in a 123-reference frame using electrical components. Therefore, all of the three aforementioned boundary conditions must be taken into account.

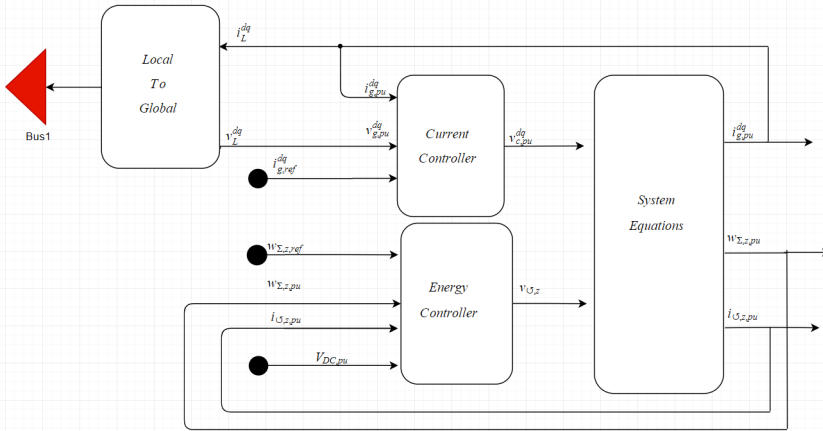


Figure 3.8: MMC\_base: the OpenModelica model interfaced with the system from fig. 3.5. The controllers and system equations are described in sections 2.1 and 2.2 and it is integrated with the rest of the system using a local to global transformation using eqs. (3.1) to (3.2) and a Power Pin.

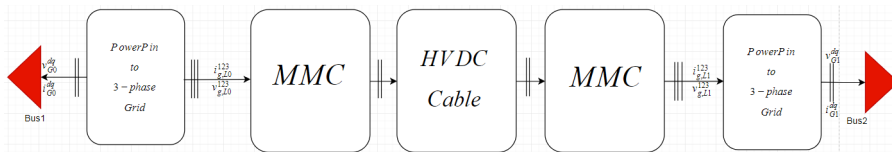


Figure 3.9: HVDC\_Base: The three phase OpenModelica model of an HVDC-link designed to be used with ePHASORSim in fig. 3.6. The MMC models are depicted in fig. 2.6 and the cable is described in section 2.3

### The transformation into an FMU

An FMU is simply a file that contains a simulation model, and that follows the FMI standard. Because of the widespread usage of the FMI standard, this allows the model to be integrated with a variety of tools. For an extensive list, the reader is referred to [113].

The process of creating an FMU is done using the "FMU creator" which can be found in the following directory C:\OPAL-RT\RT-LAB\v11.3.6.125\FMUcreator\FMUcreator. To smoothly build on the structure already created by RT-lab, the following construction

---

## 3.2 Integration of OpenModelica models with real-time simulation tools

---

procedure is recommended.

1. Create the model of the controller and system in accordance with limitation 1 - 3 from 3.2.1 and save it in the OpenModelica package `Opal-RT_Dev` which can be provided by Opal upon request. Make sure that after the local to global transformation block, there is a Power Pin with the dq-currents and voltages of the grid. Moreover, if the component is e.g., an MMC, the name of the model must be "`MMC_BASE`." That is, the name of the model must end with "`_BASE`."
2. Create a new model in the OpenModelica package "`GenUnit`," also provided by Opal upon request, and drag the model from `Opal-RT_Dev` into that environment. This `GenUnit` model must then have Power Pins with names "`Bus0`", "`Bus1`" etc. which are connected to the Power Pins of the "`_BASE`"-model saved under `Opal-RT_Dev`.
3. Open the FMU Creator from `C:\OPAL-RT\RT-LAB\v11.3.6.125\FMUCreator\FMUCreator`.
4. Under "`path`" chose the `GenUnit` and then under "`Model selection`" chose the model created in step 2. Then add the entire `OpalRT_Dev` library as a dependency. If the correct target (i.e., the simulation system) appears automatically then select that target. If it does not happen, then restart RT-Lab and try again. If no targets appear, then the target IP-address can be selected manually. Lastly, press "`Build model`."

### 3.2.2 The ancillary files

In addition to the requirement of the OpenModelica model to be transformed into an FMU, the FMI protocol also requires two more ancillary files. The first is an FMU-Glossary file used to recognize the parameters of the model, and the second is an Excel file that describes the system into which the OpenModelica model shall be integrated. More information on these files can be found under *Help* → *Helpcontents* → *ePHASORsimUserGuide* → *UserDefinedModels* → *UsingFMUs* in RT-LAB.

### The FMUGlossary file

The FMUGlossary file is used during the initialization of the model in question. Thus, it must include the name and type of the OpenModelica model as well as the number of parameters and their names. These are the parameters that are defined in the OpenModelica model "`*_BASE.`" Additionally, a unique ID for the model is needed. This ID is most easily generated by pasting the following line into Matlab: `UUID = java.util.UUID.randomUUID [114]`. This creates a variable, `UUID`, with the associated ID which can be copied and pasted into the ID-field in the FMUGlossary file. The easiest way to create a working FMUGlossary file for a specific model is to use the file already created for all the other generator units and then add one line specific for the model in question. This FMUGlossary file can be found in the following directory: `C:\OPAL-RT\RT-LAB\v11.3.6.125\FMUCreator\resources\FMUGlossary`. This file is stored as an Excel file and can be altered and modified as an Excel file, but must be saved as a `*.csv` file when used by `ePHASORsim`.

	A	B	C	D	E	F	
1	Version		1				
2	ID must be unique, containing numbers and characters						
3	Type 1 for machine, type 2 for exciter, type 3 for stabilizer, type 4 for turbine, type 5 for over-exciter, type 6 for under-excitation limiter, type 7 for hvdc						
4	Name of parameters must match with their corresponding names in FMUs.						
5	The order of components is not important, the order of parameters is important since other mapping files follow the same order						
6	Lines not starting with a GUID will be ignored in cimphony the mapping						
7	Entries right of the number of parameters declared in column 4 will be ignored and can be used for comments						
8							
9	ID	Name	Type	Number of Parameters	Parameters...		
76	efc8180d-9c1c-46d6-bf52-7bd2a51da90b	HVDC		7	11 Sb	Vb	La

Figure 3.10: FMUGlossary file. Lines 10 - 75 are hidden since they only shown the example components. The remaining 8 parameters are described in columns H-O

### The Excel file

To simulate a complete system, `ePHASORsim` needs an Excel file describing that system. Once again, the easiest way to create this Excel file is to download an example file and modify it for the specific purpose. An example file can be found under this directory: `C:\OPAL-RT\RT-LAB\v11.3.6.125\Examples\ePHASORsim\phasor11_HVDC\simulink`. In the case of the model depicted in fig. 3.6, 6 variables are defined as

### 3.2 Integration of OpenModelica models with real-time simulation tools

output from the HVDC model. In the GenUnit, these are defined as outputs and retrieved through the Excel file by describing the correct path of the variable e.g.,  $hvDC1/V_{DC,pu}$  extracts the variable  $V_{DC,pu}$  from the instance of an HVDC model called  $hvDC1$ . Additionally, the angle and magnitude of the two voltage sources are defined as output variables. Lastly, one parameter is defined as input: the reference of the active power delivered to  $v_2$ .

	A	B	C	D
1	outgoing	Vmag	1/Vmag	2/Vmag
2	outgoing	Vang	1/Vang	2/Vang
3	incoming	Pref	hvdc1/Pref	
4	outgoing	iSzMMC1	hvdc1/iSzMMC1	
5	outgoing	vdcMMC1	hvdc1/vdcMMC1	
6	outgoing	wSzMMC1	hvdc1/wSzMMC1	
7	outgoing	iSzMMC2	hvdc1/iSzMMC2	
8	outgoing	vdcMMC2	hvdc1/vdcMMC2	
9	outgoing	wSzMMC2	hvdc1/wSzMMC2	
10				
11				
12				

Figure 3.11: The Pins section of the necessary Excel file.

In the MMC model, four variables describing the internal dynamics of the MMC are defined as output variables, while the DC voltages are only described in the HVDClink model. Moreover, the inputs of the MMC model were the references for the d- and q-component of the AC-side currents, not the active power reference as it was in the HVDClink model. Moreover, the parameters of the models must be determined in the Excel file. This is done in the sheet with the name of the parameter, e.g., HVDC. The name of the sheet must match the name given to the component in the glossary file and the name of the GenUnit. Moreover, all the parameters listed in the Glossary file must be given a value in that Excel sheet. The parameters that were used in MMC\_BASE and HVDC\_BASE are listed in table B.4 and section B.5 respectively.

### 3.2.3 The integration process

Assuming the three necessary files (an FMU of the model, an Excel file describing the system, and an FMUGlossary file related to the OpenModelica component model) are all in place, ePHASORSim can now run real-time simulations. The environment this is done in is MATLAB Simulink. This integration is most easily understood by considering two required aspects of the integration environment: subsystems and the OpComm-block.

#### Subsystems in the Simulink environment

For RT-Lab to understand how to handle the system which is to be modeled properly, the system must be constructed using subsystems, that must follow a specific naming convention. On the top-level of the Simulink model, there can thus only be subsystems that follow this convention. The subsystems can be broken down into two categories: GUI subsystems whose names must begin with "SC\_" and computation subsystems whose names must begin with "SM\_" or "SS\_." There can only be one GUI subsystem.

Moreover, there can be as many computational subsystems as there are cores available in the simulation system. There must always be precisely one computational subsystem with a name beginning with "SM\_" (master subsystem). If other computations can be run in parallel, then their calculations can be grouped in other subsystems with names starting with "SS\_" (slave subsystem).

The reason for this division is that RT-Lab assigns different tasks to different subsystems. This also allows a user to influence how their computational power should be used. This is because each core of the simulation system is assigned the necessary calculations of only one computational subsystem, see fig. 3.12. Because internal signal (real-time-synchronized signal) sharing between CPU cores and between CPUs are faster than external signals (asynchronous signals) between the target and the Host PC, this allows for faster computation [115].

### 3.2 Integration of OpenModelica models with real-time simulation tools

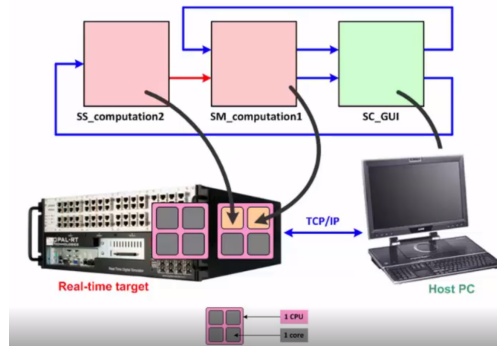


Figure 3.12: How RT-lab assigns tasks based on subsystem division [115]

#### Proper use of OpComm blocks

Any input in a subsystem must go through an OpComm block before the signal can be further processed. An OpComm block can be used to receive real-time-synchronized signals from other real-time subsystems or to receive asynchronous signals from the GUI subsystem. However, a single OpComm block cannot do both. This means that if a system contains a subsystem block that receives signals both from another computational subsystem and from the GUI subsystem, then that subsystem block must contain two OpComm blocks, one for each signal type, see fig. 3.13.

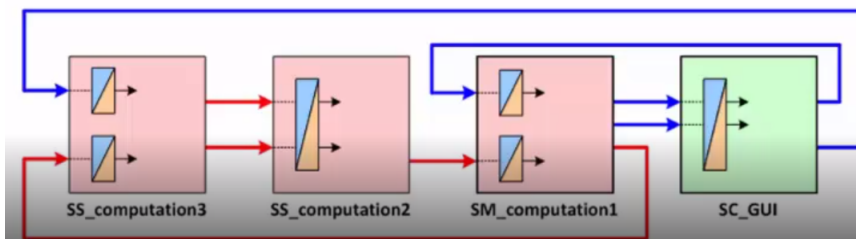


Figure 3.13: Overview of OpComm blocks in various subsystems [115]

### 3.2.4 The model construction in the Simulink environment

To simulate the system from fig. 3.5, two subsystems called SM\_Grid and SC\_console both with their respective OpComms were created in the Simulink environment. The computation subsystem needs to include the ePHASORSim solver, which, in turn, needs the MMC FMU and system Excel file. The GUI subsystem only needs the scopes for the states as well as the inputs of the MMC system, i.e., the references for the d- and q-component of the AC-side currents.

This is done by opening the Simulink Library Browser window and selecting RT-LAB/Phasor and dragging the "Solver" into the Simulink model window. By clicking on it and selecting the Excel-file, the solver alters to include the inputs and outputs described under "pins" in that Excel file. Additionally, the directory currently in use must include a folder that contains the FMU of the OpenModelica model. The name of this folder must be written under the library → "FMU component folder." The overview of the Simulink model is depicted in fig. 3.14.

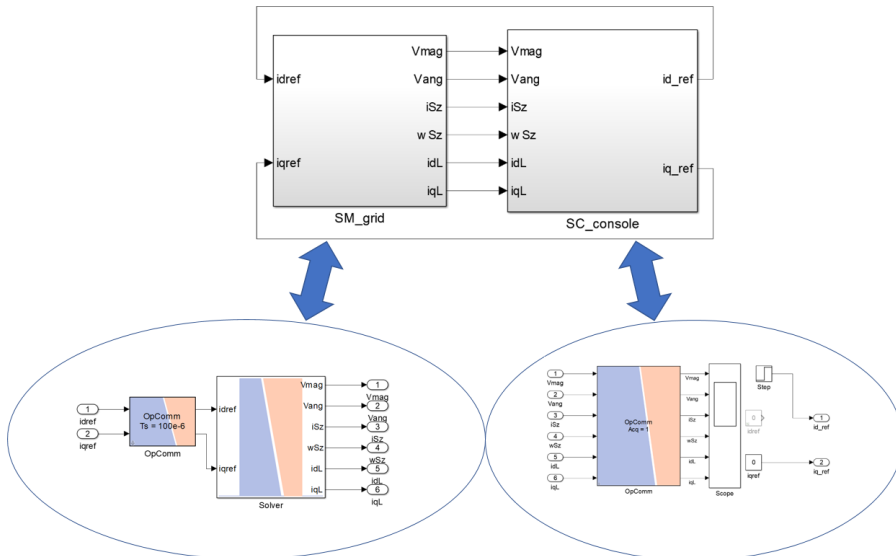


Figure 3.14: Simulink environment used in the simulation of the system from fig. 3.5 with the integrated MMC FMU model from fig. 3.8

# Chapter 4

## Simulation and results

This chapter describes the simulations that were carried out and explains the results of the simulations. The results are only explained in this chapter, while the data are further discussed in chapter 5. The first set of simulations is run to make sure that OpenModelica is capable of modeling relatively high-frequency dynamics. This is done by comparing models resembling fig. 3.1 made in OpenModelica with similar models made in MATLAB Simulink. The second set of simulations aims to demonstrate that the Modelica based MMC FMU was successfully integrated into a system which was simulated using real-time simulation tools. The third set of simulations is run to investigate how MMC energy should be used to improve the power dynamics of HVDC transmission systems. This is done in two parts. The first part investigates if the MMC can be used to dampen the power variations of the turbine caused by fluctuations in wind speed. The second part investigates if the MMC energy can be used to reduce power step response time. Lastly, analysis of the decoupling effects of a feed-forward term in the voltage controller of an MMC is performed.

## 4.1 Simulation of switching model of two-level VSC

To investigate OpenModelica's ability to capture relatively high-frequency dynamics, a switching model of a 2L-VSC described in section 3.1 was developed in OpenModelica and MATLAB. The parameters used for the simulation are listed in section B.3. To ensure that the behavior of the switches can be adequately captured, each simulation was run using a time-step of  $1 \mu\text{s}$ . At the instance of  $t = 0.4$ , a step in DC voltage is applied in the DC voltage controller. Since the peak value of the AC voltage is defined to be half that of the base of the DC voltage and the grid was defined to be stiff and equal to 1 p.u., the reference of the DC voltage was initially set to be 1.2 p.u. to avoid over-modulation.

The solver used first in the OpenModelica version of the model was Dassl while the solver used by MATLAB was ode45 (Dormand-prince). They both operate using variable step lengths. This provides a reasonable basis for comparison between the software. Other solvers were subsequently used to analyze if this introduces errors or differences in run-time.

After every solver was tested, one of the core differences of the two models, the memory block, was removed and replaced with a continuous delay. This was done under the suspicion that the discrete nature of the memory block introduced a source of error in the dynamics produced by MATLAB Simulink.

### 4.1.1 Three Phase current

An essential feature of the 2L-VSC is its ability to produce AC currents resembling sinusoidal waveforms. The AC-terminal currents of the two models are presented in fig. 4.1.

As described in section 3.1 the voltage applied at the AC-terminals of the converter alternates between  $v_{DC}/2$  and  $-v_{DC}/2$ . When the low voltage is applied, the voltage

## 4.1 Simulation of switching model of two-level VSC

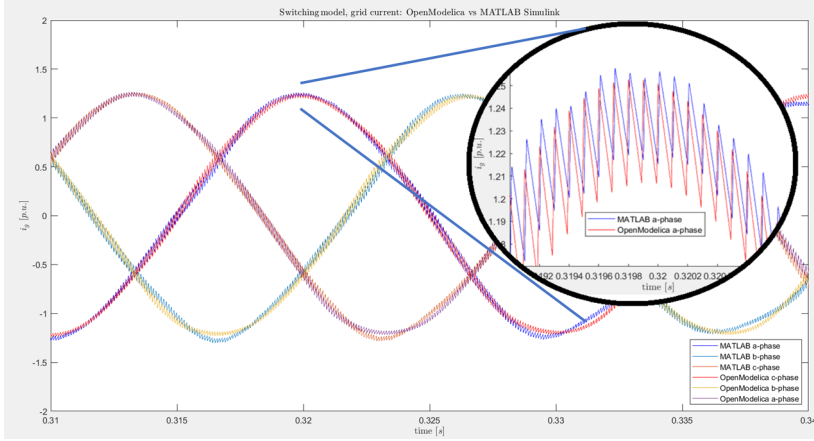


Figure 4.1: Three-phase grid currents produced by MATLAB Simulink and OpenModelica

across the inductor is descending in the direction of positive current resulting in an increase in current in accordance with eq. (4.1).

$$\frac{d}{dt} i_{g,k} = \frac{1}{L} \left( v_{g,k} - \left( -\frac{v_{DC}}{2} \right) \right) \quad (4.1)$$

Since the frequency of the PWM is 200 times higher than the frequency of the grid voltage, the voltage across the inductor is close to constant during one switching period. This causes the current to rise and fall linearly during application of  $-v_{DC}/2$  and  $v_{DC}/2$  respectively. This sequentially linear current behavior can be clearly seen in the two models in the zoomed part of fig. 4.1.

Moreover, it is expected that the ripple of the current is at its minimum when the current is close to its peak and trough. This is because the voltage difference between the grid voltage and the converter voltage is smallest, resulting in smaller rates of change of current according to eq. (4.1). The depiction of the three-phase grid currents in fig. 4.1 shows that the OpenModelica model captures this aspect of the system behavior.

The differences in the dynamics produced by the two software are presumed attributable to the differences in modeling of the switches, as discussed in chapter 5.

### 4.1.2 DC voltage step response

A step in the DC voltage reference was introduced at  $t = 0.4\text{s}$  equal to 0.1 p.u. The DC voltage profiles are depicted in fig. 4.2. The voltage profile of the switching model made in OpenModelica is compared against the DC-step response of an average model of the 2L-VSC as well as the MATLAB results.

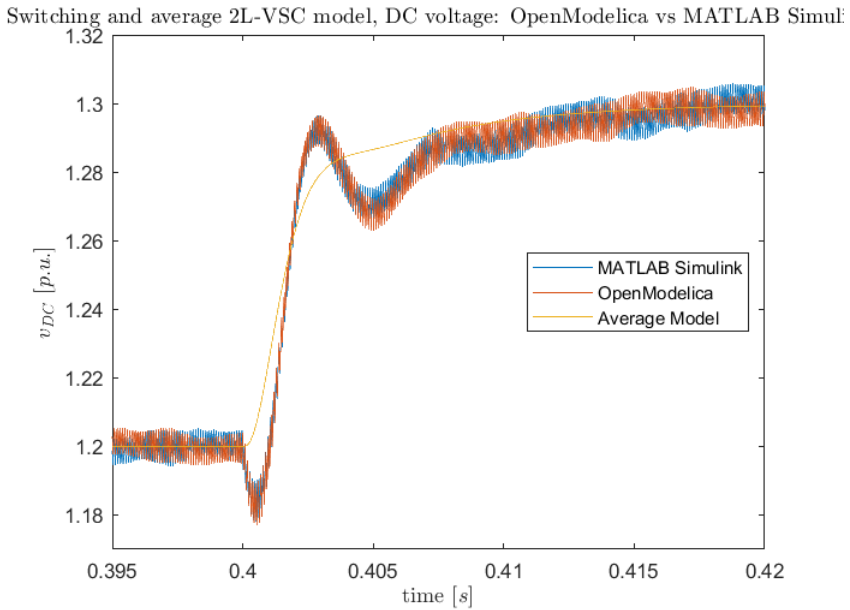


Figure 4.2: DC voltage produced by MATLAB simulink and OpenMModelica

As can be seen in fig. 4.2, the switching model captures some high-frequency dynamics that an average model does not capture. Furthermore, these dynamics resemble the dynamics produced by the MATLAB model very closely.

As to why the average model cannot capture all the dynamics captured by the switching models, this relates to several simplifications made in the average model. Immediately succeeding the step in reference, the switching model falls slightly, while the average model instantly rises. This can be explained by considering the behavior of the two different AC-side models. In the average model, the AC-side is modeled using voltage sources

---

## 4.1 Simulation of switching model of two-level VSC

---

that can follow a reference exactly. Thus, when the DC voltage reference increases, the AC-side voltage sources can instantly produce a lower voltage increasing the current flowing through the inductor as per eq. (4.1) which again elevates the DC voltage. In the case of the switching model, the lower AC voltage is created by applying  $-v_{DC}/2$  for longer fractions of the switching period. This does increase the current flowing through the inductor, but in the time it takes to build up that current, the capacitor discharges slightly, causing a small dip in voltage.

The differences in the two models can also explain the more significant oscillations found in the switching models. As already mentioned, the way the switching models operate introduces some delays relating not only to the PWM but also to how quickly the currents and voltages in the system can change, as well as how independently they can vary. Initially, the only delay purposefully added in the average model is a delay between the current controller and the AC-side voltage sources which is introduced to account for the delay of the PWM. If this delay is increased from  $1.5\tau_{PWM}$  to  $4\tau_{PWM}$ , some of the same oscillations would also appear in the average model, suggesting that such delays cause the oscillations. However, since these delays relate to the dynamics between the electrical components and the switches of the 2L-VSC, they are inaccurately modeled when assumed constant. i.e., if such a delay is introduced, the same oscillatory behavior emerges during the first period of the oscillation, but it would also persist longer. For instance, the dynamic of the capacitor needing to discharge during the period of current reduction can only be modeled as a delay when the current needs to rise.

### 4.1.3 Run-times

MATLAB was unable to simulate the dynamics of the 2L-VSC correctly when using a memory block and a fixed time-step solver. Therefore, the memory block was replaced with a continuous delay to investigate the potential impact of this. The transfer function used to emulate this delay is shown in eq. (4.2).

$$G = \frac{1}{s * 10^{-6} + 1} \quad (4.2)$$

## Chapter 4. Simulation and results

This was also introduced into the OpenModelica model to test if it could improve performance. It might seem counterintuitive that introducing a delay would improve performance. However, the hypothesis was that the algebraic loop also existed in the OpenModelica model, but that OpenModelica had build-in techniques to handle it. Thus, it was conceivable that if the algebraic loop were broken by using the delay in eq. (4.2), no such mitigating effort from OpenModelica would be needed, which might reduce the run-time. The run-times of the simulations are displayed in table 4.1.

Table 4.1: Table listing run-times [s] of 2L-VSC switching models when modeling 0.5s. Simulations labeled x means the dynamics produced are wrong. na. means not available. WMB means with memory block, WCD means with continuous delay

			MATLAB		OpenModelica	
			WMB	WCD	No Delay	WCD
Fixed time-step	Explicit	Ode8 Dormand-Prince	x	52.1	na	
		Ode5 Dormand-Prince	x	29.2	na	
		Ode4 Runge-Kutta	x	23.3	483	486
		Ode3 Bogacki-Shampine	x	19.5	na	
		Ode2 Heun	x	16.1	230	225
		Ode1 Euler	x	12.6	121.7	116
	Implicit	Ode14	x	153.4	na	
		Ode1	na			
	Variable time-step	Explicit	Ode45	29.5	33.6	
Ode23			23.5	28.9		
Ode113			20.4	43.9		
Implicit		Ode1-5 Dassl	na		1317	2544
		Ode15s	x	48.1		
		Ode23s	x	64.9		
		Ode23t	x	29.7		
		Ode23tb	x	30.2		

As table 4.1 shows, breaking the algebraic loop by introducing the delay did not reduce the run-time of the software. On the contrary, when the variable step-time solver Dassl was used, the run-time increased. Moreover, the run-times increase with the order of the

solver. This is because higher order solvers account for higher order derivatives. With this added precision comes increased computational labor; hence, the increased run-time.

Based on these findings, it can be confidently said that more detailed models, e.g., switching models of systems such as the 2L-VSC can provide valuable insight into the dynamics characterizing such systems. These insights are necessary to further develop average models to capture dynamical features of interest. Furthermore, OpenModelica can accurately model systems characterized by such relatively high-frequency dynamics with similar precision as MATLAB. However, when modeled in the way described here, the simulation times were typically at least one order of magnitude higher when OpenModelica was used for the simulations.

## 4.2 Real-time simulation using Opal-RT

To demonstrate that models created in OpenModelica can be integrated into a system which is simulated using ePHASORSim and OP5700 (see fig. 4.3), the two systems described in section 3.2 were simulated. The parameters of the models can be found in tables B.4 and B.5. For the simulation of the system containing the HVDC-link, the time-step of the simulation was  $25\mu\text{s}$  while the time-step for the model containing the MMC was  $100\mu\text{s}$ . The tests were performed at the National Smart Grid laboratory in Trondheim.



Figure 4.3: Real-time simulation system/Real-time target used for the simulations

## Chapter 4. Simulation and results

---

The results from the real-time simulation of the MMC are depicted in fig. 4.4. At  $t = 0.25$ , a step in the reference of local d-component of the grid current from 0 to 0.3 p.u. was applied. Thus, the local d-component of the grid-current approached that value. Since the current controller includes a decoupling of the d- and q-component of the AC-side grid current, the q-component of the current, effectively remains at zero.

As a consequence of this, as small drop in  $w_{\Sigma,z}$  can be seen, which is in accordance with eq. (2.41). This also causes a slight decrease in  $v_{\odot}$  causing an increase in  $i_{\odot}$  in accordance with eq. (2.40).

Since the voltage and angle at Bus0 are defined to be 1 p.u. and 0 respectively, they do not change upon this step. However, since the power flows towards Bus0, this causes the angle at Bus 1 to increase. The magnitude also increases, but to a much lesser degree.

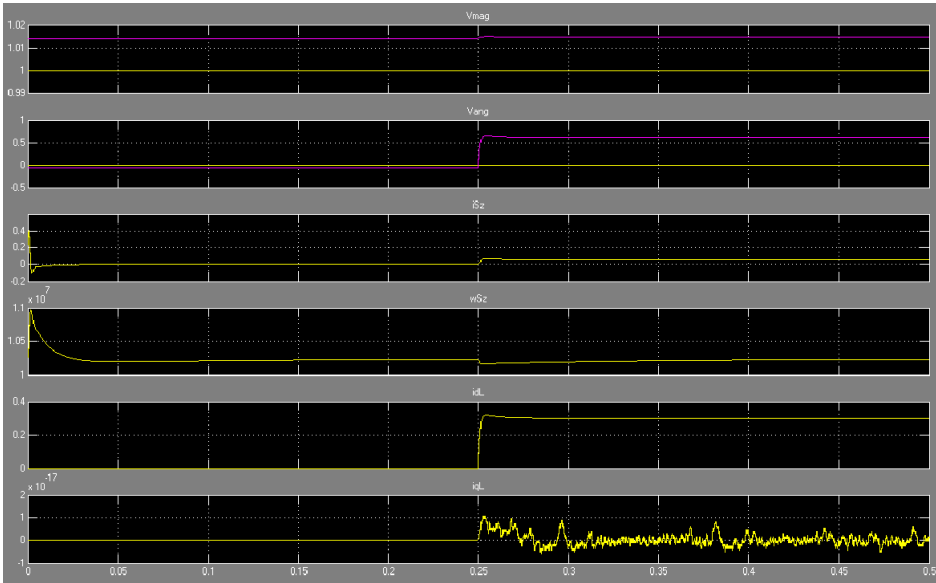


Figure 4.4: Response of the 6 output variables of the system modeled containing the 4 MMC variables

Based on these results, it can be said that the system behaved as expected and the integration of the MMC into the system was successful.

## 4.3 Dampening power fluctuations from the wind turbine

To investigate the ability of the MMC to improve power dynamics on the time-scales of seconds, the zero-sequence energy sum is controlled to dampen power fluctuations from the turbine caused by wind variation. To model this, the model in fig. 4.5 was developed.

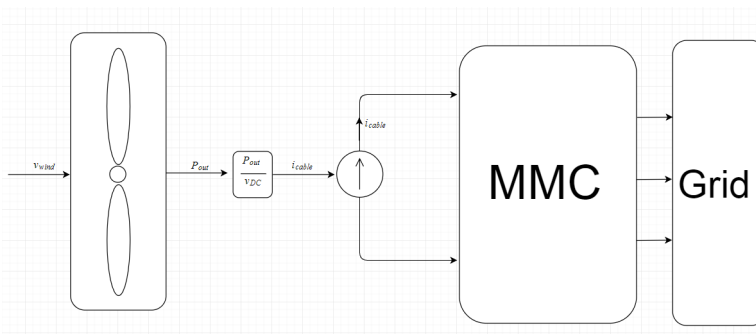


Figure 4.5: Model used when testing if the MMC can improve the power response of an energy system during wind fluctuations

The scenario tested, in this case, is chosen to study dynamics between the turbine, its control, and the energy storage capability of the MMC. For clarity, it is not suggested that fig. 4.5 realistically depicts the power electronic interface between a wind turbine and the HVDC system. It only serves as a model, to investigate if the MMC can dampen the power variations of the turbine.

To introduce such variations, the wind speed is chosen to vary around the threshold wind speed value used in the turbine controllers. The simulation is run under two conditions. First, it is run with no alteration to reference of the zero-sequence energy sum,  $\Delta w_{\Sigma,z,ref} = 0$ . During the second simulation, the same reference is determined by a controller which is depicted in fig. 2.11.

The wind profile selected in this scenario is based on wind data provided by [101] with regards to fluctuation. These data are from the Roosevelts roads weather station, which

## Chapter 4. Simulation and results

---

was chosen for its high resolution of 1 minute. In the data provided, the quickest alteration in wind speed was  $0.14 \text{ ms}^{-2}$  on average over a period of 1 minute. Assuming there is some fluctuation within that time-frame, the maximum wind speed fluctuation in this scenario is set to be  $0.2 \text{ ms}^{-2}$

The power delivered to the grid in the two cases are displayed in fig. 4.6 together with the rotational speed of the turbine and the wind speed. All values provided are in p.u.

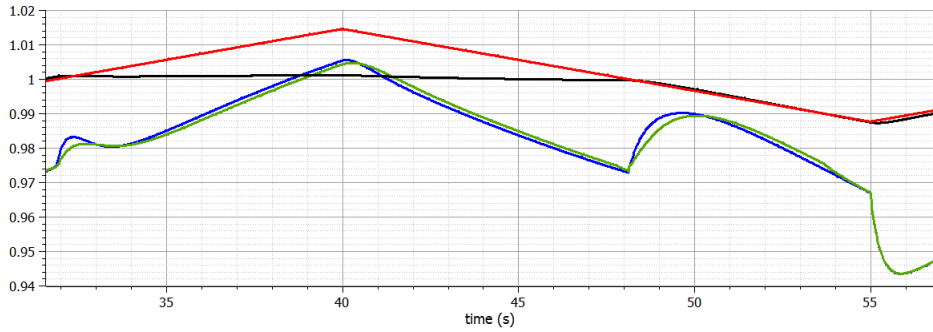


Figure 4.6: Power profiles during fluctuation in wind speed and rotational speed of generator. The blue power profile represents the case with  $\Delta w_{\Sigma,z,ref} = 0$  and the green profile represents the case using the controller from fig. 2.11. The black line is  $w_{gen,pu}$  and the red line is  $v_{wind,pu}$

The zero-sequence energy sum of the converter is depicted in fig. 4.7 in p.u.

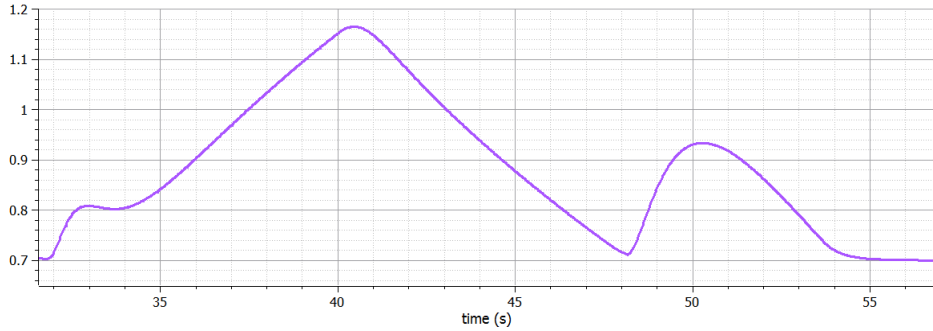


Figure 4.7: Zero-sequence energy sum of the MMC during the simulation in p.u.

The blade angle used in the Pitch controller is depicted in fig. 4.8

### 4.3 Dampening power fluctuations from the wind turbine

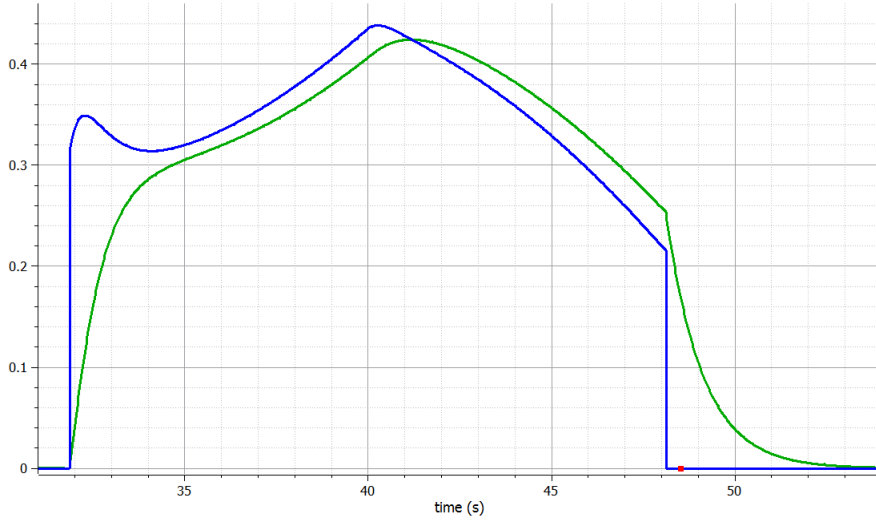


Figure 4.8: Blade pitch angle in green and blade pitch angle reference in blue

The energy dynamics of the wind, turbine, and MMC are depicted in figs. 4.6 and 4.7. For clarity, the profiles should be broken down into several regions. When  $30s \leq t \leq 35s$  the wind speed increases from below its threshold value and linearly increases towards above its threshold value. Thus, the rotational speed of the turbine also increases. When the wind speed exceeds its rated value, then the speed controller activates, and the generated torque increases to slow the rate of change of the rotor speed. Simultaneously, the pitch controller activates, to reduce the input torque, but before the pitch angle reaches its reference, there is an increase in power delivered to the HVDC grid. When the controller used in fig. 2.11 is used, the stored energy in the converter increases and thus absorbs some of the increased power output. The consequence of this is that the power perturbation delivered to the grid is reduced by approximately 30%, and the overshoot is reduced by 80%, see fig. 4.9.

Subsequently, while  $35s \leq t \leq 40s$ , the wind speed is above its threshold value and increasing. During this period, the power produced by the turbine exceeds its rated value, and the converter utilizes this and stores more energy. Thus, the power delivered to the grid is slightly lower and does not overshoot as much when the controller in fig. 2.11 is used. When  $40s \leq t \leq 46s$  the wind speed descends and the power produced by the

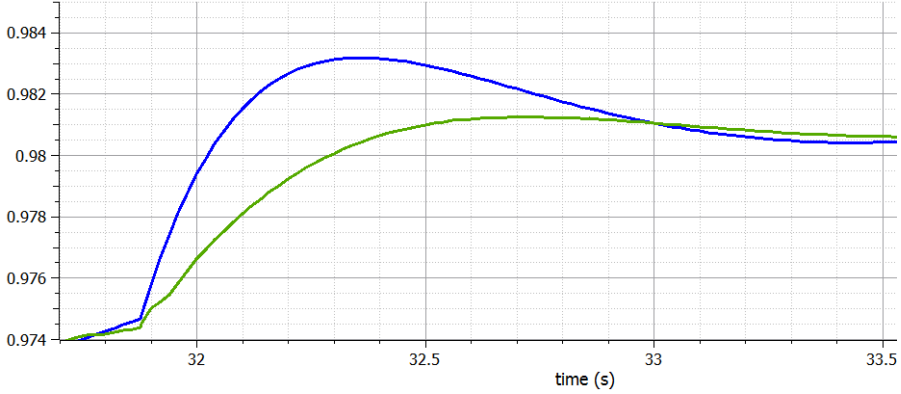


Figure 4.9: Zoomed image from fig. 4.6. In the green power response  $w_{\Sigma,z,ref}$  is controlled, while in the blue response it is set to be 1

turbine is slightly lower than the rated value. Thus, the converter releases energy and the nadir of the power delivered to the grid is somewhat elevated, by approximately 0.002 p.u.

When  $46s \leq t \leq 50s$  the wind speed drops below its threshold value, and the rotational speed of the generator declines. This is because of the speed controller, which reduces the rotational speed of the turbine when the wind speed is below rated value. Consequently, the turbine releases some of the rotational energy stored in the generator. Simultaneously, the pitch angle controller changes the pitch angle, which changes  $C_p$  increasing the power flowing into the turbine. When the controller in fig. 2.11 is used, the converter captures some of the energy reducing the change in power output to the grid by 6% as well as delaying the peak to 2 second - rather than 1.5 seconds - after the turbine starts to decelerate. When  $55s \leq t$  the turbine re-accelerates and the power output from the turbine is reduced. Here, the converter cannot release energy, because the energy level reaches 0.7 p.u. and the controller does not allow the converter to operate below this level. Thus the power profiles in the two scenarios align.

As the simulations show, most of the power fluctuations of the turbine cannot be mitigated by the MMC. However, the briefer the fluctuations are, the greater the relative impact of the MMC.

## 4.4 Using stored energy to improve the step response of the power output

To investigate the ability of the MMC to improve power dynamics on the time-scales of milliseconds, the reference of the stored energy in the converter will be controlled to improve the step response of the converter in delivered power. Two controllers will be tested for this investigation: a PI controller and a behavior-based controller. The system of investigation is depicted in fig. 4.10.

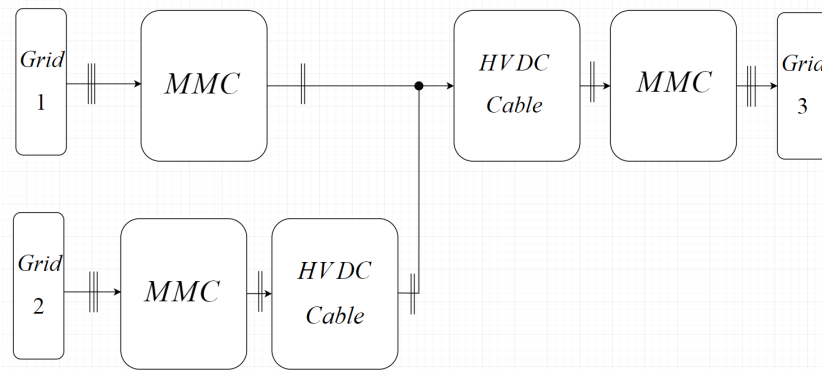


Figure 4.10: Multiterminal HVDC system used to investigate if the energy storage capabilities of the MMC can improve the power flow to Grid 3

The simulation scenario is an increase in the power reference of the rightmost MMC at  $t = 1s$ . No other references are altered, and all grids are assumed stiff.

### 4.4.1 Base case

In the base case, the reference  $w_{\Sigma,z,sum}$  of the power controlling MMC is kept at 1. This scenario serves as a basis for comparison to the two controllers used subsequently. The power curves from the base case are depicted in fig. 4.11.

When the power reference changes, this causes the reference for the d-component of the

## Chapter 4. Simulation and results

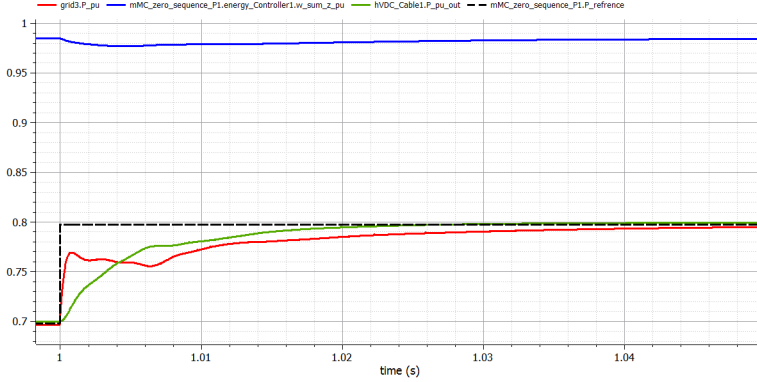


Figure 4.11: Power profile during unaided reference step at  $t = 1.0$ . The green profile is the power delivered to the converter from the HVDC-cable, the red profile is the power delivered to the grid, the blue profile is  $w_{\Sigma,z,pu}$  of the power controlling converter, and the black dotted line is the steady-state power to grid

grid current and thus the d-component of the converter voltage to spike. Therefore, in accordance with eq. (2.41), the stored energy of the converter drops. This change in stored energy,  $\Delta w_{\Sigma,z,pu} \approx 0.9847 - 0.9806 p.u. = 0.0036 p.u.$  released over 1 millisecond equals about 72360 J. This constitutes  $0.07 S_{base}$  which explains why the power delivered to the grid (in red) exceeds the power delivered to the converter (in green). Additionally, the voltage of the DC-capacitor declines by 0.01 p.u. during the same period, but the relatively small size of the DC-capacitor ( $1.67 \cdot 10^{-6} F$ ) coupled with the absorption of reactive power from the inductance of cable, makes this energy release a negligible contribution. Thus, the difference between the power to and from the converter stems almost exclusively from the stored converter energy of the submodules. Specifically, this explains the somewhat odd power to grid profile seen in the first step of fig. 4.11. The initial rise of power delivered of about 0.07 p.u. comes directly from the submodules of the converter. During the subsequent 4 milliseconds, the converter continues to release energy and  $\Delta w_{\Sigma,z,pu} \approx 0.9806 - 0.9770 p.u$  roughly equals  $0.02 S_{base}$ . However, this is not sufficient to maintain a power output difference relative to the power flowing into the converter from the HVDC-cable. Thus, the difference between the input and output power of the converter diminishes over time until the converter starts to recharge 5 milliseconds after the step. Because of this recharging, there is a period of approximately 1 millisecond where the power flowing out of the converter is steady although the power

---

## 4.4 Using stored energy to improve the step response of the power output

---

flowing into the converter is steadily increasing. Subsequently, the power output of the converter rises towards its reference.

### 4.4.2 PI controller

To investigate if the power step response of the system could be improved, it is attempted to control  $w_{\Sigma,z,ref}$  by using the PI controller explained in section 2.2.2. The dynamics of the system when this PI controller is implemented is depicted in fig. 4.12.

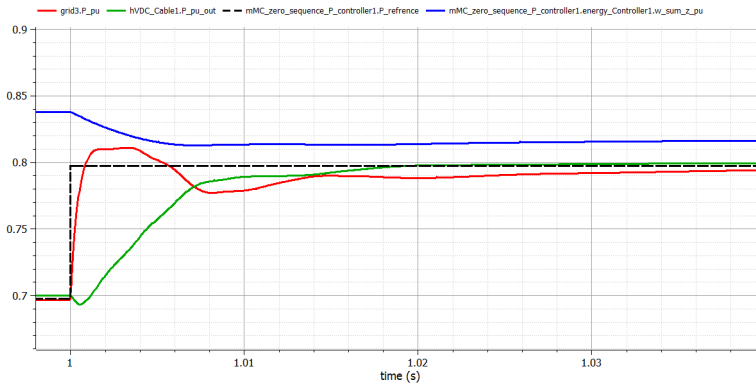


Figure 4.12: Power profile during reference step at 1.0 using PI controller to control  $w_{\Sigma,z,ref}$ . The green profile is the power delivered to the converter from the HVDC-cable, the red profile is the power delivered to the grid, the blue profile is  $w_{\Sigma,z,pu}$  of the converter, and the black dotted line is the steady-state power to grid.

Initially, it was observed that the power delivered to the converter changes shape compared to the previous step simulations during the initial phase of the step response, i.e., the first millisecond. Instead of rising, it initially drops before recovering. This behavior can be explained by considering the spike in the circulating voltage. This causes  $2v_{\circ} > v_{DC}$  which changes the voltage polarity over the arm inductor, which contributes to a reduction in the DC-current. Thus, there is a reduction in the energy stored in the magnetic fields surrounding the cable as a consequence of its inductance. However, there is a more substantial energy consumption related to the change in the electric fields of the cable, due to its capacitance. The difference between these two factors manifests as the

drop in power. This effect is subsequently counteracted, as the DC voltage slightly drops and the cable discharges its extra energy. After the first millisecond, the power output of the cable exceeds the power input. This is a result of the capacitive characteristics of the cable.

This happens only when a PI controller is used to determine  $w_{\Sigma,z,ref}$ , because of the proportional gain in the PI controller. This causes an immediate spike in the circulating voltage, which is not present in the case with the behavior-based control. This behavior would not be present if a pure integral controller would be used either.

Apart from the initial transient associated with the charging and discharging of the cable, a more oscillatory behavior emerges when the PI controller is used. This relates primarily to the dynamics introduced by the integral gain in the PI controller. The initial overshoot is roughly 14% of the step-size, and the subsequent undershoot is approximately 20%. Furthermore, the time until the power delivered to the grid is within 5% of the step-size of its reference is 33 milliseconds after the step. This makes it appear as if the controller does not improve the speed of the converter compared to no active control of  $w_{\Sigma,z,ref}$ . It should, however, be noted that the power delivered to the grid is within 20% of the step-size of the reference within only 0.5 milliseconds.

### 4.4.3 Behavior-based control

As shown above, utilizing a PI controller inevitably introduces some oscillations resulting from the dominant integral gain of the controller. To combat this, another control design was tested.

The task of the controller is to change  $w_{\Sigma,z,ref}$  to release energy, and thus rapidly elevate the power response of the system, faster than the power controller can. The first task related to the development of this controller is to understand the amount of energy which must be released as a function of the step in power reference. Fortunately, the shape of the power profile is the same, regardless of the size of the step. This is because the

#### 4.4 Using stored energy to improve the step response of the power output

increased or decreased step size always exists in inverse proportion to the error signal and thus control signal of the controller. This would not always be the case in reality, because of randomness, physical deterioration, inaccurate measurements, etc.

Assuming deterministic system behavior, the required energy can be estimated by integrating the difference between the power reference and the power delivered to the converter, i.e., the dotted black line and the green line in fig. 4.11, which is zoomed and colored in fig. 4.13. Based on this estimate, a generalized rule can be developed for any step-size.

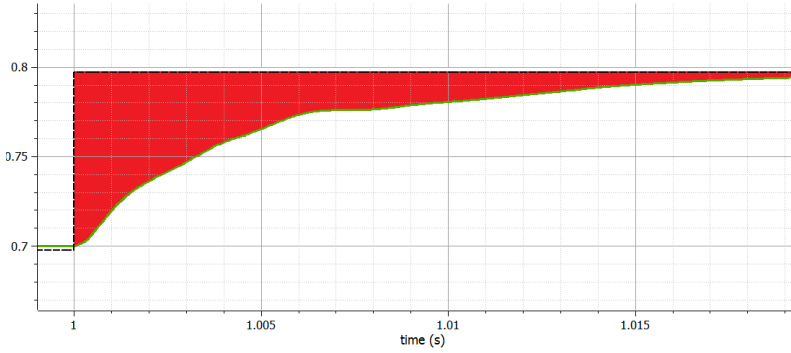


Figure 4.13: Illustration of the needed energy to be released by the converter

Using proportionality, the change in  $w_{\Sigma,z,ref}$  can be calculated based on this difference. An estimate of this energy can be found by simply counting the rubrics encapsulated in the red area. There are roughly 50 such blocks of height  $0.01S_{base}$  and width  $0.001s$ . Thus, this should manifest as an energy output in accordance with eq. (4.3).

$$w_{step} = \frac{S_{base} \int_{t=1}^{t=1.02} (P_{ref} - P) dt}{3w_{base}} \approx \frac{10^9 * 50 * 0.001 * 0.01}{3 * 6.7 * 10^6} \approx 0.025 p.u \quad (4.3)$$

Given the acceptance of an overshoot coupled with the fact the number produced by eq. (4.3) is only a rough approximation,  $0.033p.u.$  was found as an improvement. Because this was calculated based on a step of  $0.1p.u.$ , in general, a step in  $w_{\Sigma,z,ref}$  of  $0.33 p.u.$  for every unit step in power reference was implemented in the controller.

## Chapter 4. Simulation and results

The second characterization of  $w_{\Sigma,z,ref}$  which must be determined relates to the shape of its profile. Because  $(P_{ref} - P)$  resembles  $ae^{-bt}\forall[a, b] \geq 0$  and thus  $\int(P_{ref} - P)dt$  must have the same shape, an exponentially decaying function was selected. The rise time constant was selected based on the desired speed of the controller to 0.01s.

Furthermore, because the converter should recover the dispersed energy, the converter enters a recharge period which was chosen to equal 10 seconds. This recharge period is initiated one second after the step in power reference. Thus, during the discharge period, the zero-sequence energy sum reference is described by eq. (4.4). The parameters used in eq. (4.4) can be found in table B.8. During the recharge period, the same function is used, but the sign of the step changes and  $t_{recharge}$  replaces  $t_{RTC}$ . The resultant profiles are shown in fig. 4.14.

$$w_{\Sigma,z,ref} = w_{offset} + w_{step} \left( 1 - e^{-\frac{(t-t_{step})}{t_{RTC}}} \right) \forall t \geq t_{step} \quad (4.4)$$

The power delivered to the grid,  $w_{\Sigma,z,pu}$ , the steady-state power output, and power delivered from the HVDC-cable to the converter are depicted in fig. 4.14

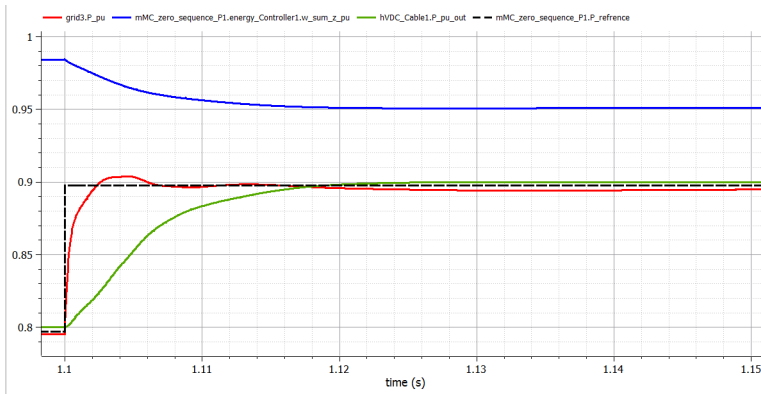


Figure 4.14: Power profile during reference step at 1.1 using behavior-based control. The green curve is the power delivered to the converter from the HVDC-cable, the red is the power delivered to the grid, the blue is  $w_{\Sigma,z,pu}$  of the converter, and the black line is the steady-state power to the grid.

During this simulation, several of the dynamics mentioned section 4.4.1 are present again. However, the critical distinction, in this case, is that the stored energy of the converter

descends further and does not oscillate thereafter. Thus, the power delivered to the grid is within  $P(t = 1.1) + \Delta P * 0.95\%$  after 1 millisecond, which is 32 times faster than in the case where  $w_{\Sigma,z,ref}$  was unchanged. A small overshoot, equal to approximately 6%, does appear. This relates to the selection of  $w_{step}$ , which was chosen to be slightly larger than the integrated difference of the power delivered and the power reference would indicate. This does, however, make the controller faster than it otherwise would have been. There is also a small undershoot in power delivered due to the dynamics of the system discussed in the PI controlled case. This undershoot is equal to 0.035% of the step-size, which is close to 3 orders of magnitude less than in the PI controlled case.

## 4.5 Impact of feed-forward in DC voltage control

As recalled from eq. (2.55), the feed-forward term in the voltage controller did not include the term that related to the zero-sequence energy sum. This section investigates the impact of its inclusion. Thus, the new feed-forward term,  $ff_{vc2}$ , used in the voltage controller is expressed by eq. (4.5).

$$ff_{vc2} = i_{cable,pu} \frac{v_{DC,pu}}{v_{c,d,pu}} - \frac{2w_{base}}{S_{base}v_{c,d,pu}} \frac{d}{dt} w_{\Sigma,z,pu} \quad (4.5)$$

Two steps were executed, first a step of 0.1 p.u. in  $w_{\Sigma,z,ref}$  at  $t = 3s$  and subsequently one step of 0.1 p.u. in  $v_{DC,ref}$  at  $t = 4s$ . The system used in this simulation is depicted in fig. 4.15.

The p.u. DC voltage and zero-sequence energy sum following the first step with and without the feed-forward terms are shown in fig. 4.16.

As can be seen, when the zero-sequence energy sum increases, attempting to reach its reference, the DC voltage drops. This can be understood in an energy perspective, by considering that the extra energy needed to charge the submodules is partly being drawn from the DC-capacitance and cable. It could also be understood by considering the dynamics of the energy controller. When  $w_{\Sigma,z,ref}$  increases, so does also  $i_{\circ,z,ref}$ .

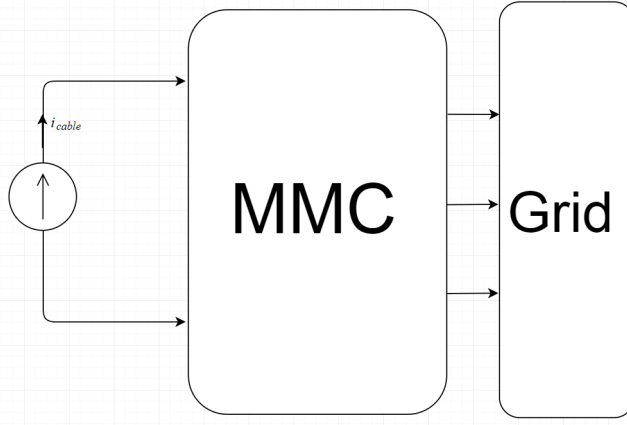


Figure 4.15: Model used to investigate the impact of the feed-forward term described by eq. (4.5)

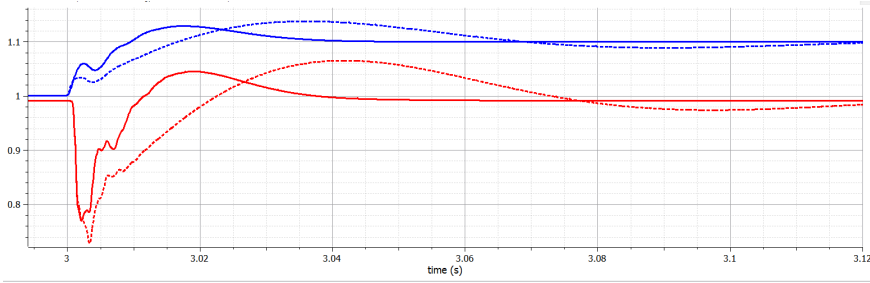


Figure 4.16:  $v_{DC}$  (red) and  $w_{\Sigma,z,pu}$  (blue) during a step in  $w_{\Sigma,z,ref}$  of 0.1 p.u. at  $t = 3$ s. The dotted lines are without the new feed-forward and the dotted are with the new feed-forward

Because of the minus sign in the proportional and integral terms in the PI controller for the circulating current,  $K_{\circ,cc,p}$  and  $K_{\circ,cc,i}$ ,  $v_{\circ,z}$  drops. Because of the arm inductance on the DC-side of the model,  $i_{\circ,z}$  cannot instantly change, and thus the voltage drop in circulating voltage must manifest as a voltage drop in the DC voltage.

Regardless of the implemented feed-forward, these steps result in voltage drops on the DC-side. This is because of the immediate nature of the reduction in circulating voltage, which must cause the voltage drop over the DC-side capacitor to occur. This, in part, relates to the fact that the circulating voltage immediately drops because of the proportionality

## 4.5 Impact of feed-forward in DC voltage control

terms in the controllers, while the zero-sequence energy does not immediately react. Thus, the improvement of the feed-forward cannot be instant. Furthermore, the voltage control loop is not infinitely fast and cannot react instantly to any change.

However, a significant difference in how the voltage recovers can be seen when considering the two implementations. In the case with the new forward, the DC voltage quickly rises, overshoots and descends to its reference. The overshoot peaks at 1.045 p.u. and the nadir of the profile is at 0.77. The DC voltage is within one percent of its reference within 37 milliseconds. This is a significant improvement compared with the case where the feed-forward is not implemented. When there is no implementation of this, the nadir descends to 0.728, the overshoot ascends to 1.066 and the time until the DC voltage is within one percent of its steady-state value increases to 110 milliseconds. This is mostly because the DC voltage follows the circulating voltage, which follows the oscillations in the zero-sequence energy sum. When the feed-forward term is introduced, neither state oscillates like this.

The p.u. voltage and zero-sequence energy profiles during the second step are depicted in fig. 4.17.

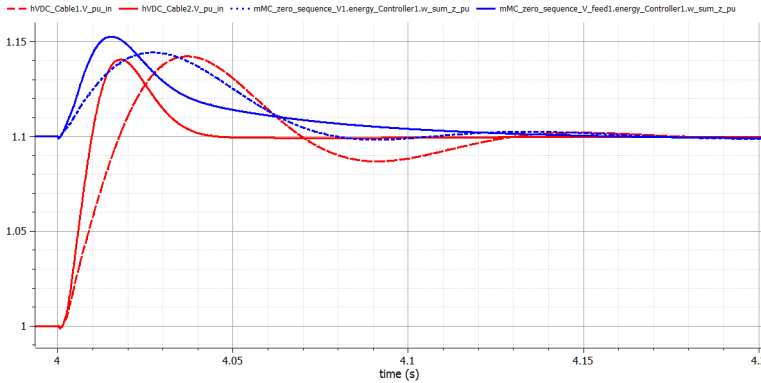


Figure 4.17:  $v_{DC}$  (red) and  $w_{\Sigma,z,pu}$  (blue) during a step in  $v_{DC,ref}$  of 0.1 p.u. at  $t = 4s$ . The dotted lines are without the new feed forward and the dotted are with the new feed forward

Again, a complete decoupling is not achieved in either case because of the fast dynamics of the system. As can be seen, when  $v_{DC}$  starts to rise, then this causes some change to  $w_{\Sigma,z}$ .

## Chapter 4. Simulation and results

---

To clarify this change, the course of events will be briefly recapitulated. At the moment of the step,  $v_{c,d}$  immediately falls due to the proportional gain of the PI controller in the voltage and current controllers and the sudden error in DC voltage. This causes  $w_{\Sigma,z,pu}$  to fall slightly in accordance with eq. (2.41), approximately 0.0004 and 0.001 p.u. with and without the feed-forward respectively. Subsequently,  $i_{g,d}$  increases in magnitude. It is recalled that due to the sign convention used here,  $i_{g,d}$  is negative. Thus, when its magnitude increases and  $v_{c,d}$  resumes normal levels, then this causes  $w_{\Sigma,z}$  to increase.  $w_{\Sigma,z}$  continues to rise until  $i_{g,d}$  reaches its new steady state level and then gradually declines towards its reference. As  $|i_{g,d}|$  rises (i.e., becomes more negative), so does the DC voltage rise and eventually reaches its new steady state value.

As can be seen, the performance of the DC voltage is significantly improved using the feed-forward mechanism described here. The time it takes the DC voltage to be within one percent of its reference for the last time within 30 milliseconds and 100 milliseconds with and without the feed-forward respectively. Furthermore, the DC voltage is practically without oscillations, and the overshoot is slightly lower, about 2 % of the step height. It is noteworthy that the elevation of the zero-sequence energy sum is higher with this feed-forward implementation, which is presumably due to the faster nature of the DC voltage.

# Chapter 5

## Discussion

To put the discussion in the correct context, the purpose of the discussion is initially explained in light of the objectives of the thesis. Firstly, the validity of the suitability demonstration of OpenModelica is discussed. This is because the subsequent investigation of the positive impact of the MMC on the HVDC power dynamics depends on this validity. Thus, OpenModelica's ability to capture dynamics of interest is first discussed as well as its general reliability. Then, as it provides further insight into the software's reliability, operational performance, and area of usage, a discussion of the real-time simulation of the integrated OpenModelica models is conducted.

Once the software is sufficiently established, a discussion of the power dynamics of the HVDC system follows. Initially, the dampening effect the MMC can have on the relatively slow turbine dynamics are discussed. Then, how the MMC can reduce the response time of the HVDC system upon a step in power reference is examined. Lastly, the decoupling effects of the feed-forward term in the voltage controller are considered.

## 5.1 OpenModelica's suitability to model HVDC systems

The original purposes of the simulations which are discussed here are whether OpenModelica can model relatively high-frequency dynamics and produce models that can be integrated with real-time simulation tools. However, since these simulations also, to an extent, reveal insights into OpenModelica's resilience to discontinuities and handling of algebraic loops, these aspects are also discussed.

### 5.1.1 Modeling of high frequency dynamics

#### Differences in produced dynamics

Close inspection of fig. 4.1 reveals that the produced dynamics of the two software are not identical. Considering the ripple on the zoomed part of fig. 4.1, it can be seen that the ripple in the OpenModelica model is larger than in the MATLAB model. One explanation for this is that the modeling of switches is different. The "IGBT/diode"-block used in MATLAB does not instantly reduce the current through the component to 0, but instead linearly decreases it over two periods using two different rates of change [116]. Moreover, the "IGBT/diode"-block uses a snubber resistance together with an infinitely large snubber capacitor. This RC snubber affects the voltage over the "IGBT/diode" component which, in turn, affects  $v_c^{123}$ . Lastly, an inspection of the IGBT block from the same library revealed that a snubber inductor is used to limit the rise of the current in the IGBT model [116]. The "IGBT/diode" states that it uses a simplified version of the IGBT block, with no forward voltage, but does not address the inductor [117]. If that inductance is not forced to zero by default in the "IGBT/diode"-block, that would also contribute to the smaller current ripple.

The modeling differences of the switches are, therefore, presumed to cause the differences seen in the dynamics produced by the models. Hence, these differences are not con-

sidered evidence that OpenModelica cannot capture relatively high-frequency dynamics adequately.

### **Software resilience to discontinuities**

As mentioned in section 3.1, MATLAB was not able to simulate the system unless a delay was added to every measured signal, because of the presence of an algebraic loop. Furthermore, MATLAB was not able to simulate the system dynamics using a fixed step-time solver, only when using a variable step-time solver when the delay was a memory block. A potential reason for why MATLAB produces different dynamics when using a fixed step time solver is that the fixed step solvers used in MATLAB expect every state to be continuous during each step. However, the memory block produces discrete signal outputs [118]. Two attempts were made to mitigate this. Firstly, changing the time-step of the model was tested, but even reducing it down to 10 ns did not result in correct dynamics produced by the fixed time-step solvers. The second mitigation attempt was to replace the memory block with a continuous delay. When this replacement was introduced, the fixed step time solvers in MATLAB accurately produced the correct dynamics. Introducing the same delay in the OpenModelica had only one noticeable consequence: the run-time almost doubled when a variable step solver was used.

This would indicate that MATLAB's fixed time-step solvers are not able to correctly calculate the states of the system when discontinuities like these are introduced. Interestingly, the fixed time-step solvers in OpenModelica did produce the correct dynamics, although the model of the switches produces discontinuities in the states.

### **Handling of Algebraic loops**

Another observation is that OpenModelica did not require any mitigation to algebraic loops in the model, unlike MATLAB. This might speak to a difference in how the two software compile models. This is challenging to confidently say since MATLAB is not as

transparent regarding their inner workings as OpenModelica. However, analyzing how OpenModelica sorts its equations and variables presents some insight into this. Since OpenModelica is equation based, the compiler must go through each equation and decide which variable it should solve for to produce an assignment statement. Moreover, the sorting algorithm groups sets of equations that are cyclically dependent together into blocks which are solved simultaneously [119]. Subsequently, further optimization is conducted on the system of equations. One specific example of this relates to algebraic loops [120]. This includes tearing, i.e., restructuring algebraic loops (see fig. 5.1), and generating symbolic jacobians, i.e., taking a nonlinear set of equations and producing a set of linear equations for each nonlinear equation by differentiating each equation with respect to the state [121].

This is an indication that OpenModelica handles an extensive system of equations, algebraic loops, and discontinuities differently than MATLAB in a way that appears more resilient to these aspects.

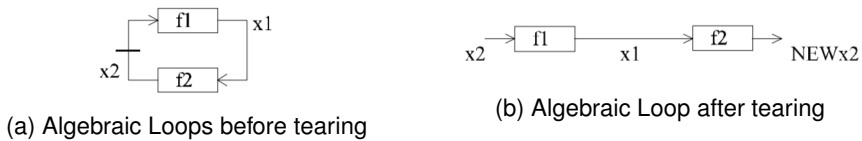


Figure 5.1: Tearing of algebraic Loop[122]

### Run-times

The run-times of the two software were substantially different. During the initial simulation, OpenModelica ran about 40 times slower per simulated second. When simulated in OpenModelica, the simulation time was approximately 1317 seconds per simulated half-second, while MATLAB used about 33 seconds. The most probable reason for this is that the components used in MATLAB and OpenModelica to model the switches are different. This is somewhat challenging to investigate in depth because MATLAB does not provide detailed descriptions of their IGBT models. However, an interesting observation is that the turn off characteristics of the IGBT model in Simulink is modeled in

---

## 5.1 OpenModelica's suitability to model HVDC systems

---

two steps with linear current descend [116]. This allows MATLAB to model the system without needing to introduce discontinuities in the flow and potential variables of the system. Thus, if future efforts are to be made of building converter models containing switches in OpenModelica, this thesis recommends constructing IGBT with continuous characteristics, to see if this improves the run-time of the simulation.

The reason the run-time difference is presumed attributable to the model of the switches is that when similar verification attempts were made in [68], no significant difference in run-time was detected. Furthermore, in [68], the voltages applied at the converter terminals were not produced by connecting the phases to the DC-side in an alternating manner using switches, but rather by alternating the reference of controllable voltage sources between  $v_{DC}/2$  and  $-v_{DC}/2$ .

In general, it has been demonstrated that OpenModelica can capture relatively high-frequency dynamics based on a comparison with MATLAB Simulink. Since all the dynamics of interest in the simulations investigating HVDC power dynamics are of lower frequency than the ones studied here, OpenModelica is considered reliable for these investigations. Furthermore, OpenModelica proved more versatile and resilient to modeling problems such as discontinuities and algebraic loops, requiring no modeling effort to mitigate these issues. Moreover, whereas MATLAB produces different dynamics depending on the solver and the presence of discontinuities, OpenModelica produced the same dynamics irrespective of the solver. Lastly, the differences in run-time and produced dynamics are not presumed to be because of differences between OpenModelica and MATLAB Simulink but is more likely attributable to modeling differences of the switches. Some research has already been done that supports this [68], but future research is needed to affirmatively state the only contributing factor to this difference is the modeling of the switches.

## 5.1.2 Integration of OpenModelica models with real-time simulation tools

Two systems were simulated with ePHASORsim, shown in figs. 3.5 and 3.6. In both cases, the models produced expected dynamics illustrating that the interfaces used to integrate the OpenModelica models worked as intended. This demonstrates the important and attractive feature of OpenModelica that its models can be run using real-time simulators such as Opal-RTs ePHASORsim.

However, only the model containing the MMC could run successfully with a time-step of  $100\mu\text{s}$  and was thus the only model which could be run in a real-time simulation. The exact reasons why the system containing the HVDC-link could not run using a similar time-step remains incompletely understood, due to time constraints. Nonetheless, some hypotheses were tested and subsequently ruled out. It was initially assumed that the HVDC-link model contained variables that oscillated or stepped too quickly. That is, when the time-step was too large, the solver might calculate that the values were too far from their actual values and then over-correct in the next iteration, causing instability. To test this, the system was re-tuned to be slower so that all the dynamics of the system were slower than the ones in the MMC model. Still, simulations with a time-step of  $100\mu\text{s}$  resulted in instability. The second hypothesis related to the solver used by ePHASORsim. When the HVDC-link model was tested in OpenModelica, the implicit solver Dassl was used, which was not available in ePHASORsim [123]. This hypothesis was also quickly ruled out, as the Runge-Kutta solver modeled stability when used by OpenModelica and instability when used by ePHASORsim.

This also demonstrated that the problem is presumably not related to the construction of the model because when simulated in OpenModelica using the Runge-Kutta solver, the system was stable. This might be indicative that OpenModelica compiles models differently than ePHASORsim, analogous to the compiling differences between OpenModelica and Matlab discussed in section 5.1.1. One hypothesis related to this is that before a model can be executed, the OpenModelica Compiler translates the model to executable simulations in several steps [119]. As it is said in [119] "[...] the performance

---

## 5.1 OpenModelica's suitability to model HVDC systems

---

of the numerical simulation can be improved one or several orders of magnitude by this symbolic preprocessing, as well as improving numerical stability of the solution process". Thus, if the FMU creator generates the FMU based on the unflattened, unprocessed model, and ePHASORsim uses a different technique to preprocess it, this might, at least in part, explain why ePHASORsim is unable to simulate the HVDC system at  $100\mu s$  while OpenModelica can.

A concrete example of this could be that OpenModelica is very efficient in reducing the number of equations that describe a system during the preprocessing. Thus, the system that the fixed time-step solver, e.g., Runge-Kutta, needs to solve is smaller in OpenModelica than it would be in ePHASORsim. For instance, 305 out of the 435 equations describing test model for HVDC\_base are recognized in OpenModelica as trivial equations. As has been proven in [124], every fixed time-step solver has a time-step stability limit, meaning that for a given system, if the time-step is too large, the system becomes unstable. This could be investigated by simplifying the HVDC-link model, by, for instance, constructing it in the dq-reference frame or by describing the system equations as equations, rather than by using electrical components. However, it is not suggested that computational complexity or model size is a probable cause for why this instability emerges as the time-step becomes too large. It is stated as a possibility to provide some insight into where the problem might reside, as a suggested starting point for further research.

Lastly, it might be questioned what advantages the fact that OpenModelica is free can bring if the models are integrated using the Simulink environment for real-time simulation. However, it must be remembered that this still allows for more comfortable sharing of models across socioeconomic borders. Moreover, this still allows several engineers to collaborate on developing models in OpenModelica and then conducting real-time tests requiring only one Simulink license.

In conclusion, models developed in OpenModelica can be integrated with real-time simulation tools. However, further research into the limits of this integration is needed to understand why some models cannot be run with sufficiently large time-steps.

## 5.2 Controlling the MMC to improve HVDC energy dynamics

It is briefly recalled that the overarching objective of this part of the thesis is to gain some insight into how the zero-sequence energy of the MMC should be controlled to improve HVDC system performance. Moreover, to what degree can the zero-sequence energy sum and DC voltage be decoupled using a feed-forward term in the voltage controller.

An initial observation that relates to all the simulations is that the voltage controller, as predicted, needed to be re-tuned. The re-tuning was achieved by decreasing the integral gain of the PI controller,  $K_{vc,i}$ , by a factor 15. This re-tuning can be explained by considering the assumptions made during the derivation of the analytic expression for the gains. One of the critical assumptions made was that everything inside the voltage controller could be modeled as a delay equal to the equivalent time constant of the current control loop. This would be true, if the second assumption were correct, namely that the term relating to the zero-sequence energy sum could be neglected in the tuning process. However, because of the energy storage ability of the converter, changes made to the power flow on the AC-side of the converter, do not immediately manifest on the DC-side. After the delay associated with the AC-side currents, the energy controller must respond to this power perturbation before it affects the DC-side. This additional delay can be accounted for by making the voltage controller slower by decreasing the integral gain of the controller.

### 5.2.1 Dampening power fluctuations from the wind turbine

As shown, the suggested way of controlling the zero-sequence energy sum reference can reduce certain power fluctuations of the turbine to some extent. The fluctuations that were dampened the most were caused by the wind speed exceeding its rated speed, causing the speed controller to decelerate the turbine generator. As was shown, the faster the fluctuations of the turbine, the more significant the relative impact of the MMC.

### Assessment of result validity

The speed of the energy dynamics of the turbine closely relates to its inertia. The greater the inertia, the slower the energy dynamics because the turbine accelerates more slowly. In this simulation, the inertia of each wind turbine was  $3 * 10^6 \text{ kgm}^2$ , and the rated power of the turbine was only 2 MW. According to Sintef, a typical 2 MW wind turbine has more than twice that inertia [125]. Furthermore, the average wind turbine used for offshore purposes is 3.6 MW [126], which indicates that the impact of the MMC seen in this thesis might be an overestimation.

Moreover, allowing  $w_{\Sigma,z}$  to fall to 0.7 p.u. would imply that the voltage level of each submodule is reduced to  $\sqrt{0.7} \approx 0.83$  of its rated voltage value. This is due to the quadratic relationship between voltage and energy of a converter. This implies that the total arm voltage is approximately 20% more than the peak of the sinusoidal grid voltage peak to avoid over-modulation. This is more than twice as high as has been suggested by some researchers indicating that 10% is more fitting [127], [128].

For these reasons, the results presented here might overestimate the influence the MMC can have on the energy dynamics of wind turbine caused by wind fluctuations. When this is considered together with the fact that the impact found was close to negligible for most of the energy dynamics introduced by the turbine, it might be argued that the energy storage of the MMC is not well suited for smoothing out such fluctuations. This is because the total energy storage capability of the converter is too small when considering the time scale and magnitude of these variations.

### How can the positive MMC impact be improved

It is possible to design MMCs to improve its positive impact on these types of dynamics. The base value of the zero-sequence energy sum used in this simulation is  $6.79 * 10^6$  Ws. That means that the converter can supply 10% of the rated power for approximately 2 seconds, assuming it discharges completely. Therefore, it is quite natural that its ability

to effectively alter the power profile of the power delivered to a grid is quite limited. However, the storage capability of the converter could be improved in the future. For a brief analysis of this, the storage capability of the converter is recalled in eq. (5.1)

$$W = 3 \frac{C_{SM}}{N} (N * V_{SM})^2 \quad (5.1)$$

where  $C_{SM}$  and  $V_{SM}$  are the capacitance and voltage rating of the submodules respectively. It will be assumed that  $NV_{SM} = V_{DC}$ . Furthermore, it is assumed that lower limits on how much energy can be released is constitute by how low the energy level can get before over-modulation is unavoidable. It is thus assumed that the MMC is designed so that a certain fraction of its energy can be released before this happens and that the excess energy is proportional to its energy capacity.

The first consideration relates to the DC voltage and especially if this could be increased in the future. This would increase the arm voltage and thereby increase the amount of energy stored in the converter. The DC voltage used in this simulation is  $\pm 255.5$  kV, which is lower than the voltage used in e.g., the UK western Link [129]. Future projects, such as the North sea link, is expected to operate at  $\pm 515$  kV with a capacity of 1400 MW [130]. If such voltage levels are used in future offshore HVDC systems, then that would increase the storage capability of each converter by a factor of 4 compared to the MMC used in this simulation while only increasing the  $S_{base}$  by 40%. It is also possible to simply have more submodules, if their contribution is economically feasible. This would also improve reliability through redundancy.

The second consideration addresses the capacitance of each submodule. Submodule capacitance is typically chosen based on a voltage fluctuation constraint [131]. That is, to mitigate variation in submodule voltage, a lower limit is placed on the submodule capacitance because  $C_{SM}$  is inversely proportional to  $\frac{dv_{SM}}{dt}$ . This is to ensure that the lowest voltage level of the arm voltage does not fall below the grid voltage amplitude. The purpose of the design is, therefore, typically to minimize the submodule capacitance to cut costs and reduce the size of the converter [132]. However, the power density of power electronic converters has roughly doubled every decade over the past 50 years [133]. It is therefore *possible* that future converters can be designed with higher submodule capaci-

tances and thus have improved energy storage capabilities.

Lastly, in a multi-terminal HVDC grid, several MMCs can contribute to smoothing out the power flow to the onshore grid, which could improve the performance further.

However, despite this potential, as the simulations show, the characteristics of the MMC storage capability do not make it particularly well-suited to reduce the power fluctuations associated with turbine dynamics caused by wind variation. The two main reasons for this are the two characteristics of the MMC energy storage capability: size and speed. The MMC can charge and discharge very quickly, which makes it more suited to handle dynamics related to step responses or similar quick energy bursts. The relatively slow nature of the turbine dynamics suggests that the total energy output needed to fill or absorb the gap between the power produced and its reference, quickly exceed the abundant converter energy. To reduce the power variations associated with the dynamics of the turbine caused by wind fluctuation, an energy storage system is needed presumably with energy storage capabilities of supplying rated power closer to one hour. This was investigated in [2], [68].

### 5.2.2 Using stored energy to improve the step response of the power output

As was shown, the power step response time of the HVDC system was reduced (by a factor of 32) when comparing the behavior-based control to the control where the zero-sequence energy sum reference was unchanged. Both the PI controller and the behavior-based controller were characterized by the same quick ascend towards the steady-state output, but differed in terms of overshoot, undershoot, as well as the time it took until the output power settled at its reference. This showed that both controllers, but especially the behavior-based controller, reduced the time the HVDC system needed to react to changes in required output power.

### Controller comparison

It could be argued that the PI controller could provide a greater range of services than the behavior-based controller. One reason for this is that the PI controller opposes any difference between the power reference and the power provided, not just in the case of a step in reference. However, this constant opposing coupling also comes with at least two associated challenges. The first is that the steady-state level of  $w_{\Sigma,z,ref}$  is more challenging to control. For the scenario studied here,  $w_{\Sigma,z,ref}$  should be close to 1 and only diverge when injections or absorptions of power are of great utility. As was shown in section 4.3, the power fluctuations related to turbine dynamics are sufficiently large and slow to potentially use all of the excess energy capability of the converter. The second point relates to general stability assessments of the system. Intuitively, having an energy storage component which systematically opposes fluctuations of any system state should only improve stability. However, whenever several controllers are cascade-connected, as is the case with the PI controlled  $w_{\Sigma,z,ref}$ , their mutual influence can be hard to predict under all scenarios, and such dynamics might reduce the system stability. For instance, when tuning the PI controller, it was found that for certain ranges of the proportional gain  $0 < |K_p| < 0.01$ , the system became unstable as a result of start-up transients. Thus, before such a control structure could be implemented, further research into system stability would be needed.

In contrast, the behavior-based controller would virtually always ensure that  $w_{\Sigma,z,ref} = 1$ , except when deviations are required. This would also reduce the controller's ability to worsen the system stability because it is not constantly coupled with other states of the system, but with changes in power reference. A consideration could be that because the controller has a predetermined response as a function of step-size, its behavior might not be sufficiently flexible if the system operates under non-ideal conditions. However, that holds for any inverted model-based controller. The only difference, in this case, is that the controller is not based on an inverted transfer function of analytically derived system behavior. Instead, it is based on a simulation of said behavior. However, physical deterioration of the system over time, or similar effects causing changes to the system behavior, could require more flexible controllers.

---

## 5.2 Controlling the MMC to improve HVDC energy dynamics

---

Another advantage of the behavior-based controller is that it can more easily be used together with other controllers. For instance, assuming that 20% of the stored energy of the converter can be used without over-modulation occurring, then during "normal" operation  $w_{\Sigma,z,ref}$  could be controlled for, e.g., power oscillation damping. The controller used for power oscillation damping would only be allowed to use 10% of the storage capability, while the remaining 10% is reserved in case of steps in power reference.

Overall, it can be said that the characteristics of the MMC's energy storage capability make it better suited to counteract power deviations, that are on the time-scale of milliseconds than several seconds. However, the use of a standard PI controller introduces oscillations because of its sizeable integral gain. This thesis showed that the same benefits of the PI controller, but without the oscillations, can be achieved by using a behavior-based controller. This suggests that controlling the zero-sequence energy to counteract faster power deviations is possible, but that the standard PI-controller is not the most suitable for this purpose.

### 5.2.3 Impact of a feed-forward term in voltage controller

As was seen, accounting for the coupling between the DC voltage and the zero-sequence energy sum by using a feed-forward in the voltage controller improved the performance of the converter with regards to steps in both variables. Generally, the response times of the stepped variables were reduced by a factor of 3, and their oscillations were practically removed.

This demonstrates that this type of voltage controller has benefits that are not easily achieved with standardized droop control. However, the benefit of this decoupling is not compared to the advantage of distributing the responsibility of DC voltage maintenance between several converters, which is the primary motivation for droop control implementation. However, when the number of converters in the system is small, then this type of control might be advantageous. However, before such conclusions can be confidently drawn, more research is needed into the impact this controller can have on a more realistic

and complex grid. It is possible that this type of control introduces more instability when delays, measurement errors, modeling inaccuracies, etc. appear in the implementation.

However, it has been conclusively demonstrated that the decoupling between the two states,  $v_{DC}$  and  $w_{\Sigma,z}$ , can be improved using a feed-forward in the voltage controller. Further comparisons of this controller and other designs have not yet been performed. Therefore, data presented in this thesis do not allow firm conclusions concerning, e.g., droop control. Moreover, this simulation highlights the difficulty of decoupling these terms when this control hierarchy is implemented. This is because the DC voltage can only be increased or decreased by changing the AC-side current flow. This, however, must firstly affect the stored energy of the converter before it can manifest as a change in voltage. If a complete decoupling is necessary, then it is recommended to use the voltage controller to determine the reference for the circulating current and to use the energy controller to set the reference for the AC-side currents, as in [46].

# Chapter 6

## Conclusion and future work

### 6.1 Conclusion

This thesis investigated energy dynamics relating to MMCs in HVDC systems and if OpenModelica is suited to model such systems.

There were three objectives that related to OpenModelica:

1. The first objective was a demonstration of its ability to model a system characterized by relatively high-frequency dynamics typical for power electronic systems. Comparisons between two switching models of a 10kHz 2L-VSC, one build in MATLAB Simulink and one in OpenModelica, showed that OpenModelica could accurately simulate such system dynamics. Thus, OpenModelica can be considered adequately accurate for modeling systems that are characterized by frequencies up to and including the ones tested here.
2. The second aspect related to weather models created in OpenModelica could be

integrated into a system simulated by real-time simulation tools. It was demonstrated that this integration is possible. Two systems were modeled and run using ePHASORsim. However, only one of the two models was suited for simulations with a time-step sufficiently large for real-time simulation. Further research is needed to understand why larger time-steps cause instability in the second model, as well as to what can be done to mitigate this.

3. The third objective was the development of a guide on how to integrate OpenMod-  
elica models for real-time simulation. This guide can be found in section 3.2.

Moreover, there were three objectives that related to power dynamics in HVDC systems and how the MMC can be controlled to improve them:

1. It was shown that the relative, positive impact of the MMC on HVDC power dynamics is greater the briefer the dynamics are. This was demonstrated by two simulation cases that differed in duration and required energy.
  - (a) Firstly, it was shown that control of the stored energy in the MMC yields minimal improvement to most of the power and energy dynamics related to wind fluctuations and turbine behavior. This related primarily to the time scales of these types of dynamics, which is quite slow compared to the charge and discharge time as well as the total energy storage capability of the converter.
  - (b) Secondly, it was shown that control of the internal energy sum of the converter reduced the power step response time (by a factor 32) of the HVDC system. However, it was shown that the standard PI controller is not optimally suited for this control task, compared to the behavior-based controller introduced in this thesis.
2. Thirdly, it was shown that the step responses of the DC voltage and zero-sequence energy sum of the converter could be improved by introducing a feed-forward term in the voltage controller to reduce their coupling. However, a complete decoupling was not achievable by using this technique.

## 6.2 Future work

Models developed during the work described in this thesis are all publicly available. Hopefully, some of these will be found useful for futures investigations, some of which are suggested below.

### 6.2.1 Modeling of switches

Currently, there does not exist any IGBT model in OpenModelica. The development of an IGBT could facilitate conclusive verification that the modeling of the switches was the only source of difference between OpenModelica and MATLAB seen in this thesis.

### 6.2.2 HIL-testing

In this thesis, a model of an MMC could run successfully using a real-time simulator and a time-step of 100  $\mu s$ . Thus, the controllers proposed in this thesis could be developed into hardware and tested using the principle of HIL, producing the system behavior with the proposed system equations and models.

To progress with the larger HVDC system models, efforts would have to be made in order to make the system models run with a larger time-step. Given that the model could be run using OpenModelica, but not ePHASORSim, with the appropriate time-step, one place to initiate this research is to investigate the differences in how the software compile models. Another approach would be to test intermediate models with regards to complexity to see if that is the cause of the issue. This could mean to attempt to run a real-time simulation of an MMC model developed in the 123-reference frame, model the HVDC link in the dq-reference frame or model the system dynamics of the HVDC link using equations, rather than electrical circuits.

### 6.2.3 Further development of the model

Several aspects of the HVDC system modeled in this thesis are simplified to the point where particular dynamics are ignored. However, the open source nature of this work makes it well-suited for expansion by others with interest in different dynamics. If, for instance, researchers with profound knowledge on turbine modeling are interested in investigating the effect of the MMC's energy dynamics on individual turbine features, this thesis has hopefully constituted a starting point. This could also allow for accurate comparisons aiming at determining how the energy storage capabilities of the MMC should be used, by enabling researchers with different research interest to quantify their improvement impact using the same model for different purposes.

Accurate development of the turbine model and its connection to the grid would be a rather natural contribution in this context. This would provide more precise power flows to the system, which could include faster dynamics than the ones discussed in this thesis. Some of these have already been studied, but others remain unstudied concerning potential improvements introduced by an MMC. Furthermore, this would allow research into the consequence of having weak grids as well as their dynamics impact on MMC based multi-terminal HVDC systems.

Another related topic is fault handling. One of the attractive features of multi-terminal HVDC grids is the ability to reroute power flows if needed during, e.g., faults. To investigate the potential contribution of the MMC's energy storage in such cases, the MMC models presented here should be further developed to be able to capture realistic behavior under such conditions.

Furthermore, this thesis did not include modeling of an external energy storage system, and although some dynamics related to this are investigated in [68] several other dynamics of such a storage system are not modeled, although mentioned in this thesis. By encompassing this as well in the model, the dynamic interactions of all of these components can be investigated.

---

By improving the accuracy of all these dynamic elements, and quantifying the improving impact the MMC can have on each component in a single modeling environment, either modeled in isolation or the entire system, quantitative comparisons between the impacts can be made. This could then suggest how the energy storage capability of the MMC can be best put to use. Furthermore, this could be used by any interested industry party who could alter the models to investigate how to use the energy storage capability when considering their specific cases. Hopefully, this will prove useful for further academic and industrial investigations.

Regarding control hierarchy, this thesis has demonstrated that the coupling between the DC voltage and zero-sequence energy sum can be significantly reduced by using a feed-forward term in the voltage controller. However, further research using side-by-side comparisons of all different control structure possibilities under various scenarios is necessary before affirmative conclusions can be drawn. This would especially relate to the number of terminals, and thus converters, employed in a multi-terminal HVDC grid.

---

# Reference List

- [1] E. V. Tranulis, 2019. [Online]. Available: [https://github.com/erlingvt/HVDC\\_system\\_models\\_Modeled\\_in\\_OpenModelica](https://github.com/erlingvt/HVDC_system_models_Modeled_in_OpenModelica).
- [2] J. Espvik, E. V. Tranulis, E. Tedeschi, and S. Sanchez, "Modeling of Multiterminal HVDC Offshore Grids with Renewable Energy and Storage Integration by Opensource Tools", *IEEE Transactions on Power Delivery*, no. 1, 2019, Unpublished.
- [3] *Climate Change - United Nations Sustainable Development*. [Online]. Available: <https://www.un.org/sustainabledevelopment/climate-change-2/> (visited on 04/01/2019).
- [4] "Wind energy in Europe in 2018", WindEurope, Tech. Rep., 2018.
- [5] *The Paris Agreement \_ UNFCCC*. [Online]. Available: <https://unfccc.int/process-and-meetings/the-paris-agreement/the-paris-agreement> (visited on 04/01/2019).
- [6] "Wind energy in Europe: Scenarios for 2030", WindEurope, Tech. Rep. September, 2017.
- [7] Clean Energy Wire, *German Offshore wind Power - output, business and perspectives*, 2018. [Online]. Available: <https://www.cleanenergywire>.

- 
- org/factsheets/german-offshore-wind-power-output-business-and-perspectives (visited on 04/23/2018).
- [8] —, *German onshore wind power – output, business and perspectives*, 2018. [Online]. Available: <https://www.cleanenergywire.org/factsheets/german-onshore-wind-power-output-business-and-perspectives> (visited on 04/23/2019).
- [9] M. J. Dvorak, C. L. Archer, and M. Z. Jacobson, “California offshore wind energy potential”, *Renewable Energy*, vol. 35, no. 6, pp. 1244–1254, 2010, ISSN: 09601481. DOI: 10.1016/j.renene.2009.11.022. [Online]. Available: <http://dx.doi.org/10.1016/j.renene.2009.11.022>.
- [10] AWEA, “American Wind Energy Association U.S. Wind Industry Fourth Quarter 2018 Market Report A product of AWEA Data Services”, 2019. [Online]. Available: [https://www.awea.org/getattachment/Resources/Publications-and-Reports/Market-Reports/2018-U-S-Wind-Industry-Market-Reports/4Q2018%7B%5C\\_%7Dpublic/U-S-Wind-Industry-third-Quarter-2018-Market-Report/4Q-2018-AWEA-Market-Report-Public-Version.pdf.aspx?lang=en-US](https://www.awea.org/getattachment/Resources/Publications-and-Reports/Market-Reports/2018-U-S-Wind-Industry-Market-Reports/4Q2018%7B%5C_%7Dpublic/U-S-Wind-Industry-third-Quarter-2018-Market-Report/4Q-2018-AWEA-Market-Report-Public-Version.pdf.aspx?lang=en-US).
- [11] Equinor, *Wind power in Japan*, Tokyo, 2019.
- [12] Linklaters, “Japan Offshore Wind : Approaching a Tipping Point”, no. October, pp. 0–26, 2018. [Online]. Available: <https://www.linklaters.com/ko-kr/insights/publications/2018/october/japan-offshore-wind>.
- [13] H. Björklund, “ABB review - Special report 60 years of HVDC”, *The corporate technical journal*, pp. 1–72, 2014.
- [14] *DNV GL supports creation of China’s first HVDC offshore wind substation - DNV GL*. [Online]. Available: <https://www.dnvgl.com/news/dnvgl-supports-creation-of-china-s-first-hvdc-offshore-wind-substation-127946> (visited on 04/02/2019).

- 
- [15] *AWS Truepower Dashboards*. [Online]. Available: <https://aws-dewi.ul.com/knowledge-center/maps/> (visited on 04/01/2019).
- [16] N. B. Negra, J. Todorovic, and T. Ackermann, "Loss evaluation of HVAC and HVDC transmission solutions for large offshore wind farms", vol. 76, pp. 916–927, 2006. DOI: 10.1016/j.epsr.2005.11.004.
- [17] S. Rodrigues, C. Restrepo, E. Kontos, R. T. Pinto, and P. Bauer, "Trends of offshore wind projects", *Renewable and Sustainable Energy Reviews*, vol. 49, pp. 1114–1135, 2015, ISSN: 1364-0321. DOI: 10.1016/j.rser.2015.04.092. [Online]. Available: <http://dx.doi.org/10.1016/j.rser.2015.04.092>.
- [18] N. Chong and R. Li, *Offshore Wind Farms Technologies, Design and Operation*. 2016.
- [19] "Offshore Wind in Europe", WindEurope, Tech. Rep., 2018.
- [20] "Status of Offshore Wind Energy Development in Germany Year 2018", Deutsche Windguad, Tech. Rep., 2018.
- [21] *Market trends -moving into deeper waters with bigger turbines*. [Online]. Available: <https://hub.globalccsinstitute.com/publications/deep-water-next-step-offshore-wind-energy/12-market-trends-moving-deeper-waters-bigger-turbines> (visited on 04/01/2019).
- [22] *China's first offshore HVDC line planned \_ Windpower Offshore*. [Online]. Available: <https://www.windpoweroffshore.com/article/1491354/chinas-first-offshore-hvdc-line-planned> (visited on 04/02/2019).
- [23] *HYDROCHINA HUADONG ENGINEERING CORPORATION LIMITED*. [Online]. Available: <http://www.ecidi.com/en/introduction.aspx> (visited on 04/02/2019).
- [24] E. Tedeschi, *Lecture notes in "Power Electronics in Future Power Systems*, 2018.
-

- 
- [25] X. Xiang, M. Merlin, and T. Green, "Cost Analysis and Comparison of HVAC, LFAC and HVDC for Offshore Wind Power Connection", no. August 2017, 6 (6 .)–6 (6 .) 2016. DOI: 10.1049/cp.2016.0386.
- [26] U. S. E. I. Administration, "Assessing HVDC Transmission for Impacts of Non - Dispatchable Generation", no. June, 2018.
- [27] L. P. Lazaridis, "Economic Comparison of HVAC and HVDC Solutions for Large Offshore Wind Farms under Special Consideration of Reliability", *Electrical Engineering*, vol. 12, no. 4, pp. 203–208, 2005, ISSN: 09340882. DOI: 10.1007/s004970050001.
- [28] ABB, *Offshore wind connections/dc-solutions*. [Online]. Available: <http://new.abb.com/systems/offshore-wind-connections/dc-solutions> (visited on 05/03/2018).
- [29] R. Adapa, *Using HVDC to Facilitate Offshore Wind Power Transmission*, 2018. [Online]. Available: [https://www.elp.com/articles/powergrid%7B%5C\\_%7Dinternational/print/volume-23/issue-4/features/turning-the-tide.html](https://www.elp.com/articles/powergrid%7B%5C_%7Dinternational/print/volume-23/issue-4/features/turning-the-tide.html) (visited on 04/02/2019).
- [30] The Regional Group North Sea for the NSCOGI (North Seas Countries' Offshore Grid Initiative), "Offshore Transmission Technology", p. 44, 2011. [Online]. Available: [https://www.entsoe.eu/fileadmin/user%7B%5C\\_%7Dupload/%7B%5C\\_%7Dlibrary/publications/entsoe/SDC/European%7B%5C\\_%7Doffshore%7B%5C\\_%7Dgrid%7B%5C\\_%7D-%7B%5C\\_%7Doffshore%7B%5C\\_%7DTechnology%7B%5C\\_%7D-%7B%5C\\_%7DFINALversion.pdf](https://www.entsoe.eu/fileadmin/user%7B%5C_%7Dupload/%7B%5C_%7Dlibrary/publications/entsoe/SDC/European%7B%5C_%7Doffshore%7B%5C_%7Dgrid%7B%5C_%7D-%7B%5C_%7Doffshore%7B%5C_%7DTechnology%7B%5C_%7D-%7B%5C_%7DFINALversion.pdf).
- [31] R. S. Geetha, R. Deekshit, and G. Lal, "Converter Topologies in VSC-HVDC Systems-an overview", vol. 3, no. 8, pp. 1380–1386, 2014.
- [32] H. A. Pereira, V. F. Mendes, L. Harnefors, and R. Teodorescu, "Comparison of 2L-VSC and MMC-based HVDC Converters: Grid Frequency Support Considering Reduced Wind Power Plants Models", *Electric Power Components and Systems*, vol. 45, no. 18, pp. 2007–2016, 2017, ISSN:

- 
15325016. DOI: 10.1080/15325008.2017.1378941. [Online]. Available: <https://doi.org/10.1080/15325008.2017.1378941>.
- [33] L. Xu, B. Andersen, P. Cartwright, and P. Horton, "Topologies for VSC transmission", *Power Engineering Journal*, vol. 16, no. 3, pp. 142–150, 2005, ISSN: 0950-3366. DOI: 10.1049/pe:20020307.
- [34] S. Meier, S. Norrga, and H. Nee, "New Voltage Source Converter Topology for HVDC Grid Connection of Offshore Wind Farms New Voltage Source Converter Topology for HVDC Grid Connection of Offshore Wind Farms", no. January, 2004.
- [35] K. L. Koo and Z. Emin, "Methodology for Modelling and Assessing Harmonic Impact of HVDC Connections in the Vicinity of Renewables",
- [36] ABB, "HVDC Light ® It's time to connect", *ABB ID No. POW-0038*, pp. 1–72, 2013.
- [37] *Troll electrification project - Case studies \_ ABB*. [Online]. Available: <https://new.abb.com/systems/hvdc/references/troll-a> (visited on 04/02/2019).
- [38] *Borwind*. [Online]. Available: <https://new.abb.com/systems/hvdc/references/borwin1> (visited on 04/02/2019).
- [39] Trans Bay Cable, "Introduction to The Trans Bay Cable Project", 2014.
- [40] D. C. Ludois and G. Venkataramanan, "Simplified terminal behavioral model for a modular multilevel converter", *IEEE Transactions on Power Electronics*, vol. 29, no. 4, pp. 1622–1631, 2014, ISSN: 08858993. DOI: 10.1109/TPEL.2013.2268856.
- [41] —, "Simplified dynamics and control of Modular Multilevel Converter based on a terminal behavioral model", *2012 IEEE Energy Conversion Congress and Exposition, ECCE 2012*, pp. 3520–3527, 2012. DOI: 10.1109/ECCE.2012.6342491.
- [42] H. Saad, S. Denetière, and J. Mahseredjian, "On modelling of MMC in EMT-type program", *2016 IEEE 17th Workshop on Control and Modeling*
-

- 
- for *Power Electronics, COMPEL 2016*, pp. 1–7, 2016. DOI: 10.1109/COMPEL.2016.7556717.
- [43] G. Bergna-Diaz, J. A. Suul, and S. D’Arco, “Energy-Based State-Space Representation of Modular Multilevel Converters with a Constant Equilibrium Point in Steady-State Operation”, *IEEE Transactions on Power Electronics*, vol. 33, no. 6, pp. 4832–4851, 2018, ISSN: 08858993. DOI: 10.1109/TPEL.2017.2727496.
- [44] G. Bergna Diaz, J. A. Suul, and S. D’Arco, “Small-signal state-space modeling of modular multilevel converters for system stability analysis”, *2015 IEEE Energy Conversion Congress and Exposition, ECCE 2015*, pp. 5822–5829, 2015. DOI: 10.1109/ECCE.2015.7310477.
- [45] J. Freytes, G. Bergna, J. Are Suul, S. D’Arco, H. Saad, and X. Guillaud, “State-space modelling with steady-state time invariant representation of energy based controllers for modular multilevel converters”, *2017 IEEE Manchester PowerTech, Powertech 2017*, vol. 2, no. 2, pp. 1–7, 2017. DOI: 10.1109/PTC.2017.7981011.
- [46] G. Bergna, J. A. Suul, and S. D’Arco, “Impact on small-signal dynamics of using circulating currents instead of AC-currents to control the DC voltage in MMC HVDC terminals”, in *ECCE 2016 - IEEE Energy Conversion Congress and Exposition, Proceedings*, IEEE, 2016, pp. 1–8, ISBN: 9781509007370. DOI: 10.1109/ECCE.2016.7855182.
- [47] S. D’Arco, X. Guillaud, F. Gruson, G. Bergna, H. Saad, J. Freytes, F. Colas, and J. A. Suul, “Improving Small-Signal Stability of an MMC With CCSC by Control of the Internally Stored Energy”, *IEEE Transactions on Power Delivery*, vol. 33, no. 1, pp. 429–439, 2017, ISSN: 0885-8977. DOI: 10.1109/tpwrd.2017.2725579.
- [48] L. Huang, X. Yang, P. Xu, F. Zhang, X. Ma, T. Liu, X. Hao, and W. Liu, “The evolution and variation of sub-module topologies with DC-fault current clearing capability in MMC-HVDC”, *2017 IEEE 3rd International Fu-*

- 
- ture Energy Electronics Conference and ECCE Asia, IFEEC - ECCE Asia 2017*, pp. 1938–1943, 2017. DOI: 10.1109/IFEEC.2017.7992346.
- [49] Z. Bai, H. Xia, H. Ma, and J. Wang, “MMC Capacitor Voltage Balancing Strategy Based on Carrier Rotation”, *Proceedings - 2018 IEEE International Power Electronics and Application Conference and Exposition, PEAC 2018*, no. 1, pp. 1–5, 2018. DOI: 10.1109/PEAC.2018.8590333.
- [50] H. Zhang, D. Jovcic, W. Lin, and A. J. Far, “Average value MMC model with accurate blocked state and cell charging/discharging dynamics”, *4th International Symposium on Environment Friendly Energies and Applications, EFEA 2016*, pp. 1–6, 2016. DOI: 10.1109/EFEA.2016.7748768.
- [51] S. Sanchez, G. Bergna, and E. Tedeschi, “Tuning of control loops for grid-connected Modular Multilevel Converters under a simplified port representation for large system studies”, *2017 12th International Conference on Ecological Vehicles and Renewable Energies, EVER 2017*, no. November, 2017. DOI: 10.1109/EVER.2017.7935913.
- [52] A. A. Taffese, E. Tedeschi, and E. De Jong, “A control scheme for utilizing energy storage of the modular multilevel converter for power oscillation damping”, *2017 IEEE 18th Workshop on Control and Modeling for Power Electronics, COMPEL 2017*, 2017. DOI: 10.1109/COMPEL.2017.8013415.
- [53] A. A. Taffese, A. G. Endegnanew, S. Sanchez, and E. Tedeschi, “Reducing Rapid Wind Farm Power Fluctuations Using the Modular Multilevel Converter Table of Contents”, 2019.
- [54] A. E. Leon, “Short-Term Frequency Regulation and Inertia Emulation Using an MMC-Based MTDC System”, *IEEE Transactions on Power Systems*, vol. 33, no. 3, pp. 2854–2863, 2018. DOI: 10.1109/TPWRS.2017.2757258.
- [55] J. Freytes, S. Akkari, P. Rault, M. M. Belhaouane, and X. Guillaud, “Dynamic Analysis of MMC-Based MTDC Grids : Use of MMC Energy to Im-
-

- 
- prove Voltage Behavior”, *IEEE Transactions on Power Delivery*, vol. 34, no. 1, pp. 137–148, 2019. DOI: 10.1109/TPWRD.2018.2868878.
- [56] I. Puranik, L. Zhang, S. Member, J. Qin, S. Member, A. D. Polarization, and C. Model, “Impact of Low-Frequency Ripple on Lifetime of Battery in MMC-based Battery Storage Systems”, pp. 2748–2752, 2018.
- [57] A. B. Ch, “Modular Multilevel Converter based Hybrid Energy Storage System”, 2017.
- [58] *EUR-Lex - 32016R0631 - EN - EUR-Lex*. [Online]. Available: <https://eur-lex.europa.eu/legal-content/EN/TXT/?uri=CELEX%7B%5C%7D3A32016R0631> (visited on 05/23/2019).
- [59] M. Saqid and A. Saleem, *Power-quality issues and the need for reactive-power compensation in the grid integration of wind powe.* (visited on 01/23/2019).
- [60] *Skype conversation with Dr. Yongtao Yang, DNV GL*, 2018.
- [61] OSMC, *OpenModelica*, 2019. [Online]. Available: <https://openmodelica.org/> (visited on 04/24/2019).
- [62] MathWorksStore, *New Annual License for MATLAB R2019a*, 2019. [Online]. Available: <https://se.mathworks.com/store/link/products/standard/annual/ML> (visited on 04/24/2019).
- [63] MathWorks, *Pricing and Licensing*, 2019. [Online]. Available: <https://uk.mathworks.com/pricing-licensing.html?prodcode=ML%7B%5C%7Dintendeduse=undefined>.
- [64] *ModelicaDEVs*. [Online]. Available: <https://build.openmodelica.org/Documentation/ModelicaDEVs.UsersGuide.Introduction.html> (visited on ).
- [65] *ModelicaDEVs*. [Online]. Available: <https://build.openmodelica.org/Documentation/ModelicaDEVs.UsersGuide.QSS.html> (visited on ).

- 
- [66] *ModelicaDEVS*. [Online]. Available: <https://build.openmodelica.org/Documentation/ModelicaDEVS.UsersGuide.DEVSformalism.html> (visited on ).
- [67] J. Bélanger, P. Venne, and S. Member, “The What , Where and Why of Real-Time Simulation”, pp. 37–49,
- [68] J. Espvik, “Modeling of Multiterminal HVDC grids with Renewable Energy and Storage Integration by Opensource Tools for HIL Applications”, Master, NTNU.
- [69] R. Wachal, M. Ba, P. Le-huy, and A. Mo, *HVDC Converters in a HVDC Grid*, December. 2014, ISBN: 9782858733057.
- [70] C. Wang, D. Xu, F. He, Q. Mu, X. Zhang, and H. Peng, “Capacitor Voltage Balancing Control Algorithm for Modular Multilevel Converter Based on the Dynamic Tiered Sorting”, *2018 International Conference on Power System Technology (POWERCON)*, no. 201804270000890, pp. 2752–2757, 2019. DOI: 10.1109/powercon.2018.8602306.
- [71] Lin Wang, Ping Wang, Zixin Li, and Yaohua Li, “A novel capacitor voltage balancing control strategy for modular multilevel converters (MMC)”, *2013 International Conference on Electrical Machines and Systems (ICEMS)*, no. Mmc, pp. 1804–1807, 2014. DOI: 10.1109/icems.2013.6713283.
- [72] X. Zhang, Y. Zhang, Y. Xu, M. Guo, and X. Kang, “An Optimization Algorithm of Capacitor Voltage Balancing in Modular Multilevel Converter”, *2018 International Conference on Power System Technology (POWERCON)*, no. 201804270000303, pp. 2533–2537, 2019. DOI: 10.1109/powercon.2018.8602343.
- [73] S. Rohner, J. Weber, and S. Bernet, “Continuous model of modular multilevel converter with experimental verification”, *IEEE Energy Conversion Congress and Exposition: Energy Conversion Innovation for a Clean Energy Future, ECCE 2011, Proceedings*, pp. 4021–4028, 2011. DOI: 10.1109/ECCE.2011.6064316.
-

- 
- [74] H.-P. Nee, L. Angquist, A. Antonopoulos, S. Norrga, and L. Harnefors, "Dynamic Analysis of Modular Multilevel Converters", *IEEE Transactions on Industrial Electronics*, vol. 60, no. 7, pp. 2526–2537, 2012, ISSN: 0278-0046. DOI: 10.1109/tie.2012.2194974.
- [75] A. Antonopoulos, L. Angquist, and H. P. Nee, "On dynamics and voltage control of the Modular Multilevel Converter", *Power Electronics and Applications, 2009. EPE '09. 13th European Conference on*, pp. 1–10, 2009.
- [76] H. Saad, S. Denetiere, J. Mahseredjian, P. Delarue, X. Guillaud, J. Peralta, and S. Nguéfeu, "Modular multilevel converter models for electromagnetic transients", *IEEE Transactions on Power Delivery*, vol. 29, no. 3, pp. 1481–1489, 2014, ISSN: 08858977. DOI: 10.1109/TPWRD.2013.2285633.
- [77] M.-b. H. T. Systems, V. Sood, X. Wang, J. Cano, and A. Mehrizi-sani, "Dynamic Averaged and Simplified Models for", vol. 28, no. 3, pp. 1723–1730, 2013. DOI: 10.1109/TPWRD.2013.2251912.
- [78] J. Peralta, H. Saad, S. Denetiere, and J. Mahseredjian, "Dynamic performance of average-value models for multi-terminal VSC-HVDC systems", *IEEE Power and Energy Society General Meeting*, pp. 1–8, 2012, ISSN: 19449925. DOI: 10.1109/PESGM.2012.6345610.
- [79] J. Xu, A. M. Gole, and C. Zhao, "The Use of Averaged-Value Model of Modular Multilevel Converter in DC Grid", *IEEE Transactions on Power Delivery*, vol. 30, no. 2, pp. 519–528, 2015, ISSN: 08858977. DOI: 10.1109/TPWRD.2014.2332557.
- [80] A. Beddard, M. Barnes, and R. Preece, "Comparison of Detailed Modeling Techniques for MMC Employed on VSC-HVDC Schemes", *IEEE Transactions on Power Delivery*, vol. 30, no. 2, pp. 579–589, 2015, ISSN: 08858977. DOI: 10.1109/TPWRD.2014.2325065.
- [81] N. R. Chaudhuri, R. Oliveira, and A. Yazdani, "Stability Analysis of Vector-Controlled Modular Multilevel Converters in Linear Time-Periodic Frame-

- 
- work”, *IEEE Transactions on Power Electronics*, vol. 31, no. 7, pp. 5255–5269, 2016, ISSN: 08858993. DOI: 10.1109/TPEL.2015.2480845.
- [82] S. R. Deore, P. B. Darji, and A. M. Kulkarni, “Dynamic phasor modeling of Modular Multi-level Converters”, *2012 IEEE 7th International Conference on Industrial and Information Systems, ICIIS 2012*, pp. 1–6, 2012. DOI: 10.1109/ICIInfS.2012.6304792.
- [83] N. T. Trinh, M. Zeller, K. Wuerflinger, and I. Erlich, “Generic Model of MMC-VSC-HVDC for Interaction Study with AC Power System”, *IEEE Transactions on Power Systems*, vol. 31, no. 1, pp. 27–34, 2016, ISSN: 08858950. DOI: 10.1109/TPWRS.2015.2390416.
- [84] T. Li, A. M. Gole, and C. Zhao, “Harmonic Instability in MMC-HVDC Converters Resulting from Internal Dynamics”, *IEEE Transactions on Power Delivery*, vol. 31, no. 4, pp. 1738–1747, 2016, ISSN: 08858977. DOI: 10.1109/TPWRD.2016.2542188.
- [85] G. Bergna and J. A. Suul, “State-Space Modelling of Modular Multilevel Converters for Constant Variables in Steady-State”, *2016 IEEE 17th Workshop on Control and Modeling for Power Electronics (COMPEL)*, pp. 1–9, 2016. DOI: 10.1109/COMPEL.2016.7556695.
- [86] S. Liu, Z. Xu, W. Hua, G. Tang, and Y. Xue, “Electromechanical transient modeling of modular multilevel converter based multi-terminal hvdc systems”, *IEEE Transactions on Power Systems*, vol. 29, no. 1, pp. 72–83, 2014, ISSN: 08858950. DOI: 10.1109/TPWRS.2013.2278402.
- [87] A. A. J. Far and D. Jovcic, “Circulating current suppression control dynamics and impact on MMC converter dynamics”, *2015 IEEE Eindhoven PowerTech, PowerTech 2015*, pp. 1–6, 2015. DOI: 10.1109/PTC.2015.7232762.
- [88] X. Yang, J. Li, X. Wang, W. Fan, and T. Q. Zheng, “Circulating current model of modular multilevel converter”, *Asia-Pacific Power and Energy*
-

- 
- Engineering Conference, APPEEC*, no. 141091522, pp. 1–6, 2011, ISSN: 21574839. DOI: 10.1109/APPEEC.2011.5749067.
- [89] D. Siemaszko, L. Angquist, A. Antonopoulos, H.-p. Nee, M. Vasiladiotis, and K. Ilves, “Open-Loop Control of Modular Multilevel Converters Using Estimation of Stored Energy”, *IEEE Transactions on Industry Applications*, vol. 47, no. 6, pp. 2516–2524, 2011, ISSN: 0093-9994. DOI: 10.1109/tia.2011.2168593.
- [90] J. Beerten, G. B. Diaz, and S. D. Arco, “Comparison of Small-Signal Dynamics in MMC and Two-Level VSC HVDC Transmission Schemes”, *2016 IEEE International Energy Conference (ENERGYCON)*, pp. 1–6, DOI: 10.1109/ENERGYCON.2016.7514048.
- [91] G. Bergna, J. A. Suul, E. Berne, J. C. Vannier, and M. Molinas, “MMC circulating current reference calculation in ABC frame by means of Lagrange Multipliers for ensuring constant DC power under unbalanced grid conditions”, *2014 16th European Conference on Power Electronics and Applications, EPE-ECCE Europe 2014*, pp. 1–10, 2014. DOI: 10.1109/EPE.2014.6910909.
- [92] N. Ahmed, L. Ångquist, D. Van Hertem, J. Beerten, W. Leterme, and S. Norrga, “A new HVDC grid test system for HVDC grid dynamics and protection studies in EMT-type software”, 095 (7.)–095 (7.) 2015. DOI: 10.1049/cp.2015.0068.
- [93] M. Barnes and A. Beddard, “Voltage Source Converter HVDC Links – The state of the Art and Issues Going Forward”, vol. 24, no. January, pp. 108–122, 2012, ISSN: 1876-6102. DOI: 10.1016/j.egypro.2012.06.092. [Online]. Available: <http://dx.doi.org/10.1016/j.egypro.2012.06.092>.
- [94] I. Pizetta, A. S. Brandao, and M. Sarcinelli-filho, “Symmetrical Optimum Based PI Control Redesign”, *Anais do XX Congresso Brasileiro de Automática*, pp. 1466–1473, 2014.

- 
- [95] P. Sourdille, A. O. Dwyer, P. Sourdille, and A. O. Dwyer, "Determination of the phase of a transfer function : theory versus practice Determination of the phase of a transfer function : Theory versus Practice", 2004.
- [96] J. A. Suul, J. Beerten, and S. D'Arco, "Frequency-dependent cable modelling for small-signal stability analysis of VSC-HVDC systems", *IET Generation, Transmission & Distribution*, vol. 10, no. 6, pp. 1370–1381, 2016, ISSN: 1751-8687. DOI: 10.1049/iet-gtd.2015.0868.
- [97] *Expansions for Small Quantities*. [Online]. Available: <https://www.astro.umd.edu/~7B~7Dmiller/teaching/astr498d/expansions.pdf>.
- [98] J. A. Martinez-Velasco, *Power System Transients: Parameter Determination*. 2010, pp. 137–175, ISBN: 9781420065299.
- [99] J. Beerten, S. D. Arco, and J. A. Suul, "Cable Model Order Reduction for HVDC Systems Interoperability Analysis", pp. 1–10,
- [100] B. Gustavsen and A. Semlyen, "Vector\_Fitting.Pdf", *IEEE Trans. Power Delivery*, vol14, no.3, pp., pp. 1052–1061, 1999.
- [101] T. Brekken, *Design og drift av Smart Grid kraftsystemer*, Trondheim, 2018.
- [102] W. Turbines and S. Edition, *for Design of Wind Turbines*, ISBN: 8755028705.
- [103] J. Zhang, M. Cheng, Z. Chen, and X. Fu, "Pitch Angle Control for Variable Speed Wind Turbines", no. April, pp. 2691–2696, 2008.
- [104] E. V. Tranulis, "Modelling of the Voltage Source Converter in OpenModelica", NTNU, Trondheim, Tech. Rep., 2018.
- [105] C. Bajracharya, "Control of VSC-HVDC for wind power", no. June, 2008.
- [106] Controllab, *What is HIL Testing?*, 2015. [Online]. Available: <http://www.hil-simulation.com/home/hil-testing.html>.
- [107] D. Winkler and C. Gühmann, "Hardware-in-the-Loop simulation of a hybrid electric vehicle using Modelica/Dymola", *22nd International Battery, Hybrid and Fuel Cell Electric Vehicle Symposium*, no. May 2014, pp. 1054–1063, 2006. [Online]. Available: <http://citeseerx.ist.psu.edu/>

---

viewdoc/download?doi=10.1.1.404.7637%7B%5C%7Drep= repl%7B%5C%7Ddtype=pdf%7B%5C%7D0Ahttp://mathpros.com/papers/hybrid/Hardware%7B%5C%7Din%7B%5C%7Dthe%7B%5C%7DLoop%7B%5C%7DSimulation%7B%5C%7Dof%7B%5C%7Da%7B%5C%7DHybrid%7B%5C%7DElectric%7B%5C%7DVehicle%7B%5C%7Dusing%7B%5C%7DModelica%7B%5C%7Dand%7B%5C%7DDymola.pdf.

- [108] C. Dufour, S. Abourida, and J. Baalanger, "InfiniBand-based real-time simulation of HVDC, STATCOM and SVC devices with Custom-Of-The-Shelf PCs and FPGAs", *IEEE International Symposium on Industrial Electronics*, vol. 3, no. December, pp. 2025–2029, 2006. DOI: 10.1109/ISIE.2006.295884.
- [109] OpalRT, *OPAL-RT how-to video and quick start guide links (updated Feb 2019)*, 2019. [Online]. Available: [http://www.ecadtools.com.au/documents-opal/OPAL-RT%20how-to%20video%20and%20quick%20start%20guide%20links%20\(updated%20Feb%202019\).pdf](http://www.ecadtools.com.au/documents-opal/OPAL-RT%20how-to%20video%20and%20quick%20start%20guide%20links%20(updated%20Feb%202019).pdf).
- [110] O. TECHNOLOGIES, *EMS SCADA Electromechanical real-time simulation*. [Online]. Available: <https://www.opal-rt.com/systems-ephasorsim/> (visited on 04/26/2019).
- [111] OPAL-RT, *OP5700 User Manual*, 2006. DOI:10.1007/SpringerReference\_28001. arXiv: arXiv:1011.1669v3.
- [112] P. Kundur, *Power System Stability and Control.pdf*, 1994.
- [113] [Online]. Available: <https://fmi-standard.org/tools/>.
- [114] Mathworks, *UUID Generation - File Exchange - MATLAB Central*. [Online]. Available: <https://se.mathworks.com/matlabcentral/fileexchange/21709-uuid-generation> (visited on 04/26/2019).
- [115] OpalRT, *Subsystem Division*. [Online]. Available: <https://www.opal-rt.com/opal%7B%5C%7Dtutorial/preparing-simulink-model-real-time-execution/>.

- 
- [116] *Implement insulated gate bipolar transistor (IGBT) - Simulink - MathWorks Nordic*. [Online]. Available: <https://se.mathworks.com/help/physmod/sps/powersys/ref/igbt.html> (visited on 05/23/2019).
- [117] *Implements ideal IGBT, GTO, or MOSFET and antiparallel diode - Simulink - MathWorks Nordic*.
- [118] *Why you should never break a continuous algebraic loop with a Memory block - MATLAB & Simulink*.
- [119] M. Sjölund, *Tools and Methods for Analysis, Debugging, and Performance Improvement of Equation-Based Models*, September. 2015, ISBN: 9789175190716. DOI: 10.3384/diss.diva-116346.
- [120] W. Braun, F. Casella, and B. Bachmann, "Solving Large-scale Modelica Models : New Approaches and Experimental Results using OpenModelica", 2017. DOI: 10.3384/ecp17132557.
- [121] W. Braun, L. Ochel, and B. Bachmann, "Symbolically Derived Jacobians Using Automatic Differentiation- Symbolically Derived Jacobians Using Automatic Differentiation - Enhancement of the OpenModelica Compiler", no. June, 2011. DOI: 10.3384/ecp11063495.
- [122] D. Ab and M. Otter, "METHODS FOR TEARING SYSTEMS OF EQUATIONS IN OBJECT-ORIENTED MODELING Hilding Elmqvist", vol. 2, no. Mah, 1990.
- [123] L. R. Petzold, "A description of DASSL: a differential / algebraic system solver", *Proceedings of the 10th IMACS World Congress on System Simulation and Scientific Computation*, no. January 1982, pp. 3–7, 1982.
- [124] D. Germund, "A special stability problem for linear multistep methods", *Springer Link*, 1963.
- [125] B. Liu, K. Uhlen, and T. Undeland, "Temporary Rotor Inertial Control of Wind Turbine to Support the Grid Frequency Regulation", no. January, 2012.
- [126] *Wind energy frequently asked questions (FAQ) \_ EWEA*.

- 
- [127] K. Ilves, S. Norrga, L. Harnefors, and H. P. Nee, "On energy storage requirements in modular multilevel converters", *IEEE Transactions on Power Electronics*, vol. 29, no. 1, pp. 77–88, 2014, ISSN: 08858993. DOI: 10.1109/TPEL.2013.2254129.
- [128] I. Kalle, *Modeling and Design of Modular Multilevel Converters for Grid Applications*. 2014, p. 55, ISBN: 9789175015804. [Online]. Available: <https://www.diva-portal.org/smash/get/diva2:753599/FULLTEXT01.pdf>.
- [129] P. Roper, "600kV 1", no. December 2017, pp. 1–8, 2018.
- [130] *North Sea Link - North Sea Link*. [Online]. Available: [northsealink.com](http://northsealink.com) (visited on 05/09/2019).
- [131] Y. Li, "Arm Inductance and Sub-module Capacitance Selection in Modular Multilevel Converter", 2013.
- [132] *Conversation with Prof. Elisabetta Tedeschi*, Trondheim, 2019.
- [133] C. Paper, J. W. Kolar, and M. L. Heldwein, "PWM Converter Power Density Barriers", no. February 2014, 2007. DOI: 10.1109/PCCON.2007.372914.

# Appendices



Appendix **A**

Paper for OSES2019 conference

# Modeling of Multiterminal HVDC Offshore Grids with Renewable Energy and Storage Integration by Opensource Tools

Joachim Espvik  
*Department of Electric  
Power Engineering,  
Norwegian University of  
Science and Technology*  
Trondheim, Norway  
joachim\_espvik@hotmail.com

Erling Vatn Tranulis  
*Department of Electric  
Power Engineering,  
Norwegian University of  
Science and Technology*  
Trondheim, Norway  
erling.v.t@gmail.com

Elisabetta Tedeschi  
*Department of Electric  
Power Engineering,  
Norwegian University of  
Science and Technology*  
Trondheim, Norway  
elisabetta.tedeschi@ntnu.no

Santiago Sanchez Acevedo  
*Energy Systems  
SINTEF Energy Research*  
Trondheim, Norway  
santiago.sanchez@sintef.no

**Abstract**—With increasing offshore wind penetration levels, more secure and flexible offshore electrical transmission systems are needed to ensure security of supply to onshore users. When considering long distances of electrical power transmission, HVDC grids based on the modular multilevel converter (MMC) are a solution for present and future large scale offshore wind integration. As HVDC grids are developing into large and complex systems, dynamic analysis of the systems is useful to gain knowledge on the interactions between the different components in the grids. This paper uses the open source tool OpenModelica as modeling environment to demonstrate the potential of the tool in modeling such HVDC systems. A three-terminal HVDC system with offshore wind and energy storage integration is implemented in OpenModelica, and the dynamics of the system are investigated through four simulation cases. The main focus of this paper is dynamics and operation related to the HVDC system. The simulation results show that the MMCs can improve the most rapid power fluctuations using its internal storage capabilities, while an external energy storage system provides a more constant power flow over more extensive periods, in addition to improving the operation of the HVDC system. All models used in this paper are made publicly available to anyone for any purpose, including future studies of larger HVDC grids.

**Index Terms**—Offshore wind power, Energy storage system, Multiterminal HVDC, MMC, Open source, OpenModelica, Dynamic modeling, Transient simulations

## I. INTRODUCTION

Over the last 10 years, the installed capacity of offshore wind power has dramatically increased from 1 to 18 GW in Europe [1]. Furthermore, projections of future installation levels coupled with economic considerations and maritime spatial planning predict increasing distances to shore of future offshore wind farms [2], [3]. When transporting electrical energy in submarine cables over such long distances, economic and technical considerations make high-voltage direct current (HVDC) the preferred choice for electrical power transmission [4].

This work was partly funded by the Norwegian Research Council and DNV-GL through the NFR contract n. 250493 - within the Integrated approach to the Design and Control of Offshore HVDC Networks (IDeCON) project.

As the number of wind farms with HVDC connections to shore increases, the power system also becomes increasingly dependent on secure power supply through these HVDC connections. To ensure security of supply from these wind farms, it is useful to connect the HVDC terminals in an offshore HVDC grid [5]. This increases the flexibility of the system, as power flows in HVDC grids can be rerouted through different paths to shore. This allows power transfer from the wind farms to shore even if one of the HVDC connections is out of operation, thus, increasing the reliability of the system.

In such HVDC grids, the modular multilevel converter (MMC) is becoming the preferred power electronic converter for converting between AC and DC due to its many benefits [6]. The MMC is capable of reversing the power flow without reversing the polarity of the DC voltages by DC current reversal. Additionally, features like modularity and scalability make the MMC advantageous compared to other voltage source converter (VSC) topologies. The MMC also has an inherent capability of storing energy internally in the converter [7], which can benefit the system in which it is connected.

Another crucial aspect for offshore wind power integration is the varying power production due to the intermittency in wind speed. The varying power production from wind farms can be classified into three categories [8]. The first being the most rapid variations due to, e.g., wind gusts on the time scale of seconds. The second variation is short-term variations on the scale of minutes to hours while the third and last variation is seasonal variations. To meet this challenge, an energy storage system can be integrated into the HVDC grid to complement the power production from the offshore wind farms and further improve the overall system.

However, because HVDC grids are developing into large and complex systems with many different components, it is useful to test the system to gain knowledge on the interactions between the various components. When investigating the dynamics and testing the controllers of such large systems, it is not directly feasible to run tests on full-scale systems.

Therefore, hardware-in-the-loop (HIL) testing is often used to test HVDC grids in laboratory environments [9]. HIL combines software based simulation models that replicate the behavior of the physical components with actual physical components.

The Modelica modeling language is a tool especially used in the automobile industry for HIL testing [10], [11]. An emerging tool based on the Modelica language is OpenModelica, which is open-source and allows integration of models developed in different physical domains. Additionally, OpenModelica supports the Functional Mock-up Interface (FMI) standard that allows models developed in OpenModelica to be shared across multiple platforms and tools, and be used in, e.g., HIL testing. This makes the modeling of an HVDC grid in OpenModelica a timely investigation area, including possibilities for laboratory testing and verification.

In this paper, a model of a three-terminal HVDC grid with offshore wind and energy storage integration, including MMCs, HVDC cables, wind farms, and an energy storage system, is analyzed and implemented in OpenModelica. The topic of energy storage integration in the HVDC grid is investigated using simulations of the system to demonstrate the potential of the open source tool in such analyses. Additionally, the internal storage capabilities of the MMC are studied to investigate how the MMC can contribute to the HVDC grid support compared to an external offshore energy storage system.

As an additional contribution to the knowledge community, all models introduced in the paper are made publicly available to anyone for any purpose through the following URL: <https://github.com/joachimesp/OpenModelica-HVDC-NTNU>. Additionally, an MMC model and a point-to-point HVDC model built for Opal-RTs real-time simulator, ePHASORSIM, are added to the folder for illustration purposes on how to build models for the real-time simulator. This allows models to be used in future laboratory experiments with HIL testing.

Further details of the models developed and test cases presented hereafter can be found in [12], [13].

The remainder of the paper is organized as follows: Section II introduces the OpenModelica software with the description of a preliminary assessment of its performance. Next, Section III describes the three-terminal HVDC system with all models used to build the system. Section IV introduces the different simulation cases, their purpose, and results. Section V includes a discussion and Section VI concludes.

## II. THE OPENMODELICA SOFTWARE

The Modelica modeling language is a vendor-independent standard, thus there exists multiple implementations of modeling tools using the modeling language, such as Dymola, MathModelica and IDA. However, these implementations are not open source, which makes OpenModelica an emerging tool.

One of the features used in this paper was the use of electrical components in the built-in standard library of OpenModelica. This reflects the acausal modeling approach in the

software, meaning dynamics of an electrical circuit can be modeled by drawing the circuit with circuit components and not with generic blocks as in causal modeling.

Preliminary tests were carried out to verify that OpenModelica is able to capture high frequency dynamics in the range of several kilohertz. This was done by building two 10kHz 2L-VSC models, one in OpenModelica and one in MATLAB Simulink to compare their results. The tests showed that the captured dynamics of the two models were very similar [12], [13]. Since such dynamics are of significantly higher frequency than the simulations in this paper, it was assumed that OpenModelica could accurately capture all dynamics of interest.

## III. SIMULATION SYSTEM DESCRIPTION

The final goal of this paper is to investigate the dynamics of the system in fig. 1 by implementing it in OpenModelica. The topology is chosen because it is the system with the lowest complexity that allows studying the interactions between the key components in an HVDC grid, including an energy storage system.

The system in fig. 1 includes two wind farms, WF1 and WF2, three HVDC MMC converters connected by two HVDC cables and an energy storage system (ESS) connected near WF2.

WF1 consists of 70 turbines with a rated power of 7MW each, while WF2 consists of 60 turbines with a rated power of 7MW each. Both cables are of 100km length. The rated values of the energy storage will be dimensioned in simulation case 2 later in the paper. A table with all the key parameters used in the different models is included in the Appendix. For further details on the controller parameters used in this paper, the reader can refer to the appendices in [12], [13].

The models used for each component are presented in this section.

### A. Energy-based MMC model

As explained in the introduction, the MMC is one of the key components in an HVDC grid, and it is used for converting between AC and DC in the grid. Figure 2 shows a schematic of the circuit of the MMC that is built of multiple submodules.

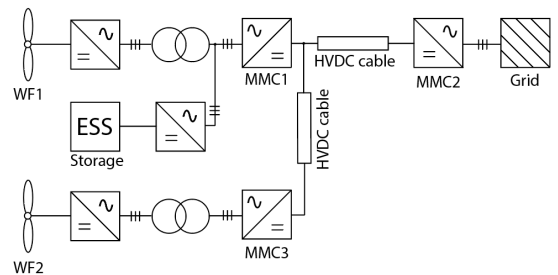


Fig. 1. Three-terminal HVDC system with offshore wind and storage integration under analysis.

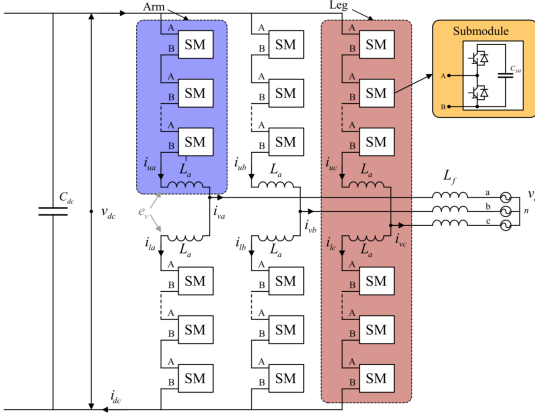


Fig. 2. A schematic of the MMC from [15].

Each submodule is, in this case, a half bridge with two IGBTs and a capacitor. Additionally, the MMC consists of an arm inductor for each arm,  $L_a$ , and an inductor on each phase of the AC-side,  $L_f$ . The MMC is operated such that the voltage of each submodule is inserted at the output voltage in steps, resulting in a waveform close to a sine on the AC-side,  $e_v$ . The output voltage waveform is generated with respect to the grid voltage, represented by voltage sources in the schematic, to produce a flow of active and reactive power across the grid side inductors.

In [14], a comparison of all available MMC models in the literature with varying level of complexity was done, and the conclusion led to a recommendation for using average value models for network-level studies. Average models are more computationally efficient compared to the more complex models, and they can reproduce the dynamics of the MMC accurately without detailed modeling of the internal structure of the MMC. Average models represent the MMC through controllable voltage and current sources on the AC and DC side, effectively meaning that effects of the pulse width modulation within the converter are averaged out over the switching period.

Furthermore, in this paper, the contribution of the internally stored energy in the MMC is studied. Therefore, an energy-based MMC model that includes the dynamics of the internally stored energy in the MMC was chosen.

When deciding on the how to model the MMC, it was desirable that the model should have steady state time invariant (SSTI) states. SSTI states facilitate linearized state space representations for eigenvalue analysis. Although this feature was not directly utilized in this work, it still makes the model more attractive for members of the industry and researchers wishing to make use of such techniques for stability analysis or tuning purposes. Furthermore, this makes control of the model easier.

Hence, the simplified zero-sequence MMC model from [15]

was chosen. The model couples states that oscillate at the same frequency in equation sets, which are subsequently transformed into a synchronous rotating reference frame (SRF). It is assumed that the modulation indices are calculated in a manner which compensates for the oscillations in the circulating voltage, referred to as "compensated modulation" [15]. This modeling approach is of great utility when deriving energy-based MMC models that provide great insight into the energy dynamics they introduce [16].

### B. The energy-based model schematic

Figure 3 shows the overview of the circuit implementation of the model as well as the associated control schemes.

The AC-side of the MMC is represented by a stiff grid voltage,  $v_g^{abc}$ , equivalent AC resistances,  $R_{eq} = R_f + \frac{1}{2}R_a$ , and inductances,  $L_{eq} = L_f + \frac{1}{2}L_a$ , as well as a controlled voltage source,  $e_v^{abc}$ , representing the voltage driving the AC-side currents,  $i_v^{abc}$ . The currents on the AC-side are controlled by an inner vector control of the transformed dq-currents [17]. The reference for the d-current comes from the outer power controller with DC voltage droop based on the measured power,  $P_{dc}$ , and voltage,  $V_{dc}$ . Droop control allows multiple MMCs in the grid to contribute to the DC voltage regulation. In this study, only the active power of the converter was of interest, and therefore, the reference for the q-current, controlling reactive power, was set to zero for all simulations executed in this paper.

The AC- and DC-sides are coupled using an energy balance equation, which accounts for the internal energy storage capability of the MMC, by modeling the zero-sequence energy sum,  $w_{\Sigma,z}$  based on the equivalent arm capacitance,  $C_{eq}$ . This energy is controlled using a zero-sequence energy sum controller, including a controller for the circulating current,  $i_{cz}$ .

The DC-side is modeled using a controllable voltage source for the circulating voltage,  $v_{c,z}$ , as well as equivalent arm resistances,  $\frac{2}{3}R_a$ , and inductances  $\frac{2}{3}L_a$ , and a DC-side capacitor,  $C_{dc}$ . The current source in fig. 3 represents, e.g., the DC current from another MMC in a point-to-point HVDC connection.

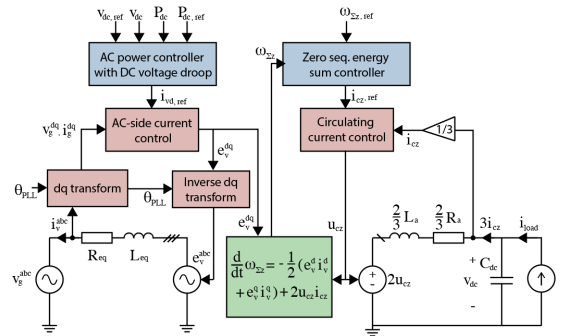


Fig. 3. Overview of the MMC model.

### C. Wind farm model

The wind farm model is represented in aggregated form based on the dynamics of a single wind turbine, assuming all turbines are operated equally. Figure 4 shows a schematic including the variables used in the turbine model.

The basis for the model is the dynamic equation for torque balance between the turbine blades,  $T_{wind}$ , the electrical generator,  $T_{gen}$ , the frictional torque,  $B\omega$ , and the torque associated with the acceleration of the turbine and generator  $J\frac{d}{dt}\omega$  which can be expressed as follows:

$$J\frac{d}{dt}\omega = T_{wind} - T_{gen} - B\omega \quad (1)$$

where  $J$  is the total inertia in turbine and the generator and  $\omega$  is the rotational speed of the turbine.

The turbine mechanical power,  $P_{turbine}$ , can be expressed by the turbine torque,  $T_{wind}$ , as

$$P_{turbine} = \omega T_{wind} \quad (2)$$

Alternatively, the turbine power can be expressed as a fraction of the power available in the wind through the power coefficient  $C_p$ .

$$P_{turbine} = C_p P_{wind} = C_p \frac{1}{2} \rho A u^3 \quad (3)$$

where  $\rho$  is the air density,  $A$  is the area swept by the blades and  $u$  is the wind speed.

When considering the aerodynamics of the turbine blades, it is useful to define the tip speed ratio  $\lambda$  as:

$$\lambda = \frac{\omega \ell}{u} \quad (4)$$

where  $\ell$  is the length of the turbine blades.

The power coefficient represents the aerodynamics of the turbine blades, and it can be expressed as a function of the tip speed ratio  $\lambda$  and the blade angle  $\beta$  representing the pitch of the blades [18]:

$$C_p(\lambda, \lambda_{ai}, \beta) = 0.5176 \left( \frac{116}{\lambda_{ai}} - 0.4\beta - 5 \right) \exp\left(\frac{-21}{\lambda_{ai}}\right) + 0.0068\lambda \quad (5)$$

where

$$\lambda_{ai}(\lambda, \beta) = \left( \frac{1}{\lambda + 0.08\beta} - \frac{0.035}{\beta^3 + 1} \right)^{-1} \quad (6)$$

Because this paper models the wind farm in an aggregated form, a gain representing the total number of turbines,  $N_{turbines}$ , is added to the power output from the model.

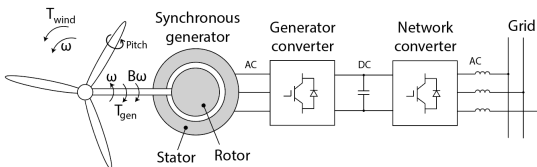


Fig. 4. A schematic of a Type IV turbine showing the basic variables used in the turbine model.

1) *Turbine controllers:* The turbine model has two control loops: one speed controller and one pitch controller.

The speed controller controls the torque of the electrical generator to regulate the speed of the turbine. This is done to maintain an optimal tip speed ratio,  $\lambda$ , optimizing the power coefficient,  $C_p$ , for wind conditions up to the rated wind speed,  $u_{rated}$ .

The pitch controller is activated for wind conditions above the rated wind speed. It is used to control the blade angle,  $\beta$ , to shed excess power when the wind speeds are above the rated value.

### D. Energy storage model

The energy storage model consists of three power flows; one describing the output from the power electronics,  $P_{pe}$ , one describing the losses in the storage system,  $P_{loss}$  and one power flow that represents the power at the storage terminals,  $P_{es}$ . The equations describing the storage system are as follows:

$$P_{es} = P_{pe} + P_{loss} \quad (7)$$

$$W_{es} = \int -P_{es} \quad (8)$$

$$SOC = \frac{W_{es}}{W_{rated}} \quad (9)$$

$$0 \leq SOC \leq 1 \quad (10)$$

where  $SOC$  is the state of charge, describing how much of the total capacity the storage unit is charged, and  $W_{es}$  is the accumulated energy stored in the unit.

Two charging states of the storage unit are defined; a charging and a discharging state. The equations describing the storage unit when it is discharging are:

$$P_{pe} > 0 \quad (11)$$

$$P_{pe} = \eta \cdot P_{es} \quad (12)$$

$$P_{loss} = \left( \frac{1}{\eta} - 1 \right) \cdot P_{pe} \quad (13)$$

where  $\eta$  is the charging and discharging efficiency of the energy storage system, hence assumed to be equal.

Next, the equations describing the unit when it is charging are:

$$P_{pe} < 0 \quad (14)$$

$$P_{es} = \eta \cdot P_{pe} \quad (15)$$

$$P_{loss} = (\eta - 1) \cdot P_{pe} \quad (16)$$

Also, to represent the delay in the storage system, a first-order transfer function is added to the power output of the storage. The filter time constant use in this paper is  $T_{delay} = 10ms$ . This is a small time constant that represents a fast energy storage system as, e.g., electrochemical energy storage systems. Examples of such electrochemical energy storage systems are lithium-ion and lead-acid [19], [20].

Additionally, a storage protection system is added to limit the state of charge between 20% and 90%. Also, the protection system prevents the storage system from charging and discharging beyond the rated power.

### E. HVDC cable model

The HVDC cable used for this study is a circuit representation of a frequency dependent cascaded pi representation from [21]. This model captures the behavior of the frequency dependent parameters as resistances and inductances for a wide range of frequencies in addition to the effects of the hyperbolic correction factors in an actual cable. These aspects can be crucial in long cable implementations such as those used in offshore applications.

## IV. SIMULATION CASES AND RESULTS

### A. Simulation case 1: Contribution of the MMC through the internal storage

Since the MMC contains several submodules connected in cascade, each comprising a capacitor, the MMC has some energy storage capability characterized by short charge and discharge periods. Control of this stored energy could thus be executed to improve power dynamics that occur over relatively short periods ranging from milliseconds to a couple of seconds depending on the energy requirement.

To investigate the support capability of the MMC with regards to power dynamics, two test cases were simulated. In the first test-case, the MMC attempts to smoothen out power variations arising from the turbine dynamics caused by wind speed fluctuation. In the second, the MMC attempts to reduce the response time of the HVDC system upon a step in power reference.

1) *Responding to turbine dynamics:* To investigate the improving impact an MMC can have on the power dynamics of a wind turbine caused by wind speed fluctuation, this aspect of fig. 1 was investigated using the isolated sub-system, corresponding to the model depicted in fig. 5.

The wind speed was varied around the rated wind speed of the controllers with a maximum variation of  $0.2m/s$  to induce power fluctuation relating to the turbine dynamics. The controller used to determine  $w_{\Sigma,z,ref}$  was a PI controller, taking  $P_{WF} - P_{ref}$  as input. To ensure that the controller did not deplete the capacitors, the admissible energy range was determined to be  $0.7 \leq w_{\Sigma,z,ref} \leq 1.3$ . The simulation was run twice. The first time the aforementioned control was implemented and in the second,  $w_{\Sigma,z,ref}$  was set equal to 1, i.e. no contribution from the internal storage in the MMC.

2) *Results:* The power delivered to the grid, together with the p.u. wind speed and rotational speed of the wind turbine, are depicted in fig. 6.

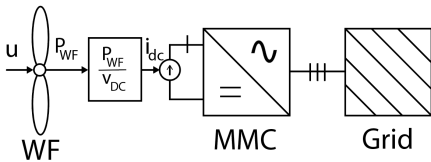


Fig. 5. Test case used to isolate the power dynamics of the turbine and MMC for Simulation case 1.

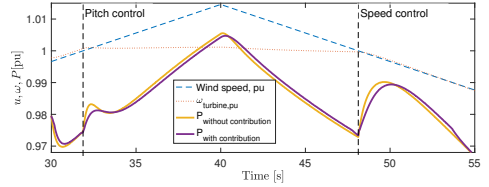


Fig. 6. Response of the powers delivered to the grid with and without contribution from the MMCs internal storage for Simulation case 1.

The most interesting section of this power dynamic is for  $30s \leq t \leq 35s$ . During this period, the wind speed increases from below the rated value, i.e. the threshold value for the pitch controller to above the threshold value. Upon crossing this threshold, the turbine operation is changed from speed control to pitch control. The pitch angle controller is activated to shed the excess power. However, because of the delay of 1 second associated with the pitching of the blade angles, for a small time period, this extra power is fed into the converter. Additionally, the speed controller decelerates the angular velocity of the turbine releasing some of its kinetic energy.

When  $w_{\Sigma,z,ref}$  is kept constant at 1 pu, this power fluctuation flows directly through the converter without being absorbed. However, when the converter is allowed to vary  $w_{\Sigma,z,ref}$ , this excess energy is absorbed by the converter, (fig. 7). This dampens the power fluctuation by reducing the fluctuation from 0.009 p.u. to 0.006 p.u.

Subsequently, while  $t \leq 48s$  the wind speed increases and decreases within the same control region. When the wind speed increases the converter absorbs energy and when the wind speed falls the converter releases energy, as shown in fig. 7. However, the time periods are so long that this energy absorption (and release) only manifest as a negligible impacts on the power response, see fig. 6.

When  $48s \leq t \leq 54s$ , the wind speed is reduced below the threshold value, and the speed controller is activated. Thus, the rotational speed of the turbine decelerates releasing some of the rotational kinetic energy stored in the inertia of the turbine to be converted and released as electrical energy into the converter. Once again, the energy absorption only causes negligible impact on the power profile. Afterwards, the converter has reached its lower energy limit and cannot release more energy. Therefore, the two power profiles converge.

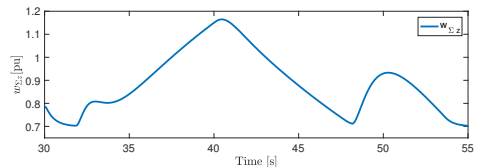


Fig. 7. Response of the internal stored energy in Simulation case 1.

3) *Response to steps in power reference:* To investigate if the MMC could improve the power step response of the HVDC system, the sub-system depicted in fig. 8 was analyzed.

MMC2 controls the power flow to Grid 3. A step in power reference from 0.7 to 0.8 was executed at  $t = 1$  s. The simulations were run twice. During the first simulation  $w_{\Sigma,z,ref}$  was controlled by a PI controller and in the second  $w_{\Sigma,z,ref}$  was set equal to 1.

4) *Results:* Figure 9 shows the difference in response of the internal energies of the MMC when using the two control strategies.

The p.u. powers delivered to Grid 3 are displayed in fig. 10 with and without control of  $w_{\Sigma,z,ref}$ , thereby with and without contribution from the MMCs internally stored energy.

As can be seen, when the energy controller controls  $w_{\Sigma,z,ref}$  to release energy upon a step in the power reference, the stored converter energy starts to decline and the output power of the converter reaches the power level around its reference faster than when  $w_{\Sigma,z,ref}$  is set constant to 1 pu.

In both cases,  $w_{\Sigma,z,pu}$  declines upon the step, causing the power leaving the converter to exceed the power entering the converter from the HVDC cable. However, when  $w_{\Sigma,z,ref}$  is maintained at 1, the rate of change of the converter energy declines after 1 ms. Therefore, the difference between the power delivered to the grid and the power entering the converter decreases, until the converter starts to recharge at  $t = 4.3$  ms after the step. Because of the recharging of the converter, there is some additional delay before the converter output energy rises again, but subsequently, it exponentially approaches its reference. When  $w_{\Sigma,z,ref}$  is controlled, the power delivered to the grid overshoots and subsequently oscillates below its reference. This oscillatory behaviour was reduced in [13], by releasing the energy in an exponentially decaying manner based on the size of the step in power reference. This reduced the overshoot from 14% of the step size to 6% of the step size and reduced the undershoot by almost 3 orders of magnitude.

This simulation shows that control of the zero-sequence energy can reduce the power step response time of the HVDC system.

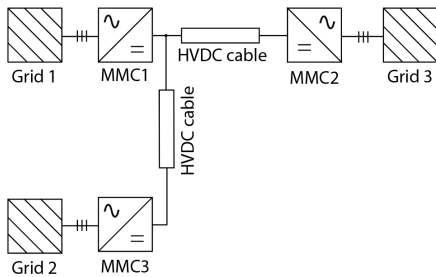


Fig. 8. System build to investigate MMC induced improvements of power step responses of HVDC systems for Simulation case 1.

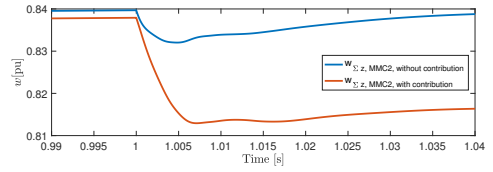


Fig. 9. Response of the stored energy in the MMC for Simulation case 1.

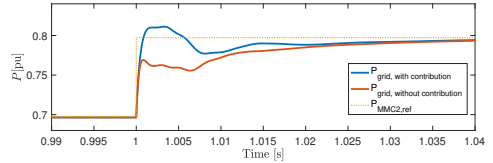


Fig. 10. Response of powers in the system for Simulation case 1.

### B. Simulation case 2: Energy storage dimensioning

Simulation case 2 aims at pre-sizing the energy storage system before it is integrated into the three-terminal HVDC system in Simulation case 3. Simulation case 2 uses a configuration where the power from the wind farm is filtered through a large first order filter, as shown in fig. 11. The difference between the filtered power and the actual power is sent as a reference for the energy storage system. This way, the combined power from the wind farm and the energy storage will have a much smoother profile than the power from the wind farm alone when the energy storage and the filter are properly dimensioned.

To dimension the energy storage rated power, the real wind speed profile shown in fig. 12 was used. These are actual wind speed data measured at Roosevelt station over approximately 20 hours.

1) *Results:* Figure 13 shows the power from WF1, the power from the energy storage, and the combined storage and wind farm power output after dimensioning of the energy storage rated power and the filter time constant.

These results and the interaction between the wind farm and the energy storage were considered satisfactory and led to the choice of a  $P_{rated}$  of 250MW for the energy storage, assuming a time constant of  $T = 1000$ s for the first order filter used to filter the power output from the wind farm.

Additionally, the state of charge was used as an indicator

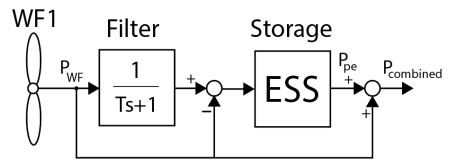


Fig. 11. Simulation setup for Simulation case 2.

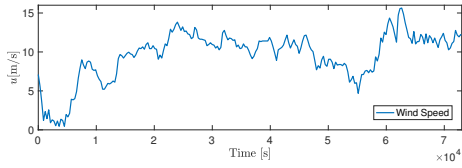


Fig. 12. The wind speed variation used for dimensioning.

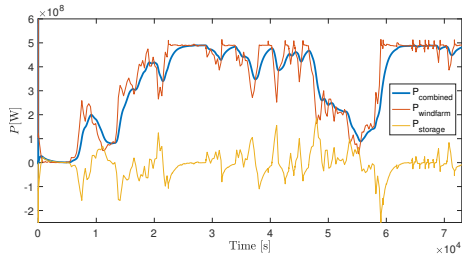


Fig. 13. Power from wind turbine, energy storage and combined power from Simulation case 2.

during the process of finding the rated values. From fig. 14, it can be seen that the state of charge varies in the whole range between its limits of 0.2 and 0.9 without capping at the limits during the simulation. This was regarded as an indicator that the storage was not over- nor under-dimensioned, resulting in proper utilization of the available capacity.

### C. Simulation case 3: Three-terminal HVDC system with wind power and energy storage integration

To study the short term effects of integrating an energy storage system offshore near one of the wind farms in fig. 15, the configuration of Simulation case 2 was added to WF1 and the energy storage system in the final simulation system showed in fig. 15.

The offshore AC-grids are modeled by voltage sources as stiff grids, and the power outputs from the wind farm models and energy storage model are applied at the references of their respective MMC.

Two events are introduced to study the differences in responses of the system when an event occurs at WF1 with an energy storage system nearby and WF2 without an energy storage system. A sudden drop in wind speed from 10 m/s to

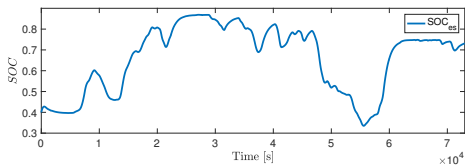


Fig. 14. The state of charge (SOC) of the energy storage from Simulation case 2.

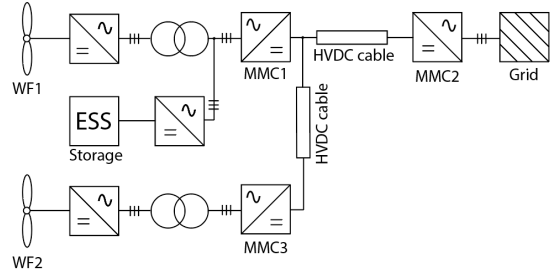


Fig. 15. Simulation system of Simulation case 3. Figure 1 repeated for convenience.

5m/s is introduced first at WF1 at  $t = 30$ s then at WF2 at  $t = 60$ s.

In this simulation case,  $w_{\Sigma,z,ref}$  is kept constant at 1pu for all of the MMCs.

1) *Results:* Figure 16 shows the response of the power from WF1, WF2 and the energy storage when a sudden drop in wind speed is introduced. From the figure, it can be seen how the energy storage system quickly reacts after the power from WF1 drops, to maintain a *more* constant power to MMC1.

Figure 17 shows the response of the MMC powers under the same conditions. From the figure it can be seen how the power delivered to shore from MMC2 is *more* constant when there is a drop in wind speed at WF1 with an energy storage system compared to when there is a drop at WF2, which has no energy storage system.

Figure 18 shows the response of the DC voltages at the MMC terminals when a sudden drop in wind speed is introduced. It can be seen that the response of the DC voltages is improved for the event at WF1 at  $t = 30$ s compared to the event at WF2 at  $t = 60$ s due to the fast contribution of

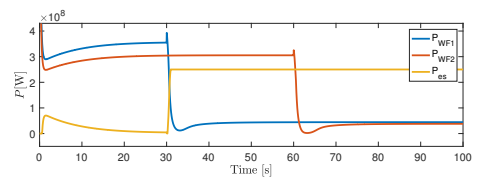


Fig. 16. The response of the wind farm powers and energy storage powers when two sudden drops in wind speed are introduced in Simulation case 3.

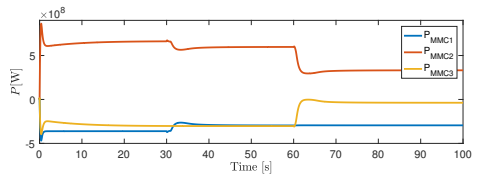


Fig. 17. Response of the MMC powers during two sudden drops in wind speeds is introduced in Simulation case 3.

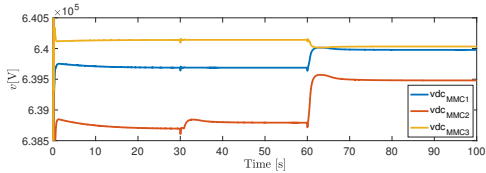


Fig. 18. The response of the DC voltages during two sudden drops in wind speeds is introduced in Simulation case 3.

the energy storage system. In the first case, the *more* constant power output from MMC1 means that the DC voltage levels do not have to be adjusted when there is a drop in the wind speed compared to the case when the wind speed drops at WF2.

Figure 19 shows the response of the zero-sequence energy sum in the MMCs when a sudden drop in wind speed is introduced. The response of the energies are also improved for the case of an event at WF1 at  $t = 30$ s compared to WF2 at  $t = 60$ s due to the fast contribution of the energy storage system.

## V. DISCUSSION

### A. The internal storage contribution of the MMC

As seen from the results, the internally stored energy in the MMCs is not large enough to account for the short term variations in the wind with the values used in this paper. However, the internal storage can be increased by either increasing the number of sub-modules in the MMC or by increasing the rated voltage of each sub-module or a combination of both.

However, because the MMC can improve fast responses as the step response of the converter, it may be beneficial to use the MMC to smooth the most rapid variations in the wind from e.g. wind gusts and tower shadowing, as studied in [22]. Possibly, these capabilities could also be used for other purposes such as power oscillation damping, improve voltage behaviour, increasing the life span of batteries by eliminating ripple or providing initial frequency response and system inertia [23]–[26].

### B. Justification for offshore storage placement

In this study, the energy storage system was placed offshore near one of the wind farms. This was done to study the effects on the HVDC system when having a storage system

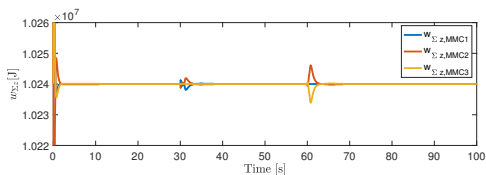


Fig. 19. The response of the zero-sequence energy of the MMCs during two sudden drops in wind speeds in Simulation case 3.

offshore, and directly compare a wind farm complemented with energy storage to a wind farm without energy storage. The configuration was practical for directly comparing the effects of events at both wind farms without changing the configuration of the system model.

Further, one can argue that in addition to improved operation of the HVDC system, the energy storage system can be placed offshore to fully utilize the flexibility of HVDC grids. By having the energy storage near the wind farm, the same constant power profile can be delivered regardless of the power flow direction to shore. This may be beneficial in cases where, e.g., different countries are connected by the HVDC grid. The offshore placement of the energy storage system allows the same power to flow to country  $x$  as country  $y$ , without having separate energy storage systems connected at the onshore terminals of both countries.

However, the topic of offshore versus onshore placement of the energy storage and its multiple techno-economic implications were not the main focus of this paper, and should, therefore, be addressed in separate studies.

### C. Storage dimensioning

Dynamic simulations using only one wind speed series are used for pre-sizing of the energy storage system to be used further in the paper. As the dimensioning of the storage was not the main focus of this paper, the approach was chosen for its simplicity, and without presumption of generality, mainly to demonstrate one practical usage of simulations in the OpenModelica software. It should, therefore, be clarified that this approach is very simple compared to actual dimensioning of energy storage systems for real wind farms.

Also, the chosen rated power of the energy storage system was 250MW, which corresponds to around half of the rated power from the wind farm nearby, containing 70 turbines with a rated power of 7MW. The rated power from the energy storage system is therefore not enough to cover the rated power from the wind farm, and it is therefore just a complement to the wind farm production resulting in more constant operation. Economic considerations relating how this can be used to financially justify the ESS investment and considerations recommending a smaller energy storage system sizing were left outside the scope of this paper. The results from simulation case 2 when using a rated power of the same as the wind farm did not show a good enough increase in performance to justify the potential increases in costs of a larger energy storage system.

### D. Using OpenModelica for real-time HIL testing

To further address the usage of the OpenModelica for model sharing through the Functional Mock-up Interface (FMI) standard and usage in real-time HIL testing, preliminary testing was performed at the National Smart Grid laboratory in Trondheim. A review of the available literature revealed the lack of information on how to build and prepare OpenModelica models for one of Opal-RT's real-time simulators, ePHASOR-SIM. However, a short guide inside the software was found,

but this guide lacked some important details. Therefore, this aspect was investigated further to increase the usefulness of the OpenModelica software in the context of modeling HVDC grids for real-time HIL testing.

Multiple models, including a model of an MMC and a point-to-point HVDC connection using MMCs were implemented in OpenModelica, exported for the real-time simulator and successfully run in a larger system model with the real-time simulator. The approach is further described in [12], [13], and by following the included guide, HVDC grid models developed in OpenModelica can be used for real-time HIL simulations for future experimental validation and testing. The guide found in [12], [13] adds to the information found inside the software.

The real-time simulation models are added to the aforementioned GitHub folder for illustration purposes. However, to have complete access to all components in the model, the Opal-RT Modelica Developer library is needed. This library is handed out by Opal-RT's customer support upon request.

## VI. CONCLUSIONS

In this paper, a three-terminal HVDC system with offshore wind and energy storage integration was modeled in OpenModelica, including the key components in an HVDC grid. The paper started by introducing the open source modeling software OpenModelica with a preliminary assessment of the performance of the software. The software was tested for the fast dynamics of a switching model of a 10kHz 2L-VSC with comparison to Simulink. The results showed that OpenModelica successfully reproduced these fast dynamics.

Next, the models for the MMC, the wind farms, the HVDC cables, and the energy storage system were described and a description of the simulation cases studied in the paper was presented.

The first simulation case showed that the internal energy of an MMC can improve the step response of the active power delivered to the grid from a three-terminal HVDC system. Further, the second simulation case showed that the contribution of the MMCs is very small when considering short term variations in the wind. Therefore, it is recommended to consider using the MMC for smoothing the most rapid changes in power due to wind gusts, tower shadowing, etc.

The third simulation used real wind speed data to pre-dimension an external energy storage system to smooth the hourly variations in power production due to changes in wind speeds. Lastly, the fourth and final simulation case combined the three terminal HVDC system with two wind farms and an energy storage system to study the short term effects of having an energy storage system at one wind farm. The results using a fast energy storage system showed that the overall operation of the HVDC system was improved when using an energy storage system, leading to smaller transients in the responses of the DC voltage and internal energy storage when wind speeds suddenly dropped.

Additionally, models developed in the software were tested in the National Smart Grid laboratory with Opal-RT's real-time

simulator ePHASORSIM. This allows for future experimental testing and validation using HIL simulations.

All simulations were performed in the open source tool OpenModelica, and the models were made publicly available to anyone for any purpose, e.g. future studies including more HVDC terminals. This paper can be used as a reference for the use of such models.

## VII. ACKNOWLEDGMENTS

The authors would like to express their gratitude towards Dr. Yongtao Yang in DNV GL for his guidance and advisory in the development of this paper and the associated Master's Theses.

## REFERENCES

- [1] Wind Europe, "Wind in power 2018: Annual combined onshore and offshore wind energy statistics," 2018.
- [2] Wind Europe, "Wind energy in Europe: scenarios for 2030," 2017.
- [3] H. Björklund, "Strong winds, high yield," in ABB review - special report 60 years of HVDC. pp. 22–25, 2014.
- [4] M. P. Bahrman and B. K. Johnson, "The ABCs of HVDC transmission technologies," in IEEE Power and Energy Magazine, vol. 5, no. 2, pp. 32–44, March–April 2007. doi: 10.1109/MPAE.2007.329194
- [5] Weixing Lu and Boon-Teck Ooi, "Optimal acquisition and aggregation of offshore wind power by multiterminal voltage-source HVDC," in IEEE Transactions on Power Delivery, vol. 18, no. 1, pp. 201–206, Jan. 2003. doi: 10.1109/TPWRD.2002.803826
- [6] R. Marquardt, "Modular multilevel converter: An universal concept for HVDC-Networks and extended DC-Bus-applications," The 2010 International Power Electronics Conference - ECCE ASIA -, Sapporo, 2010, pp. 502–507. doi: 10.1109/IPEC.2010.5544594
- [7] K. Ilves, S. Norrga, L. Harnefors and H. Nee, "On energy storage requirements in modular multilevel converters," in IEEE Transactions on Power Electronics, vol. 29, no. 1, pp. 77–88, Jan. 2014. doi: 10.1109/TPEL.2013.2254129
- [8] A. Taffese, A. Endeganew, S. Sanchez, E. Tedeschi, "Reducing rapid wind farm power fluctuations using the modular multilevel converter", unpublished.
- [9] D. Van Hertem, O. Gomis-Bellmunt and J. Liang, "HVDC grids", Wiley Online Library, 2016.
- [10] D. Winkle and C. Gühmann, "Hardware-in-the-Loop simulation of a hybrid electric vehicle using Modelica/Dymola," in Proceedings of the 22nd international battery, hybrid and fuel cell Electric Vehicle Symposium (EVS-22), Yokohama, Japan, pp. 1054–1063, 2006.
- [11] M. Otter, C. Schlegel and H. Elmqvist, "Modeling and realtime simulation of an automatic gearbox using Modelica," in Proceedings of ESS, pp. 19–23, Citeseer, 1997.
- [12] J. Espvik, "Modeling of multiterminal HVDC grids with renewable energy and storage integration by open source tools for HIL applications", M.S. thesis, Norwegian University of Science and Technology, Trondheim, June 2019.
- [13] E. Tranulis, "Modeling MMC energy dynamics in offshore HVDC systems using OpenModelica", M.S. thesis, Norwegian University of Science and Technology, Trondheim, June 2019.
- [14] S. Khan, E. Tedeschi, "Modeling of MMC for fast and accurate simulation of electromagnetic transients: a review," in Energies, vol. 10, no. 8, 2017. doi: 10.3390/en10081161
- [15] G. Bergna-Diaz, J. A. Suul and S. D'Arco, "Energy-based state-space representation of modular multilevel converters with a constant equilibrium point in steady-state operation," in IEEE Transactions on Power Electronics, vol. 33, no. 6, pp. 4832–4851, June 2018. doi: 10.1109/TPEL.2017.2727496
- [16] G. Bergna, J. A. Suul and S. D'Arco, "State-space modelling of modular multilevel converters for constant variables in steady-state," 2016 IEEE 17th Workshop on Control and Modeling for Power Electronics (COMPEL), Trondheim, 2016, pp. 1–9. doi: 10.1109/COMPEL.2016.7556695
- [17] C. Bajracharya, M. Molinas, J. A. Suul, T.M. Undeland, Tore M, "Understanding of tuning techniques of converter controllers for VSC-HVDC," in Nordic Workshop on Power and Industrial Electronics (NORPIE/2008), June 9–11, 2008, Espoo, Finland, 2008.

APPENDIX

[18] S. Heier, "Grid integration of wind energy: onshore and offshore conversion systems", John Wiley & Sons. 2014.

[19] H. Hesse, M. Schimpe, D. Kucevic and A. Jossen, "Lithium-ion battery storage for the grid a review of stationary battery storage system design tailored for applications in modern power grids", in *Energies*, vol. 10, no. 12, 2017.

[20] B. McKeon, J. Furukawa, Jun and S. Fenstermacher, "Advanced lead-acid batteries and the development of grid-scale energy storage systems", in *Proceedings of the IEEE*, vol. 102, no. 6, pp. 951–963, 2014.

[21] J. Beerten, S. D'Arco and J. A. Suul, "Frequency-dependent cable modelling for small-signal stability analysis of VSC-HVDC systems," in *IET Generation, Transmission & Distribution*, vol. 10, no. 6, pp. 1370-1381, 21 4 2016. doi: 10.1049/iet-gtd.2015.0868

[22] A. Taffese, A. Endegnanew, S. Sanchez, E. Tedeschi, "Reducing rapid wind farm power fluctuations using the modular multilevel converter", unpublished.

[23] A. A. Taffese, E. Tedeschi and E. de Jong, "A control scheme for utilizing energy storage of the modular multilevel converter for power oscillation damping," 2017 IEEE 18th Workshop on Control and Modeling for Power Electronics (COMPEL), Stanford, CA, 2017, pp. 1-8. doi: 10.1109/COMPEL.2017.8013415

[24] A. E. Leon, "Short-term frequency regulation and inertia emulation using an MMC-Based MTDC System," in *IEEE Transactions on Power Systems*, vol. 33, no. 3, pp. 2854-2863, May 2018. doi: 10.1109/TPWRS.2017.2757258

[25] J. Freytes et al., "Dynamic analysis of MMC-based MTDC grids: use of MMC energy to improve voltage behavior," in *IEEE transactions on power delivery*, vol. 34, no. 1, pp. 137-148, Feb. 2019. doi: 10.1109/TPWRD.2018.2868878

[26] I. Puranik, L. Zhang and J. Qin, "Impact of low-frequency ripple on lifetime of battery in MMC-based battery storage systems," 2018. 10.1109/ECCE.2018.8558061.

[27] C. A. Bharadwaj and S. Maiti, "Modular multilevel converter based hybrid energy storage system," 2017 IEEE PES Asia-Pacific Power and Energy Engineering Conference (APPEEC), Bangalore, 2017, pp. 1-6. doi: 10.1109/APPEEC.2017.8308983

TABLE I  
SYSTEM PARAMETERS

Component	System parameters		
	Parameter	Value	Unit
MMC	$S_n$	1059	MVA
MMC	$V_n$	333	kV
MMC	$R_{a,pu}$	0.005	p.u.
MMC	$R_{f,pu}$	0.00285	p.u.
MMC	$L_{a,pu}$	0.08	p.u.
MMC	$L_{f,pu}$	0.16428	p.u.
MMC	$C_{eq,pu}$	0.8	p.u.
MMC	$C_{DC,pu}$	0.051637	p.u.
HVDC cable	$C_l$	0.1983	$\mu\text{F}/\text{km}$
HVDC cable	$G_l$	$7.6330 \cdot 10^{-11}$	$\text{S}/\text{km}$
HVDC cable	$R_{1l}$	$1.1724 \cdot 10^{-1}$	$\Omega/\text{km}$
HVDC cable	$R_{2l}$	$8.2072 \cdot 10^{-2}$	$\Omega/\text{km}$
HVDC cable	$R_{3l}$	$1.1946 \cdot 10^{-2}$	$\Omega/\text{km}$
HVDC cable	$L_{1l}$	$2.2861 \cdot 10^{-1}$	$\text{mH}/\text{km}$
HVDC cable	$L_{2l}$	1.5522	$[\text{mH}/\text{km}]$
HVDC cable	$L_{3l}$	3.2943	$[\text{mH}/\text{km}]$
Turbine	$P_{rated}$	7	MW
Turbine	$J$	$4 \cdot 10^6$	$\text{kgm}^2$
Turbine	$B$	$2 \cdot 10^6$	$\text{sN}^{-1}\text{m}^{-1}$
Turbine	$\ell$	75	m
Turbine	$\rho$	1.2	$\text{kgm}^{-3}$
Turbine	$\lambda_{opt}$	8.1	p.u.
Turbine	$C_{pmax}$	0.48	p.u.
Turbine	$u_{rated}$	11.14	$\text{ms}^{-1}$
Turbine	$T_{pitch}$	1	s
ESS	$P_{rated}$	250	MW
ESS	$t_{rated}$	1	hour
ESS	$\eta$	0.9304	hour
ESS	$SOC_{lim,upper}$	0.9	p.u.
ESS	$SOC_{lim,lower}$	0.2	p.u.
ESS	$T_{delay}$	10	ms

---

# Appendix **B**

## Model Parameters and definitions

### B.1 Per unit definitions

Table B.1: Per unit definitions

Parameter	definition
$S_{base}$	$S_n$
$\omega_{base}$	$2V_{DC,base}^2 \frac{1}{2} C_{eq}$
$V_{base}$	$\sqrt{\frac{2}{3}} V_n$
$I_{base}$	$\sqrt{\frac{2}{3}} \frac{S_n}{V_n}$
$\omega_{base}$	$2\pi 50$
$Z_{base}$	$\frac{V_{base}}{I_{base}}$
$L_{base}$	$\frac{Z_{base}}{\omega_{base}}$
$C_{base}$	$\frac{1}{Z_{base} \omega_{base}}$
$V_{DC,base}$	$2V_{base}$
$I_{DC,base}$	$\frac{S_{base}}{V_{DC,base}}$
$Z_{DC,base}$	$\frac{V_{DC,base}}{I_{DC,base}}$

---

## B.2 MMC parameters

Table B.2: MMC parameters

Parameter	value	unit
$S_n$	1000	MVA
$V_n$	313.5	kV
$R_{a,pu}$	0.005	p.u
$R_{f,pu}$	0.00285	p.u
$L_{a,pu}$	0.08	p.u
$L_{f,pu}$	0.16428	p.u
$C_{eq,pu}$	0.8	p.u
$C_{DC,pu}$	0.051637	p.u
$K_{cc,p}$	2.6	-
$K_{cc,i}$	21.4	-
$K_{\odot,cc,p}$	0.11	-
$K_{\odot,cc,i}$	2.17	-
$K_{w,\Sigma,z,p}$	10	-
$K_{w,\Sigma,z,p}$	10	-
$K_{vc,p}$	0.726	-
$K_{vc,i}$	33.2	-

## B.3 2L-VSC parameters

Table B.3: 2L-VSC parameters

Parameter	definition	
$S_n$	20	kVA
$V_n$	400	V
$R_{pu}$	0.01	p.u
$L_{pu}$	0.15	p.u
$C_{pu}$	0.87	p.u
$K_{cc,p}$	0.796	-
$K_{cc,i}$	16.67	-
$K_{vc,p}$	2.53	-
$K_{vc,i}$	725	-
$\tau_{PWM}$	$\frac{1}{10000}$	$s^{-1}$

---

## B.4 ePHASORsim test parameters: MMC\_base

Table B.4: MMC\_BASE parameters

Parameter	value	unit
$S_b$	1.059	GVA
$V_b$	271893	V
$V_{bdc}$	640	kV
$C_{sm}$	0.01	p.u.
$N$	400	-
$f_b$	50	$s^{-1}$
$L_f$	0.06	p.u.
$L_a$	0.05	p.u.
$R_f$	0.001	p.u.
$R_a$	0.001	p.u.

## B.5 ePHASORsim test parameters: HVDC\_BASE

Table B.5: HVDC\_BASE parameters

Parameter	value	unit
$S_b$	$1.06 \cdot 10^9$	VA
$V_b$	271893	V
$L_a$	0.05	p.u.
$R_a$	0.001	p.u.
$L_f$	0.06	p.u.
$R_f$	0.001	p.u.
$V_{bdc}$	640000	V
$C_{sm}$	0.01	p.u.
$N$	400	-
$f_b$	50	$s^{-1}$
$C_{dc}$	$1.67 \cdot 10^{-6}$	F

---

## B.6 Cable

Table B.6: Cable parameters [51]

Parameter	vale	
$C_l$	0.1983	$[\mu F/km]$
$G_l$	$7.6330 \cdot 10^{-11}$	$[S/km]$
$R_{1l}$	$1.1724 \cdot 10^{-1}$	$[\Omega/km]$
$R_{2l}$	$8.2072 \cdot 10^{-2}$	$[\Omega/km]$
$R_{3l}$	$1.1946 \cdot 10^{-2}$	$[\Omega/km]$
$L_{1l}$	$2.2861 \cdot 10^{-1}$	$[mH/km]$
$L_{2l}$	1.5522	$[mH/km]$
$L_{3l}$	3.2943	$[mH/km]$

## B.7 Turbine Parameters

Table B.7: Turbine parameters [101]

Parameter	vale	unit
$P_{rated}$	2	$[MW]$
$J$	$3 \cdot 10^6$	$[kgm^2]$
$B$	$2 \cdot 10^6$	$[sN^{-1}m^{-1}]$
$\ell$	40	$[m]$
$\rho$	1.2	$[kgm^{-3}]$
$\lambda_{opt}$	8.1	-
$Cp_{max}$	0.48	-
$K_{pc,p}$	$2.5 \cdot 10^{-6}$	-
$K_{pc,i}$	$6 \cdot 10^{-7}$	-
$K_{pc,x}$	1	-
$K_{\tau c,p}$	$10^7$	-
$K_{\tau c,i}$	$10^6$	-
$K_{\tau c,x}$	1	-

---

## B.8 Behavior-based Energy reference controller parameters

Table B.8: Parameters defining zero-sequence energy sum during power step

Parameter	value	unit
$w_{offset}$	1	p.u.
$w_{step}$	$-0.33\Delta P_{ref}$	p.u.
$t_{step}$	1.1	s
$t_{RT}$	1	s
$t_{RTC}$	0.01	s
$t_{Recharge}$	10	s

## B.9 Transformation Matrix

For the transformation between a stationary reference frame and synchronous reference frames, the following transformation matrices are used.

$$\mathbf{T}_\omega = \frac{2}{3} \begin{bmatrix} \cos(\omega t) & \cos(\omega t - \frac{2\pi}{3}) & \cos(\omega t - \frac{4\pi}{3}) \\ -\sin(\omega t) & -\sin(\omega t - \frac{2\pi}{3}) & -\sin(\omega t - \frac{4\pi}{3}) \\ \frac{1}{2} & \frac{1}{2} & \frac{1}{2} \end{bmatrix} \quad (\text{B.1})$$

$$\mathbf{T}_\omega^{-1} = \begin{bmatrix} \cos(\omega t) & -\sin(\omega t) & 1 \\ \cos(\omega t - \frac{2\pi}{3}) & -\sin(\omega t - \frac{2\pi}{3}) & 1 \\ \cos(\omega t - \frac{4\pi}{3}) & -\sin(\omega t - \frac{4\pi}{3}) & 1 \end{bmatrix} \quad (\text{B.2})$$

---

# Appendix **C**

## Proofs

### **C.1 Energy sum derivation**

$$ParkTransform := \frac{2}{3} \begin{bmatrix} \cos(\omega t) & \cos\left(\omega t - \frac{2\pi}{3}\right) & \cos\left(\omega t + \frac{2\pi}{3}\right) \\ -\sin(\omega t) & -\sin\left(\omega t - \frac{2\pi}{3}\right) & -\sin\left(\omega t + \frac{2\pi}{3}\right) \\ \frac{1}{2} & \frac{1}{2} & \frac{1}{2} \end{bmatrix};$$

$$ParkTransform := \begin{bmatrix} \frac{2 \cos(\omega t)}{3} & -\frac{2 \cos\left(\omega t + \frac{\pi}{3}\right)}{3} & -\frac{2 \sin\left(\omega t + \frac{\pi}{6}\right)}{3} \\ -\frac{2 \sin(\omega t)}{3} & \frac{2 \sin\left(\omega t + \frac{\pi}{3}\right)}{3} & -\frac{2 \cos\left(\omega t + \frac{\pi}{6}\right)}{3} \\ \frac{1}{3} & \frac{1}{3} & \frac{1}{3} \end{bmatrix} \quad (1)$$

$$ParkTwoTransform := \frac{2}{3} \begin{bmatrix} \cos(-2\omega t) & \cos\left(-2\omega t - \frac{2\pi}{3}\right) & \cos\left(-2\omega t + \frac{2\pi}{3}\right) \\ -\sin(-2\omega t) & -\sin\left(-2\omega t - \frac{2\pi}{3}\right) & -\sin\left(-2\omega t + \frac{2\pi}{3}\right) \\ \frac{1}{2} & \frac{1}{2} & \frac{1}{2} \end{bmatrix};$$

$$ParkTwoTransform := \begin{bmatrix} \frac{2 \cos(2\omega t)}{3} & -\frac{2 \sin\left(2\omega t + \frac{\pi}{6}\right)}{3} & -\frac{2 \cos\left(2\omega t + \frac{\pi}{3}\right)}{3} \\ \frac{2 \sin(2\omega t)}{3} & \frac{2 \cos\left(2\omega t + \frac{\pi}{6}\right)}{3} & -\frac{2 \sin\left(2\omega t + \frac{\pi}{3}\right)}{3} \\ \frac{1}{3} & \frac{1}{3} & \frac{1}{3} \end{bmatrix} \quad (2)$$

Loading [LinearAlgebra](#)

Loading [LinearAlgebra](#)

$ParkTransform\_inv := combine(MatrixInverse(ParkTransform));$

$ParkTransform\_inv := MatrixInverse(ParkTransform) \quad (3)$

$ParkTwoTransform\_inv := combine(MatrixInverse(ParkTwoTransform));$

$ParkTwoTransform\_inv := MatrixInverse(ParkTwoTransform) \quad (4)$

$$Power\_gc := combine \left( simplify \left( combine \left( ParkTwoTransform. \left( \left( ParkTransform\_inv. \begin{bmatrix} i\_cd \\ i\_cq \\ 0 \end{bmatrix} \right) \right) \right) \right) \right) \sim$$

$$\left( \left( \left( \left( \text{ParkTransform\_inv.} \begin{bmatrix} v\_gd \\ v\_gq \\ 0 \end{bmatrix} \right) \right) \right), \{ \sin(x)^2 + \cos(x)^2 - 1 \} \right) \right) \right) \right) \\ \text{Power\_gc} := \begin{bmatrix} -\frac{i\_cq v\_gq}{2} + \frac{i\_cd v\_gd}{2} \\ -\frac{i\_cd v\_gq}{2} - \frac{i\_cq v\_gd}{2} \\ \frac{i\_cq v\_gq}{2} + \frac{i\_cd v\_gd}{2} \end{bmatrix} \quad (5)$$

$$\text{Power\_circ\_circ\_2} := \text{combine} \left( \text{simplify} \left( \text{combine} \left( \text{ParkTwoTransform.} \left( \left( \left( \text{ParkTwoTransform\_inv} \begin{bmatrix} i\_circ\_d \\ i\_circ\_q \\ i\_circ\_z \end{bmatrix} \right) \right) \right) \cdot \left( \left( \left( \left( \text{ParkTwoTransform\_inv.} \begin{bmatrix} v\_circ\_d \\ v\_circ\_q \\ v\_circ\_z \end{bmatrix} \right) \right) \right), \{ \sin(x)^2 + \cos(x)^2 - 1 \} \right) \right) \right) \right) \right)$$

$$\text{Power\_circ\_circ\_2} := \left[ \left[ \frac{i\_circ\_d v\_circ\_z + i\_circ\_z v\_circ\_d + \frac{i\_circ\_d v\_circ\_q \sin(6 \omega t)}{2}}{2} \right. \right. \\ \left. \left. + \frac{i\_circ\_q v\_circ\_d \sin(6 \omega t)}{2} - \frac{i\_circ\_q v\_circ\_q \cos(6 \omega t)}{2} \right. \right. \\ \left. \left. + \frac{i\_circ\_d v\_circ\_d \cos(6 \omega t)}{2} \right], \right. \\ \left[ \frac{i\_circ\_q v\_circ\_z + i\_circ\_z v\_circ\_q - \frac{i\_circ\_d v\_circ\_q \cos(6 \omega t)}{2}}{2} \right. \\ \left. - \frac{i\_circ\_q v\_circ\_d \cos(6 \omega t)}{2} - \frac{i\_circ\_q v\_circ\_q \sin(6 \omega t)}{2} \right. \\ \left. + \frac{i\_circ\_d v\_circ\_d \sin(6 \omega t)}{2} \right], \\ \left[ \frac{i\_circ\_q v\_circ\_q}{2} + i\_circ\_z v\_circ\_z + \frac{i\_circ\_d v\_circ\_d}{2} \right] \right] \quad (6)$$

$$\text{Power\_circ\_circ} := \text{simplify}(\text{simplify}(\text{simplify}(\text{simplify}(\text{simplify}(\text{Power\_circ\_circ}), \{i\_circ\_d v\_circ\_d\}), \{i\_circ\_q v\_circ\_q\}), \{i\_circ\_d v\_circ\_d\}), \{i\_circ\_d v\_circ\_q\}), \{i\_circ\_q v\_circ\_d\})$$

$$\text{Power\_circ\_circ} := \begin{bmatrix} i\_circ\_d v\_circ\_z + i\_circ\_z v\_circ\_d \\ i\_circ\_q v\_circ\_z + i\_circ\_z v\_circ\_q \\ i\_circ\_z v\_circ\_z \end{bmatrix} \quad (7)$$

$$\text{Energy\_sum} = 2 \cdot \text{Power\_circ\_circ} - \text{Power\_gc}$$

$$\text{Energy\_sum} = \begin{bmatrix} 2 i_{\text{circ}_d} v_{\text{circ}_z} + 2 i_{\text{circ}_z} v_{\text{circ}_d} + \frac{i c q v_{gq}}{2} - \frac{i c d v_{gd}}{2} \\ 2 i_{\text{circ}_q} v_{\text{circ}_z} + 2 i_{\text{circ}_z} v_{\text{circ}_q} + \frac{i c d v_{gq}}{2} + \frac{i c q v_{gd}}{2} \\ 2 i_{\text{circ}_z} v_{\text{circ}_z} - \frac{i c q v_{gq}}{2} - \frac{i c d v_{gd}}{2} \end{bmatrix} \quad (8)$$

---

## C.2 Coupling matrix

$$\begin{aligned}
Tran &:= \frac{2}{3} \begin{bmatrix} \cos(\omega t) & \cos\left(\omega t - \frac{2\pi}{3}\right) & \cos\left(\omega t + \frac{2\pi}{3}\right) \\ -\sin(\omega t) & -\sin\left(\omega t - \frac{2\pi}{3}\right) & -\sin\left(\omega t + \frac{2\pi}{3}\right) \\ \frac{1}{2} & \frac{1}{2} & \frac{1}{2} \end{bmatrix} \\
Tran &:= \begin{bmatrix} \frac{2 \cos(\omega t)}{3} & -\frac{2 \cos\left(\omega t + \frac{\pi}{3}\right)}{3} & -\frac{2 \sin\left(\omega t + \frac{\pi}{6}\right)}{3} \\ -\frac{2 \sin(\omega t)}{3} & \frac{2 \sin\left(\omega t + \frac{\pi}{3}\right)}{3} & -\frac{2 \cos\left(\omega t + \frac{\pi}{6}\right)}{3} \\ \frac{1}{3} & \frac{1}{3} & \frac{1}{3} \end{bmatrix} \tag{1}
\end{aligned}$$

$$\begin{aligned}
Trans\_inv &:= combine(MatrixInverse(Tran)); \\
Trans\_inv &:= MatrixInverse(Tran) \tag{2}
\end{aligned}$$

Loading [LinearAlgebra](#)

$$\begin{aligned}
der\_Trans\_inv &:= map(diff, Trans\_inv, t); \\
der\_Trans\_inv &:= 0 \tag{3}
\end{aligned}$$

$$J := combine(Tran \cdot der\_Trans\_inv)$$

$$J := \begin{bmatrix} 0 & -\omega & 0 \\ \omega & 0 & 0 \\ 0 & 0 & 0 \end{bmatrix} \tag{4}$$

